Thesis for Doctor’s Degree

Design of Nonlinear PID Controllers and Their Application to a Heat Exchanger System for LNG-fuelled Marine Engines

Advisor: Prof. Jin, Gang-Gyoo
Prof. Shin, Seung-Ho

August 2018

The Graduate School of Ocean Science and Technology
Korea Maritime and Ocean University

Department of Convergence Study on the Ocean Science and Technology

Gun-Baek So

Approved by the Committee of the Ocean Science and Technology School of Korea Maritime and Ocean University in Fulfillment of the Partial Requirements for the Degree of Doctor of Engineering

Dissertation Committee:
Prof. Kim, Jong-Hwa, Chair

Prof. Oh, Sea-June

Prof. Choi, Hyeung-Sik

Prof. Choi, Jin-Kyu

Prof. Jin, Gang-Gyoo, Advisor

June 2018

The Graduate School of Ocean Science and Technology
Korea Maritime and Ocean University

Contents

List of Figures

List of Tables

Design of Nonlinear PID Controllers and Their Application to a Heat Exchanger System for LNG-fuelled Marine Engines

Gun-Baek So

Department of Convergence Study on the Ocean Science and Technology
Graduate School of Korea Maritime & Ocean University

Abstract

Excessive use of fossil fuels resources is adding several types of greenhouse gases which make the earth warmer. Emissions from ship's exhausts contribute to global climate change, too. The International Maritime Organization (IMO) has adopted regulations to reduce the emission of air pollutants from international shipping, such as major air pollutants, carbon dioxide (CO_2), nitrogen oxides (NOx), and sulphur oxides (SOx) under Annex VI of the 1997 MARPOL protocol. Likewise, as regulations on the emission of major air pollutants have become internationally strict, the development of environmentally friendly vessels and engines is required. One of the globally accepted means of reducing emission gases is the use of more eco-friendly fuel, LNG (Liquefied Natural Gas). LNG as a marine fuel reduces air pollutants as referred compared to traditional heavy fuel oil (HFO). Recently, large engine manufacturers are developing LNG-fuelled marine engines. In order to use this cryogenic LNG as a fuel, it is necessary to change it back to a gaseous state. A heat exchanger is used to regasify LNG. The heat exchange takes place between LNG and glycol on the primary loop, and heat exchange occurs between glycol and steam on the secondary loop. These series of processes are called LNG regasification.

To control the temperature of the heat exchanger, it is necessary to model the heat exchanger. However, it is not easy to obtain an accurate mathematical model because the heat exchanger has non-linearity and time-varying characteristics. In addition, a fixed-gain controller is bound to have a limitation in its function if parameters of the heat exchanger are changed. Thus, various techniques have been studied to improve the adaptability and robustness of the controller. Recently, there has been using nonlinear PID (NPID) controller for the controlled system which have highly nonlinear and time-varying characteristics during operation.

Therefore, this thesis proposes two types of the nonlinear proportional, integral, derivative (NPID) controllers to control the glycol temperature of the regasification system for LNG-fuelled marine engines. The Fully-Nonlinear PID (F-NPID) controller has a structure that the error between the set-point (or reference input) and output (or the measured output) is scaled nonlinearly, and input into the controller to derive proportional, integral, and derivative controllers. The Partial-Nonlinear PID (P-NPID) controller uses the conventional linear PD controller and only I controller uses the method of F-NPID controller. In this case, the nonlinear functions are implemented by the Fuzzy model of Takagi-Sugeno (T-S) type. In addition, the error is continuously scaled so that outstanding control performance can be maintained even when the operating environment is changed, thereby improving the swiftness and the closeness of responses.

Also, the parameters of the two proposed controllers are optimally tuned in terms of minimizing the integral of the absolute error (*IAE*) objective function based on the genetic algorithm (GA). Meanwhile, it is necessary to examine the stability of overall feedback system that can be caused by introducing nonlinear functions during controller design. For this, the stability of the overall feedback system is analyzed by applying the circle stability theorems, which is often used for stability analysis of nonlinear problems.

The proposed controllers are verified their performances which are the set-point tracking, robustness against noise and parameter changes, disturbance rejection performances by comparing with two conventional PID controllers and a conventional NPID controller.

KEY WORDS: Circle criterion, Nonlinear PID controller, Regasification system, Temperature control, T-S fuzzy model

Nomenclature

Alphabet

A	area of the diaphragm
a_1, a_2, b_1, b_2, c_1, c_2	positive constants defined by the user
b	parameter indicating the degree of non-iniform
d	input disturbance
F, F_i	flow rate of the glycol
F_1, F_2, F_3	membership function of the fuzzy sets
f	fitness function
g	number of generations
g_{max}	maximum number of generations
H	total enthalpy
J	objective function
K	steady-state gain
K_d	steady-state gain of disturbance, derivative gain
K_h	steady-state gain of heat exchanger
K_i	integral gain
K_{ip}	steady-state gain of I/P converter
K_p	proportional gain
K_s	steady-state gain of temperature sensor
K_u	ultimate gain
K_v	steady-state gain of pneumatic control valve
k_q	positive proportional constant
k_{sp}	spring constant
k_0, k_1, k_2	positive constants defined by the user
$k(e)$	nonlinear gain
L	time delay
m	mass of the glycol
N	maximum derivative gain
n	population size

P_u	ultimate period
p	pneumatic acting on the diaphragm
Q	heating energy
r	random value
T	transpose
T_d	derivative time
T_f	filter time constant
T_h	time constant of heat exchanger
T_i	integral time
T_s	time constant of temperature sensor
T_v	time constant of pneumatic control valve
t_p	peak time
t_r	rise time
t_s	settling time
U	internal energy of the fluid
u	control input
u_d	derivative action
u_i	integral action
u_p	proportional action
$\bar{u}, \bar{u}_i$	internal energy of the fluid
V, V_i	volume of the glycol
v	velocity of glycol fluid, nonlinearly scaled error
W_T	power applied to system
w	nonlinearly scaled error
x	displacement of valve stem, parameter vector
$\mathbf{x}_1$, $\mathbf{x}_2$	chromosome
$\bar{\mathbf{x}}_1, \bar{\mathbf{x}}_2$	offspring
α_1, α_2, α_3	degree of membership
ε	positive constant
λ	random value
μ	coefficient of friction of valve stem
θ	glycol outlet temperature

θ_d	glycol outlet temperature by input disturbance
ρ	density of the glycol
σ	standard deviation
ζ	damping coefficient
τ	time constant, random value
Ψ, Φ	nonlinear function
$\forall$	for all

Chapter 1. Introduction

1.1 Research background and trends

The development of the industry requires a lot of energy resources, and humans have been using a lot of fossil fuels as the energy resources. These fossil fuels are widely used not only power plants, chemical plants, steel mills, automobiles and homes in offshore, but also in marine vessels.

Exhaust gases generated from the use of fossil fuels in ships contain a large amount of carbon dioxide (CO_2), sulfur oxides (SOx) and nitrogen oxides (NOx) etc. CO_2 gas has the greatest impact on global warming. Changes in the global environment caused by global warming include sea level rise, desertification, abnormal climate changes, and ecosystem devastation. SOx is produced by combustion of sulfur contained in impurities in fossil fuels, and NOx is generated by the reaction of nitrogen and oxygen when the fuel burns at a very high temperature in the engine. SOx and NOx may cause acid rain, and this acid rain devastates the soil by acidifying the soil and interferes with the growth of plants or causes plants to die by destroying chlorophyll, leaf tissue and root hair cells of plants. There have been internationally active discussions on the regulation to mitigate global warming and air pollution caused by such exhaust gas emission [1-3].

The International Maritime Organization (IMO) has regulated engine exhaust gases such as carbon dioxide (CO_2), nitrogen oxides (NOx) and sulfur oxides (SOx), which are major air pollution sources, in accordance with Annex VI of the 1997 MARPOL Protocol, and the Baltic Sea area, the North Sea area, the North American Area and the United Caribbean area already brought into force as Emission Control Area (ECA) [4] (See Fig. 1.1).

Figure 1.1 Emission control area (source: Google)

According to the IMO regulation [5] related to CO_2, Attained Energy Efficiency Design Index (Attained EEDI) should be calculated for each new ship and each new ship which has undergone a major conversion. The value of this Attained EEDI should be less than or equal to the Required EEDI value. EEDI refers to the mass of CO_2 emitted when a ton of cargo is transported by one mile on the sea, and the lower the EEDI of the vessel, the better the energy efficiency.

$$\text{Required EEDI}=\frac{\text{Engine Power(kW)}\times\text{SFC}\left(\frac{\text{g}}{\text{kWh}}\right)\times\text{reduction factor } C_F}{\text{Capacity(DWT)}\times\text{Distance(mile)}}$$

If the ship construction contract is on or after January 1, 2025, or the date of delivery is on or after January 1, 2029, the EEDI reduction factor should be reduced to 0~30 [%] below the reference value according to the vessel type and dead weight tonnage.

According to IMO regulation [6] related to SOx, the sulphur content of any fuel oil used on board ships shall not exceed 3.5 [%m/m] from 2012 to January 1, 2020, and the sulphur content shall not exceed 0.5 [%m/m] on and after 1 January 2020. In particular, while ships are sailing inside the SOx emission control area (the Baltic Sea area, the North Sea area, the North American Area, the United Caribbean area), the sulphur content of fuel oil used on board ships shall not exceed 0.1 [%m/m] on and after 1 January 2015.

The IMO regulations [7] related to NOx include Tier 1, Tier 2 and Tier 3. Tier 1 regulates the NOx emission of a marine diesel engine exceeding 130 [kW] which is installed on a ship constructed on or after 1 January 2000 and prior to 1 January 2011, and NOx emission shall not exceed 9.8~17 [g/kWh] according to the engine speed rate. Tier 2 regulates the NOx emission of a marine diesel engine exceeding 130 [kW] which is installed on a ship constructed on or after 1 January 2011, and NOx emission shall not exceed 7.7~14.4 [g/kWh] according to the engine speed rate. Tier 3 regulates the NOx emission inside the NOx Emission Control Area (the North American Area, the United Caribbean area), and NOx emission shall not exceed 2.0~3.4 [g/kWh] according to the engine speed rate. This is a tremendously strengthened measure, about 20 [%] of Tier 1. Figure 1.2 shows the regulations for CO_2 emissions, NOx emissions, PM (particulate matter) emissions, and sulphur content in fuel oil.

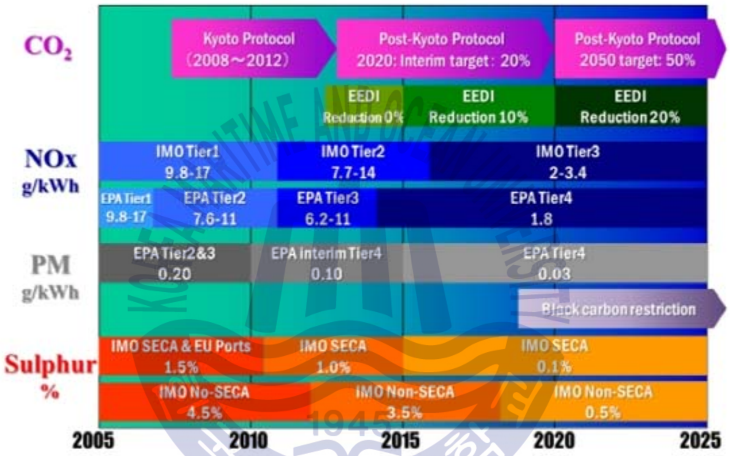

Figure 1.2 Regulation of emissions (source: Google)

As regulations of ship exhaust gas are strengthened as shown above, one of the globally accepted means of reducing emission gases is the use of more eco-friendly fuel, LNG (Liquefied Natural Gas). The use of LNG as fuel for ships can significantly reduce various air pollutants such as CO_2, SOx and NOx, and prevent marine pollution accidents due to oil spills [8].

And major countries in the world are making great efforts to lead IMO's international standards development in relation to LNG-fuelled vessels. Following the announcement of 'Maritime Transportation Strategy 2009~2018' in 2009, Europe is significantly strengthening ship fuel emission regulations and is actively encouraging the use of LNG such as changing guidelines related to sulphur content in ship fuel in 2012. Norway is strongly promoting the introduction of LNG fuel vessels with gas engine or DF (duel fuel) engine as NOx reduction measures, and especially has a plan to introduce LNG fuel propulsion vessels to public ferry managed by the country. The Dutch government is devoting itself to building infrastructure to promote the use of LNG in vessels using the port of Rotterdam, Europe's largest port. Since the establishment of a LNG terminal is not possible systematically, the United States is actively reviewing and proceeding with the construction of a LNG maritime terminal. At the government level, Japan is promoting the early adoption of natural gas-fuelled ships equipped with LNG storage facilities and is making a lot of effort to lead international standards development such as safety technology for practical application.

In order to secure the ship-sailing safety in accordance with the construction trend of LNG fuelled ships, Korea adopted the ‘Guidelines for Gas-fuelled Vessels’ set by IMO and enacted the ‘Standards for Gas-fuelled Vessels’ in January 2013. To strengthen environmental regulations and respond to high oil prices, it recently launched the 'LNG Bunkering Council' composed of the Korea Gas Corporation, shipyards, and shipping companies, and is working on the development and standardization of LNG-fuelled ships and LNG bunkering technology and improvement of the system [9].

Large engine manufacturers such as MAN Diesel & Turbo and Winterthur Gas & Diesel are developing LNG-fuelled marine engines [10-11]. The core technology in the development of LNG injection engines is the design of DF engines and tanks that can store LNG at −163°C. In order to use cryogenic LNG as a fuel, it is necessary to change it back to a gaseous state. These series of processes are called LNG regasification. A heat exchanger is used to regasify LNG. To control the temperature of a heat exchanger, it is necessary to model the heat exchanger. However, it is not easy to obtain an accurate mathematical model because the heat exchanger has non-linearity and time-varying characteristics. In addition, the parameter may change during operation, so a fixed-gain controller is effective in the limited operating range, but deviating from it can lead to poor performance and to instability, in some cases [12]. In the case of a large heat exchanger, it takes a lot of time to transfer heat, which makes it difficult to control the temperature that can ensure stable performance, so many studies have been conducted to improve this matter.

Many studies have been made on the temperature control of a cell-tube type heat exchanger as follows. Vinaya et al. [13], Oravec et al. [14], Vasičkaninová et al. [15] proposed a discrete model predictive control algorithm, and Pandey et al. [16], Kumar et al. [17], Ahmad et al. [18], Duka et al. [19], Emhemed et al. [20], Sivakumar et al. [21], Beirami et al. [22] proposed a method of combining PID control techniques based on fuzzy control, and Ahn et al. [23] proposed a PID controller that combines anti-windup and feed-forward control techniques, and Habobi et al. [24] proposed a PID controller based on PC-based controller. Sarabeevi et al. [25], Padhee et al. [26-28], Khare et al. [29], Khanvilkar et al. [30] addressed the issue of using a PID controller based on an internal model, and Xiao et al. [31], Skorospeshkin et al. [32], Manikandan et al. [33] proposed a controller based on adaptive control.

Optimal tuning of the controller parameters is very important to achieve the desired performance because the PID control determines the output of the controller through three combined actions of proportional, integral, and derivative, which are important factors determining the performance for the error between the set-point and output. The conventional PID controller has a disadvantage that it is required to re-tune the controller when the parameter of the controlled system changes due to the change of the operation condition even if these parameters are correctly tuned already. Therefore, when controlling a controlled system with nonlinearity and time-variability, the conventional PID controller is bound to have a limitation in its function. Therefore, various techniques of combining AI (artificial intelligence) techniques such as adaptive technique, gain scheduling, fuzzy, neural network, and evolutionary algorithm have been studied to improve the adaptability and robustness of the controller [34-40], and one of them is Nonlinear PID (NPID) control technique.

Recently, some forms of nonlinear PID controllers have been introduced for industrial processes [41-47]. They can be categorized into two types. One is the NPID controller introduced by Korkmaz et al. [41] and Isayed et al. [42], Zhang et al. [43], Chen et al. [44] whose gains are continuously changed based on error and/or error rate. The other is the NPID controller introduced by Seraji [45] and Zaidner et al. [46], Jiang et al. [47] where a nonlinear gain in cascade with a linear PID controller produces the scaled error.

These methods presented rather satisfactory results in different control environments, but further improvements are needed.

1.2 Research content and composition

This thesis focuses on the controller design to control the outlet temperature of the glycol on the secondary loop of the LNG regasification system in an engine using LNG as fuel.

Two types of controllers are proposed: Fully-nonlinear PID (F-NPID) controller and Partial-nonlinear PID (P-NPID) controller. The F-NPID controller has a structure that an error between the set-point and output is scaled nonlinearly, and inputs into the proportional, integral, and derivative controllers. The P-NPID controller uses the conventional linear PD controller as it is, and only the integral controller uses the method of F-NPID controller. In this case, the nonlinear function is implemented as a Fuzzy model of Takagi-Sugeno (T-S) type [70]. In addition, the error is continuously scaled so that excellent control performance can be maintained even when the operating environment is changed, improving the swiftness and the closeness of responses. Meanwhile, the stability problem of the feedback system, which may be caused by the introduction of nonlinear functions, is analyzed using a circle criterion.

Since the proposed controllers operate in two modes, the parameters are tuned by genetic algorithm (GA) and switched according to the operation mode in terms of minimizing the *IAE* (integral of the absolute error) performance index. The validity of the two proposed NPID controllers should be verified by comparing their set point tracking performance, robustness against noise and parameter changes and disturbance rejection performance with those of other three controllers.

This thesis consists of 8 chapters in total, and the contents of each chapter are as follows. Chapter 2 briefly describes the changes of the DF engine, contents about fuel injection and fuel supply systems. In Chapter 3, LNG regasification system is briefly explained and a mathematical model of the components of the temperature control system is obtained in order to control the temperature of the secondary heat exchanger. In Chapter 4, the conventional linear PID controller and the existing nonlinear PID controller to be compared are found out in this thesis. Chapter 5 proposes two nonlinear

PID controllers using fuzzy technique and discusses how to tune optimally the parameters using a GA. In Chapter 6, the stability of the feedback system is analyzed using a circle criterion. In Chapter 7, the two proposed controllers and three PID controllers to be compared are applied to the temperature control of the secondary loop heat exchanger for the LNG-fuelled marine engine and simulated. And the results of these simulations are compared and examined the validity of the proposed controllers. Finally, Chapter 8 describes final conclusions based on the results.

Chapter 2. LNG-fuelled Marine Engines

2.1 Changes of LNG-fuelled marine engines

Liquefied Natural Gas (LNG) is cooled to −163 [℃] and liquefied. As the natural gas is liquefied, the volume is reduced to about 1/600. Thus, the ship carries LNG in a cryogenic state. LNG is stored and carried in a special cargo hold. The inside of the cargo hold is made of nickel alloy steel or stainless steel so that it can withstand a cryogenic temperature of −163 [℃], and the outside is surrounded by a heat insulating material to prevent heat inflow. However, it is difficult to shut off 100 [%] of the heat input from the outside. Therefore, about 0.15 [%] of LNG of total volume is vaporized daily inside the cargo hold. As the pressure inside the cargo hold increases due to vaporization of LNG, it is dangerous. Thus, Boil Off Gas (BOG) can be taken from the cargo hold and used as fuel for the vessel, or re-liquefaction plant is used to re-liquefy and send it back to the cargo hold, or burn it if it cannot be done.

The use of natural gas as fuel in the early LNG carrier was to remove BOG in the LNG cargo hold. For over 40 years from 1964 to the mid-2000s, the steam turbine engine, an external combustion engine, had been used as the main propulsion engine for LNG carriers because it could easily solve the BOG matter. However, it was a kind of contradiction to have a low efficient external combustion engine.

Meanwhile, the Winterthur Gas & Diesel company has developed a four-stroke cycle DF engine that can use both natural gas and diesel oil as fuel. This DF engine is mainly used for power generation. It is called Dual Fuel Diesel Electric (DFDE) engine because it is a propulsion system that drives a motor connected to the propeller with electricity generated from DF engine. This DFDE engine is an eco-friendly system that has higher thermal efficiency (about 41~43 [%]) than steam turbine engines using high temperature and high pressure steam, excellent safety, and significantly reduced sulphur oxides, nitrogen oxides and carbon oxides. Courtesy of these advantages, the DFDE engine has been used as a new propulsion engine for LNG ships in place of the steam turbine engine since the mid-2000s.

Recently, the use of DF engines has been continuously reviewed at other merchant vessels other than LNG vessels due to strengthened international regulations on exhaust gases to mitigate global warming and reduce emissions of nitrogen oxides and sulfur oxides. Unlike LNG vessels, most merchant vessels today are equipped with diesel engines that use Bunker C oil as their main fuel and drive propellers directly with diesel engines. A system that directly drives a propeller with a diesel engine has better propulsion efficiency than the DFDE system. Therefore, it is better to mount a diesel engine if the BOG matter can be solved even for LNG vessels. The propulsion engine of most large merchant vessels currently in operation are using large 2 stroke cycle diesel engines with high propulsion efficiency and great power. Therefore, in order to use LNG as a fuel in a large merchant vessel, a large 2 stroke cycle DF engine that can burn gas and has high engine efficiency is needed. An engine that meets these conditions was developed in the early 1990s, but the engine is characterized by the need to receive gaseous fuel at a high pressure of up to 300 [bar] (300 times the atmospheric pressure). For this, a device for compressing and supplying the gaseous fuel to a high pressure by using a gas compressor was considered in the initial stage of development. However, this device not only used a very large power and but also had a very large volume. Thus, it was assessed no to be suitable for vessels. To overcome these disadvantages, a device was developed to supply LNG to the engine by first pressurizing LNG at a high pressure of 250~320 [bar] using a high pressure pump instead of a gas compressor, and re-gasify it. This device is 5~10 [%] level and smaller than the gas compressor when the power required for gas fuel supply is used. With the development of such a gas fuel supply system, the large DF engine began to be valued as a marine engine, and LNG-fulled marine engines can be realized in general large merchant ships. In addition, a technology was developed, which can effectively process BOG which is necessarily generated in the LNG storage tank without a separate liquefaction device by re-condensing it using LNG. However, due to the high pressure of the system, double piping is installed in a wide range in preparation for the leakage of gas and the cost is increased due to the expensive equipment.

Recently, a new two-stroke cycle engine, that directly drives the propeller while using natural gas as fuel, was developed. Typical examples are the main engine Electronic control Gas Injection (ME-GI) from MAN Diesel & Turbo and the eXtra-long stroke dual fuel (X-DF) engine from Winterthur Gas & Diesel. These two engines are DF engine (Dual fueled) which can use both Bunker C oil and natural gas as fuel. It is reported that the fuel efficiency is about 10 [%] better than DFDE system because it drives the propeller directly like the conventional diesel engine [44-49].

2.2 Fuel injection of LNG-fuelled marine engines

The DF engine is divided into two modes, that is, a high-pressure gas injection mode and a low-pressure gas injection mode depending on the gas injection pressure. Figure 2.1 shows the combustion process of a two stroke cycle DF engine by high pressure gas injection. ME-GI engine adopts this mode.

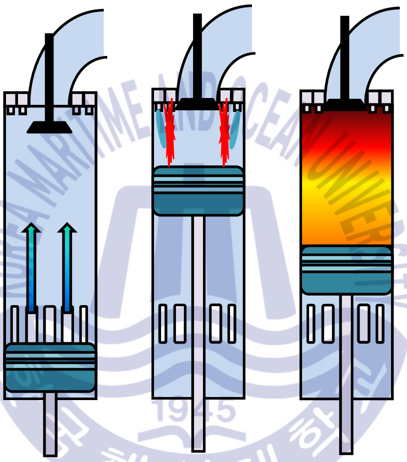

Figure 2.1 High pressure gas injection with Diesel cycle combustion process

The DF engine applying this mode operates on the principle of Diesel cycle that first compresses air with a piston and injects the fuel into the hot compressed air at the end of the compression stroke. In a gas mode using a minimum amount of liquid fuel oil, a small amount (5 [%]) of pilot fuel, which is liquid fuel oil, is compressed and ignited in the same way as a diesel engine by directly injecting it into the cylinder and gas is burned by injecting gas at a high pressure immediately after pilot fuel injection. Since liquid fuel and gas are injected into the combustion chamber at the end of compression stroke, a high injection pressure of about 300~350 [bar] is required and is frequently used in large two-stroke cycles.

As safety devices for high-pressure injection and gaseous fuel, redundancy of each system including a double piping device and a ventilation device, and various monitoring devices are installed. Figure 2.2 shows the combustion process of the 2 stroke cycle DF engine by the low-pressure gas injection mode. The X-DF engine adopts this mode.

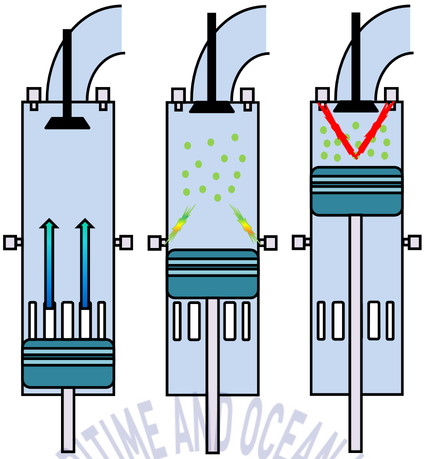

Figure 2.2 Low pressure gas injection with lean-burn Otto cycle combustion process

The cylinder structure of the DF engine adopting this mode is unusual. A scavenging port is installed in the lower part of the cylinder, and a gas injection device is installed in the middle part of the cylinder. When the piston is in the lower part of the scavenging port, the scavenging port is opened for scavenging, the piston is further raised, and the air is compressed when passing through the scavenging port. Before the piston passes the position of the gas injection valve, gas injection is performed and the mixture gas of air and fuel is compressed. The pilot fuel is injected into this compressed mixed gas to ignite and operate. Therefore, when the piston is in the middle of the cylinder, gas injection is performed, making low-pressure injection possible. As the low pressure X-DF engine has a pre-mixed homogeneous high air to fuel ratio in the combustion chamber, the flame temperature are relatively low. This results in low levels of NOx production. Conversely, with high- pressure gas injection, the temperature levels in the diffusion flame are much higher.

And the 4 stroke cycle DF engine by the low pressure gas injection mode is operated by the principle of Otto cycle or combined Otto and Diesel cycle which is the basic cycle of a gasoline engine. The most significant feature of this approach is the application of the lean-burn concept. Lean-burn refers to a method that much more air than the amount required for complete combustion is pre-mixed with the gaseous fuel outside the cylinder, inhaled into the cylinder, the mixture is compressed, and the pilot fuel is injected to ignite and operate. Since the air and the fuel are mixed in advance outside the cylinder, the mixed gas is uniformly distributed in the cylinder, the maximum combustion temperature is lowered, resulting in decreasing the NOx.

And the gas pressure is about 4~5 [bar] because air and gas are mixed before passing through the intake valve and the mixed gas is injected during the intake period. In particular, the micro-pilot of low-pressure gas injection injects and ignites about 1 [%] of the liquid fuel oil in the pre-combustion chamber by injection valve and is ignited by the lean mixed gas inside the main combustion chamber. Table 2.1 shows the differences in the theoretical cycle, pressure and characteristics required for mixed use with other fuels in ships using LNG as fuel.

Table 2.1 Comparison of LNG-fuelled marine engines

	Single fuel (LNG)	Dual fuel capacity (LNG or MDO)	Multi-fuel capacity (LNG, MDO or HFO)
Theoretical cycle	Otto cycle	Combined Otto /Diesel cycle	Diesel cycle
Fuel supply pressure	Low gas-pressure, 4~5 [bar]	Low gas-pressure, 4~5 [bar]	High-pressure gas-injection, 300~350 [bar]
Characteristics	High energy efficiency and lower emission than a diesel engine	Flexible and has back-up fuel	Need NOx-reduction techniques to meet IMO Tier III
Methane emission	Emits methane, but that is limited by design and combustion process control	Emits methane, and that is hard to meet by combustion process control	No methane emissions, and 30 [%] GHG reduction compared to HFO
Gas quality	Sensitive to gas quality	Sensitive to gas quality	Not sensitive to gas quality
Installation	Not suitable for retrofitting of existing engines	Possible to retrofit in existing engines	Suitable for conversion of existing engines, simple process

2.3 Fuel supply system of LNG-fuelled marine engines

Unlike the DFDE engine, the ME-GI engine requires a high-pressure fuel supply system up to 300 [bar]. It also drives the propeller directly with the ME-GI engine like the propulsion of a conventional diesel engine. Therefore, it can be applied without significant changing the conventional structure of engine-room, and the efficiency is high and maintenance/repair is easy. These ME-GI engines are more effective than DFDE engines in medium and large-sized vessels with large propulsion power.

The types of fuel supply system of the ME-GI engine developed so far are as follows.

(1) Gas compression type fuel gas supply system (HiCOM FGSS)

This is a system of pressurizing gaseous natural gas to 300 [bar] using a high pressure multi-stage reciprocating compressor and was developed to use BOG generated by the evaporation of LNG from the cargo hold of LNG vessels as direct fuel. Despite its advantage that the system is relatively simple, there are disadvantages that the compressor is large and the power consumption is large due to compression of gas.

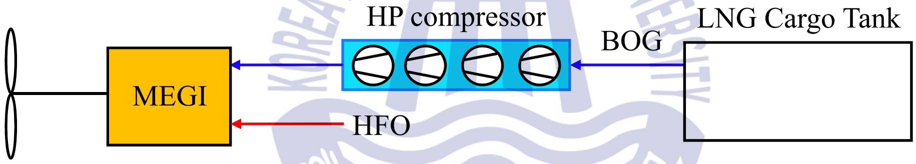

Figure 2.3 HiCOM FGSS [49]

(2) High-pressure pump type fuel gas supply system (HiVAR FGSS)

The HiVAR FGSS in Figure 2.4 is a system to compensate for the disadvantages of HiCOM FGSS. This consists of HP pump and HP vaporizer, and vaporizes LNG through the HP vaporizer at room-temperature in a gaseous state after pressurizing it to 300 [bar] by using HP pump. Since the LNG with a small volume is pressurized, the power consumption of the pump is small and the system can be compactly constructed, which makes it easy to be mounted on the vessels. Compared with HiCOM FGSS, which compresses gas using compressor, it is easy to apply to other merchant vessels. Figure 2.5 and Figure 2.6 are the photos of actually developed HiVAR FGSS.

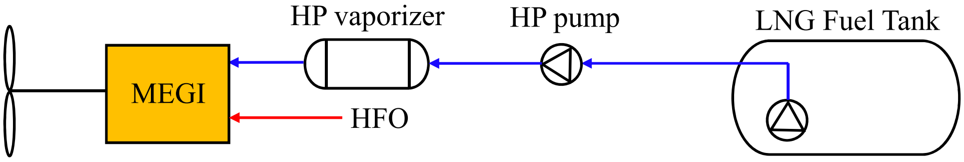

Figure 2.4 HiVAR FGSS [49]

Figure 2.5 HP pump and HP vaporizer [49]

Figure 2.6 HiVAR FGSS test skid [49]

(3) Hybrid fuel gas supply system (Hybrid FGSS)

The combination of HiCOM FGSS and HiVAR FGSS is called Hybrid FGSS, which is mainly used for LNG vessels. HiCOM FGSS is used because the amount of BOG generated from LNG cargo holds is large during the sailing with loading LNG. LNG and HiVAR FGSS stored for use as fuel are used because the amount of BOG generated after LNG is unloaded is small.

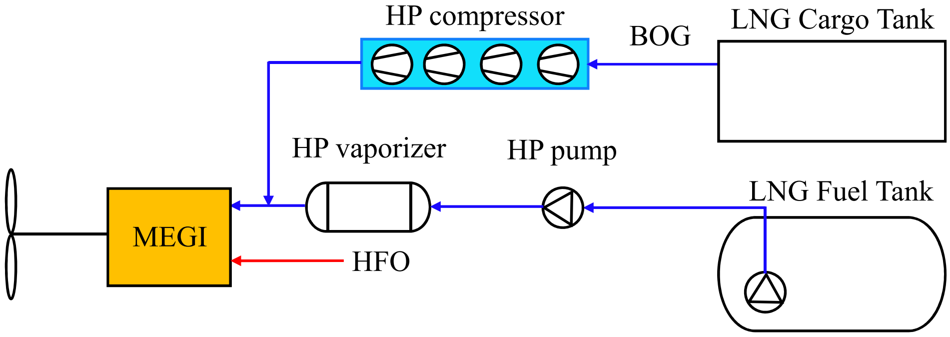

Figure 2.7 Hybrid FGSS [49]

(4) Example of FGSS

Figure 2.8 shows an example of an entire FGSS, consisting of low-pressure pump, high-pressure pump, gas valve unit (GVU), LP vaporizer, and an HP vaporizer.

The upper part of the Figure 2.8 shows the low pressure supply system, which is composed only of low pressure pump, LP vaporizer and GVU without the high pressure pump because natural gas of 4~5 [bar] and 20~30 [℃] is supplied into the cylinder. In the case of the low-pressure system, there is no need to additionally install a high-pressure pump, so the system can be constructed relatively easily. Particularly when the storage tank is Type C, the pressure build-up unit (PBU) is installed without a low pressure pump, so the internal pressure of the storage tank is maintained higher than the pressure supplied to the engine, making it possible to supply natural gas of about 5 [bar] to the engine. This system is mainly used for FGSS of DF engine for power generation.

The lower part of Figure 2.8 shows the high pressure supply system. When the LNG is transferred from the tank where the LNG is stored using the low pressure pump to the high pressure pump inlet, the high pressure pump boosts the pressure to 200~350 [bar]. This boosted LNG is re-gasified in a high-pressure vaporizer and injected into a combustion chamber in a cylinder through a gas fuel injection valve.

This system is mainly used for gas fuel supply of the ME-GI engine among DF engines for the main propulsion.

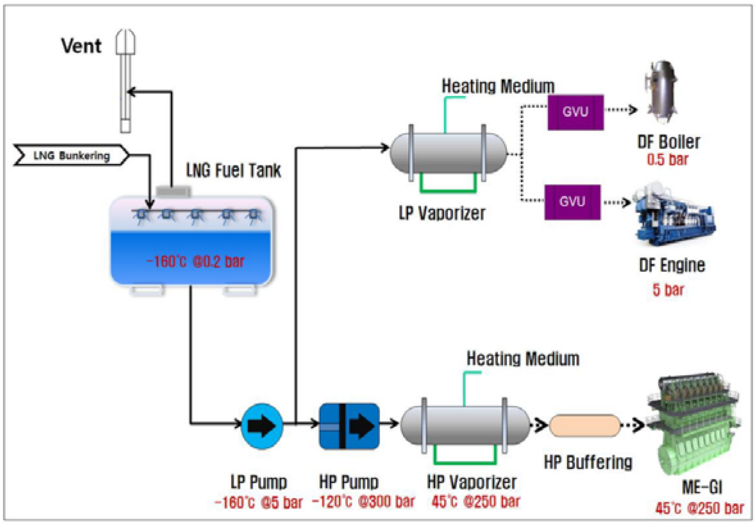

Figure 2.8 A LNG schematic diagram of FGSS for LNG-fuelled marine engines [10]

Figure 2.9 is an example of a high-pressure supply system consisting of a cryogenic HP pump and a vaporizer.

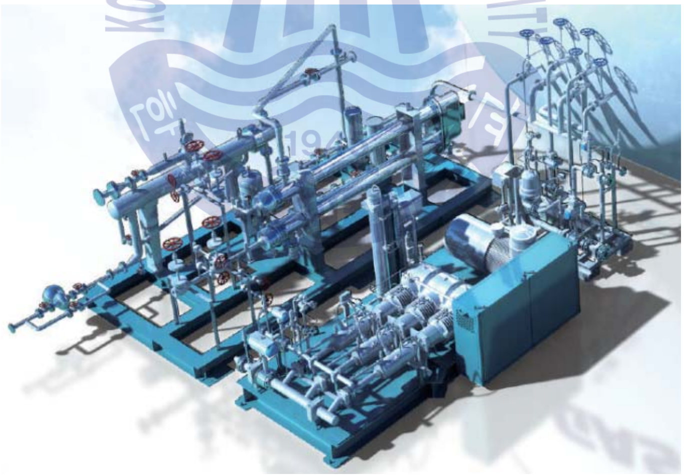

Figure 2.9 Cryogenic HP pump and HP vaporizer (source: Hyundai Heavy Industries)

Chapter 3. Modeling of LNG Regasification System

3.1 Heat exchanger

In order to supply LNG, which is natural gas liquefied at a temperature of −163 [℃], to the engine as fuel, a regasification system is required to raise it to an appropriate temperature and convert it into gas. The core equipment in this regasification system is a heat exchanger. The heat exchanger is an equipment that exchanges heat between low temperature and high temperature fluids flowing through a heat transfer wall and is widely used throughout industrial processes such as power plants, petrochemical plants, and vessels. Generally, cell-tube type, plate type, and pin-tube type are used in the industrial field, while the most widely used type is the cell-tube type of Figure 3.1. This heat exchanger has heat exchange between shell and tube side flow.

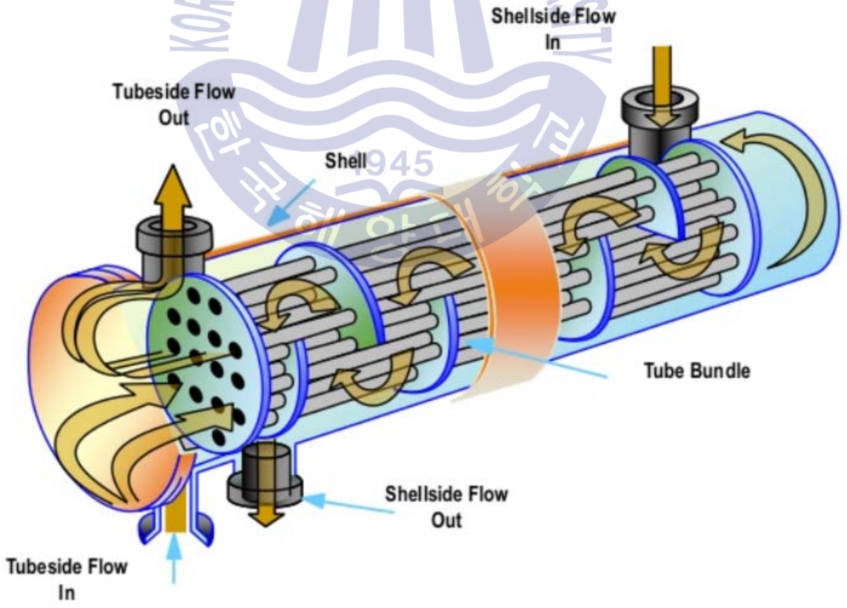

Figure 3.1 Shell and tube heat exchanger

In a shell and tube heat exchanger, a plurality of tubes is contained in a cylindrical shell, and the ends of the tubes are fixed to a tube plate so that the fluid flowing in the tubes is distributed in the header. The fluid flowing inside the shell flows through the baffle plate so as to flow as perpendicularly as possible to the tube. The advantage of this heat exchanger is that it can be cleaned both inside and outside of the heat pipe, so it is also suitable for fluid which is prone to contamination and has a wide range of applications. Since the heat transfer tube and the body can be thermally expanded, it can be used even when the temperature difference is large. This heat exchanger is suitable for a high-pressure fluid, and when the high-pressure fluid is flowed into the pipe, the pressure-resistant portion is small, so that the weight can be reduced. The manufacture is relatively simple because the structure is simple and the flange on the side of the tube plate or the body is small. Types of shell and tube heat exchangers include floating head type, fixed tube sheet type, U-tube type and kettle type [50].

3.2 LNG regasification system

Figure 3.2 shows an example of an LNG regasification system used in an LNG-fuelled marine engines.

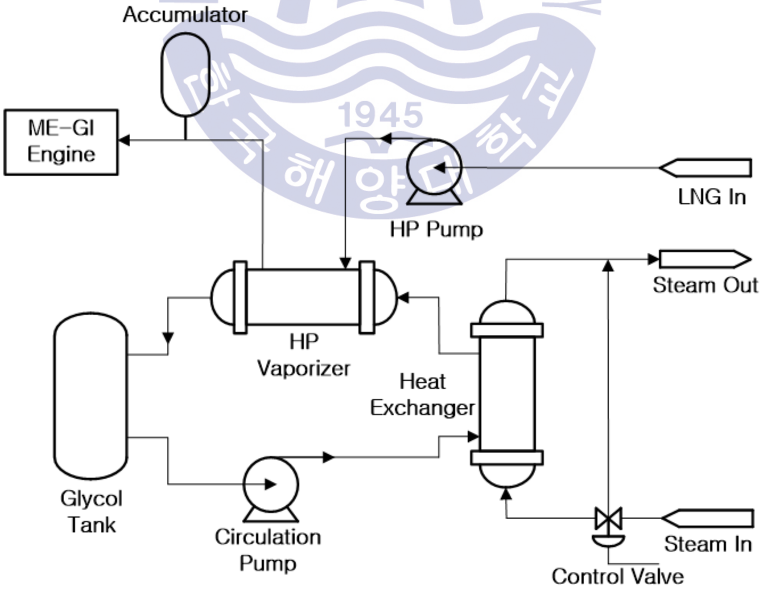

Figure 3.2 A LNG regasification system for LNG-fuelled marine engines

This LNG regasification system consists of primary and secondary loops. The −163 [℃] LNG on the primary loop is boosted to about 250~300 [bar] by the HP pump, converted to a gas state of 35~45 [℃] while passing through the high pressure evaporator, and fed into the engine cylinder through the injector. At this time, the LNG is supplied with heat from the glycol (as the intermediate heating medium). Meanwhile, glycol, which is lowered in temperature due to heat exchange with LNG, is reheated through the heat exchanger in the secondary loop, and heat is supplied from the steam at this time. In summary, heat exchange takes place between LNG and glycol on the primary loop, and heat exchange occurs between glycol and steam on the secondary loop [51-52]. The purpose of this thesis is to control the amount of steam supplied to the heat exchanger on the secondary loop to keep the outlet temperature of glycol (ie, the inlet temperature of the HP evaporator) constant. For this, the steam flow rate supplied to the heat exchanger is controlled by a pneumatic valve which receives a signal from the controller. The current signals of 4~20 [mA] output from the controller is converted to an air pressure signal in the range of 0.2~2 [bar] (3~115 [psi], 20~200 [kPa]) through an I/P (current to pressure) converter. This pneumatic signal is input to the diaphragm valve to cause displacement of the valve stem, thereby regulating the amount of steam.

3.3 Modeling of the secondary loop heat exchanger of LNG regasification system

In this section, a mathematical model of the components of the secondary loop heat exchanger system is derived to control the outlet temperature of the glycol through the heat exchanger.

3.3.1 Model of an I/P converter

An I/P (current to pressure) converter is a device that converts analog electrical signals into pneumatic signals (See Figure 3.3). This controls the valve opening and is ultimately used to control the flow rate by converting the electrical signals from the controller into pneumatic signals and supplying them to pneumatic actuators.

Figure 3.3 An I/P converter (source: Google)

It is regarded as having a proportional relationship between the input u and output p in the use of the signal range, and is expressed as the following equation [25].

$$G_{ip}(s)=\frac{P(s)}{U(s)}=K_{ip} \tag{3.1}$$

When an industrial I/P converter converts an analog signal of 4~20 [mA] to pneumatic of 3~15 [psi], and the input current applied to the I/P converter is u and the output pneumatic is p, the gain is obtained as follows.

$$K_{ip}=\frac{15-3}{20-4}=0.75\ [\mathrm{psi/mA}]$$

3.3.2 Model of a pneumatic control valve

A pneumatic control valve, also known as a diaphragm valve, receives pneumatic signals from the I/P converter and regulates the steam flow rate into the pipe, ultimately controlling the quantity of heat supplied to the heat exchanger. Figure 3.4 shows a typical pneumatic control valve consisting of a diaphragm valve, spring, valve stem, and valve.

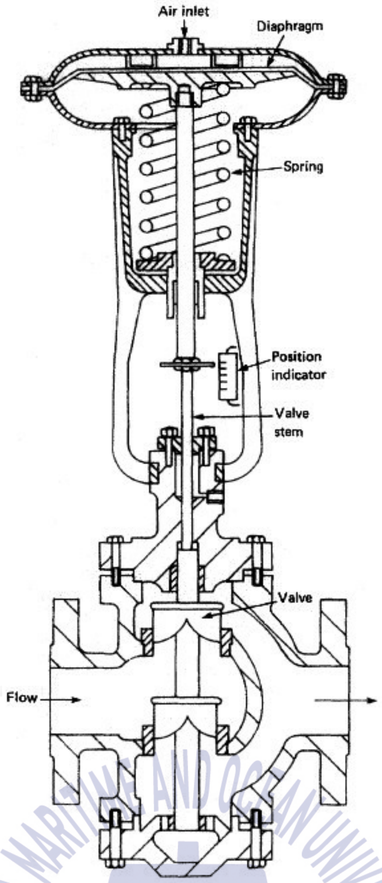

Figure 3.4 A pneumatic control valve (source: Google)

The equation equilibrium of the force applied to the diaphragm valve is as follows.

$$p(t)A = k_{sp}x(t) + \mu\frac{dx(t)}{dt} \tag{3.2}$$

where A is the area of the diaphragm, p is the pneumatic acting on the diaphragm, k_{sp} is the spring constant, μ is the coefficient of friction of the valve stem, and x is the displacement of the valve stem [25].

Meanwhile, assuming that the quantity of heat supplied to the heat exchanger is proportional to the displacement of the valve stem, the following equation can be obtained.

$$q(t) = k_q x(t) \tag{3.3}$$

where k_q is a positive proportional constant. Equation (3.4) is obtained when Equation (3.2) is substituted for Equation (3.3).

$$k_q A p(t) = k_{sp} q(t) + \mu \frac{dq(t)}{dt} \tag{3.4}$$

When this is transformed by Laplace, the following equation is obtained.

$$k_q A P(s) = (\mu s + k_{sp}) Q(s) \tag{3.5}$$

The transfer function $G_v(s)$ of the pneumatic control valve is obtained with the input as pneumatic and the output as steam heat.

$$G_v(s) = \frac{Q(s)}{P(s)} = \frac{k_q A}{\mu s + k_{sp}} = \frac{\frac{k_q}{k_{sp}} A}{1 + \frac{\mu}{k_{sp}} s} = \frac{K_v}{1 + T_v s} \tag{3.6a}$$

$$K_v = \frac{k_q}{k_{sp}}, \quad T_v = \frac{\mu}{k_{sp}} \tag{3.6b}$$

where K_v and T_v are the steady-state gain and time constants of the pneumatic control valve, respectively. For example, if the pressure acting on the diaphragm valve is in the range of 3~15 [psig] and the heat quantity of steam is 1.6 [kcal/sec] at the maximum displacement of the valve stem, the valve gain can be approximated as follows.

$$K_v = \frac{\text{Change of steam amount}}{\text{Pressure range}} = \frac{1.6 - 0}{15 - 3} = \frac{0.4}{3} \ [\text{kcal/sec} \cdot \text{psig}]$$

3.3.3 Model of a heat exchanger

The heat exchanger vaporizes LNG at the vaporizer and then heats the returned low temperature glycol to the steam. In the cell-tube type heat exchanger where heat exchange occurs, steam flows into the tube and glycol flows toward the cell. In general, a heat exchanger is nonlinear, and is a distributed parameter system, which is described by complex partial differential equations. However, to simplify the matter, the model is obtained by considering it as a linear, lumped parameter system. At this time, it is assumed that the temperature of the supply steam is constant, and the heat exchanger and the pipe are sufficiently insulated to have no heat loss from the outside. Since the difference between the mass flow rate at the inlet and outlet side of glycol on the heat exchanger is equal to the mass flow rate for Δt, it can be expressed as follows [25,33].

$$\Delta m = \Delta(\rho V) = \rho_i V_i - \rho V = (\rho_i F_i - \rho F)\Delta t \tag{3.7a}$$

$$\frac{\Delta m}{\Delta t} = \frac{\Delta(\rho V)}{\Delta t} = \rho_i F_i - \rho F \tag{3.7b}$$

where m is the mass of the glycol [kg], ρ_i and ρ are the density of the glycol [kg/m^3], V_i and V are the volume of the glycol [m^3], F_i and F are the flow rate of the glycol [m^3/sec], and subscript i indicates the inlet side. When Δt is very small, it can be expressed as a derivative term as follows.

$$\lim_{\Delta t \to \infty} \frac{\Delta m}{\Delta t} = \frac{dm}{dt} = \frac{d(\rho V)}{dt} = \rho_i F_i - \rho F \tag{3.8}$$

Assuming that the density of glycol on the inlet/outlet side is constant, the following equation is obtained.

$$\frac{dV}{dt} = F_i - F \tag{3.9}$$

Ignoring the kinetic energy and the potential energy, the energy equilibrium equation is as follows.

$$\frac{dU}{dt} = F_i \rho_i \bar{u}_i - F \rho \bar{u} + Q + W_T \tag{3.10}$$

where U is the internal energy of the fluid, Q is the heating energy per second, $\bar{u}_i$ and $\bar{u}$ are the internal energy of the fluid per unit mass, and W_T is the power applied to the system.

Since the power [watt] applied to the system is equal to the sum of the energies performed around it to force the fluid to flow, it can be expressed as follows.

$$W_T = F_i p_i - Fp \tag{3.11}$$

Equation (3.12) is obtained when Equation (3.10) is substituted for Equation (3.11).

$$\begin{aligned} \frac{dU}{dt} &= F_i \rho_i \bar{u}_i - F \rho \bar{u} + Q + F_i p_i - Fp \\ &= F_i \rho_i (\bar{u}_i + \frac{p_i}{\rho_i}) - F \rho (\bar{u} + \frac{p}{\rho}) + Q \end{aligned} \tag{3.12}$$

The enthalpy per unit mass $\bar{h}$ is equal to the sum of the internal energy per unit mass $\bar{u}$ and the work energy p/ρ applied externally per unit mass.

$$\bar{h} = \bar{u} + \frac{p}{\rho} \tag{3.13}$$

Equation (3.13) can be substituted into Equation (3.12) and summarized as follows.

$$\frac{dU}{dt} = F_i \rho_i \bar{h}_i - F \rho \bar{h} + Q \tag{3.14}$$

In addition, the total enthalpy H is equal to the sum of the total internal energy U and the total work energy pV applied externally, so the following equation is obtained.

$$H = U + pV \tag{3.15}$$

Equation (3.15) can be rewritten as follows by applying the relationship of $dH/dt= dU/dt+dpV/dt$.

$$\frac{dU}{dt} = \frac{dH}{dt} - \frac{d(pV)}{dt} = F_i \rho_i \bar{h}_i - F \rho \bar{h} + Q \tag{3.16}$$

where the enthalpy per unit mass is as follows.

$$\bar{h}_i(T) = \int_{T_r}^{T_i} C_p dT = C_p \int_{T_r}^{T_i} dT = C_p T \Big|_{T_r}^{T_i} = C_p (T_i - T_r) \tag{3.17a}$$

$$\bar{h}(T) = \int_{T_r}^{T} C_p dT = C_p \int_{T_r}^{T} dT = C_p T \Big|_{T_r}^{T} = C_p (T - T_r) \tag{3.17b}$$

By ignoring the pressure-volume change and substituting Equation (3.17) into Equation (3.16), it can be obtained the following equation.

$$\begin{aligned} \frac{dU}{dt} = \frac{dH}{dt} &= F_i \rho_i \bar{h}_i - F \rho \bar{h} + Q \\ &= F_i \rho_i C_p (T_i - T_r) - F \rho C_p (T - T_r) + Q \end{aligned} \tag{3.18}$$

Meanwhile, the total enthalpy can be obtained by multiplying the enthalpy per unit mass by the mass.

$$H = m\bar{h} = \rho V \bar{h} \quad [J] \tag{3.19}$$

If the density ρ $(=\rho_i)$ and the specific heat at constant pressure are constant, then the derivative term of total enthalpy can be expressed as:

$$\frac{dH}{dt}=\frac{d(\rho V\bar{h})}{dt}=\frac{d(\rho VC_p(T-T_r))}{dt}=\rho VC_p\frac{d(T-T_r)}{dt}+\rho C_p(T-T_r)\frac{dV}{dt} \tag{3.20}$$

The following is obtained from Equation (3.18) and Equation (3.20).

$$\rho VC_p\frac{d(T-T_r)}{dt}+\rho C_p(T-T_r)\frac{dV}{dt}=F_i\rho_i C_p(T_i-T_r)-F\rho C_p(T-T_r)+Q \tag{3.21}$$

Equation (3.22) is obtained when Equation (3.21) is substituted for Equation (3.9).

$$\rho VC_p\frac{d(T-T_r)}{dt}=F_i\rho_i C_p(T_i-T)+Q \tag{3.22}$$

If the temperature T_r is constant, it is re-summarized as the following equation.

$$\rho VC_p\frac{dT}{dt}=F_i\rho_i C_p(T_i-T)+Q \tag{3.23}$$

$$\frac{dT}{dt}=\dot{T}(t)=\frac{F_i}{V}(T_i-T)+\frac{Q}{\rho VC_p}=\frac{F_{is}}{V_s}(T_{is}-T)+\frac{Q}{\rho V_s C_p} \tag{3.24}$$

where the subscript s indicates a steady-state.

If $q \triangleq Q-Q_s$, $\theta_h=T_h \triangleq T-T_{is}$, Equation (3.15) is obtained when Equation (3.24) is substituted for these.

$$\frac{dT_h}{dt}=\frac{dT}{dt}-\frac{dT_{is}}{dt}=\frac{dT}{dt} \tag{3.25a}$$

$$\frac{dT}{dt}=\frac{F_{is}}{V_s}(T_{is}-T)+\frac{Q}{\rho V_s C_p} \tag{3.25b}$$

$$\frac{dT_h}{dt}=\frac{F_{is}}{V_s}(-T_h)+\frac{Q}{\rho V_s C_p} \tag{3.25c}$$

$$\frac{d\theta_h}{dt}=\frac{F_{is}}{V_s}(-\theta_h)+\frac{Q}{\rho V_s C_p}=\frac{F_{is}}{V_s}(-\theta_h)+\frac{q+Q_s}{\rho V_s C_p}=\frac{F_{is}}{V_s}(-\theta_h)+\frac{q}{\rho V_s C_p} \tag{3.25d}$$

The following equation is obtained by Laplace transforming Equation (3.25d).

$$s\Theta_h(s)=-\frac{F_{is}}{V_s}\Theta_h(s)+\frac{1}{\rho V_s C_p}Q(s) \tag{3.26}$$

After rearranging this, the transfer function from q to θ_h is obtained as follows.

$$G_h(s)=\frac{\Theta_h(s)}{Q(s)}=\frac{\dfrac{1}{\rho V_s C_p}}{s+\dfrac{F_{is}}{V_s}}=\frac{\dfrac{1}{\rho C_p F_{is}}}{1+\dfrac{V_s}{F_{is}}s}=\frac{K_h}{1+T_h s} \tag{3.27}$$

where $K_h = 1/\rho C_p F_{is}$ is the heat exchanger steady-state gain, and $T_h = V_s/F_{is}$ is the time constant of the heat exchanger.

3.3.4 Model of a disturbance

In general, the main disturbance that can be considered in a cell-tube type heat exchanger is the glycol flow rate and glycol temperature changes. The change in glycol flow rate is insignificant as long as the circulation pump of the secondary loop is operated at a constant speed. Suddenly changing the engine speed according to the bridge command will eventually cause a change in the LNG injection quantity, which may cause the temperature of the glycol that returns via the HP evaporator to change. Therefore, since the temperature change of the glycol is larger than the change of the flow rate, the disturbance can be approximated by the following equation based on the heat exchanger model obtained above [25].

$$T_h\dot{\theta}_d+\theta_d=K_d d \tag{3.28}$$

where d is the input disturbance [℃], θ_d is the temperature change [℃] caused by this, and K_d is the steady-state gain of the disturbance.

This can be expressed as the transfer function as follows.

$$G_d(s) = \frac{\Theta_d(s)}{D(s)} = \frac{K_d}{1 + T_h s} \tag{3.29}$$

3.3.5 Model of a RTD sensor

The sensor and transmitter sense the output temperature θ, amplify it and convert it to the current signal y. It can be expressed as first-order linear differential equation as follows [25].

$$T_s \frac{dy(t)}{dt} + y(t) = K_s \theta(t) \tag{3.30}$$

where y is the current signal [mA] corresponding to the glycol outlet temperature, and K_s and T_s are the steady-state gain and time constant of the temperature sensor, respectively.

The transfer function $H(s)$ for the temperature sensor is obtained by taking Laplace transformation for Equation (3.30) and using the input as the temperature and the output as the current.

$$H(s) = \frac{Y(s)}{\Theta(s)} = \frac{K_s}{1 + T_s s} \tag{3.31}$$

With considering a thermocouple sensor that converts the temperature of 0~100 [℃] to the current of 4~20 [mA] for feedback of the output signal, the gain of the sensor model can be approximated as follows.

$$K_s = \frac{\text{Current range}}{\text{Temperature range}} = \frac{20-4}{100-0} = 0.16\ [\text{mA}/^{\text{o}}\text{C}]$$

3.3.6 Model of a time delay

One of the factors considered when dealing with a heat exchanger system is a time delay, also known as a time delay. In this work, time delay may be caused by the measurement rather than an inherent dynamic characteristic of the system. Generally, the sensor should be installed in the glycol outlet pipe right next to the heat exchanger (a in Figure 3.5), but if it is installed in a further position (b in Figure 3.5) due to limitations such as installation location, time delay will occur. If the measured temperature at point a is $y(t)$, and the measured temperature at point b is $y(t-L)$, the time delay is expressed as $L=\lambda/v$, where λ is the distance between two points of 'a' and 'b', and v is the velocity of glycol fluid. The result of a recent field trip of the regasification system being commissioned at Hyundai Heavy Industries and Daewoo Shipbuilding & Marine engineering shows that the sensor installation location was close to the heat exchanger and the circulation speed of the high-pressure circulation pump was very fast.

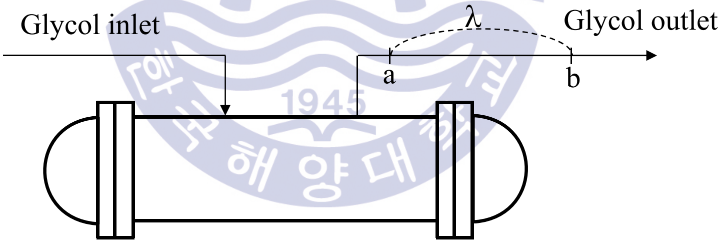

Figure 3.5 Time delay concept in heat exchanger

The transfer function of the time delay is expressed by e^{-Ls}. Since the stability analysis for the feedback system requires a rational transfer function, the first-order Padé approximation [69] is used as

$$e^{-Ls} \approx \frac{1-\frac{L}{2}s}{1+\frac{L}{2}s} \tag{3.32}$$

The term in the denominator has a negative real pole in the left-half plane and thus introduces probable dynamic effects to the characteristic polynomial of the feedback system. The transfer function linking the RTD sensor model in Equation (3.31) and the approximation in Equation (3.32) yields

$$H(s) = \frac{K_s(1-\frac{L}{2}s)}{(1+T_s s)(1+\frac{L}{2}s)} \tag{3.33}$$

3.3.7 Open-loop control system

Previously, the matter of obtaining transfer function equations of individual elements in a heat exchanger system corresponding to the controlled system of this thesis has been discussed. By combining Equation (3.1), the transfer function of the previously obtained I/P converter, Equation (3.6), the transfer function of pneumatic control valve, Equation (3.27), the heat exchanger transfer function, Equation (3.29) of the disturbance transfer function and Equation (3.33) of the sensor transfer function, the open-loop transfer function can be written as:

$$\begin{aligned} \Theta(s) &= G_{ip}(s)G_v(s)G_h(s)U(s) + G_d(s)D(s) \\ &= K_{ip}\frac{K_v}{1+T_v s}\frac{K_h}{1+T_h s}U(s) + \frac{K_d}{1+T_h s}D(s) \end{aligned} \tag{3.34}$$

$$Y(s) = H(s)\Theta(s) = \frac{K_s(1-\frac{L}{2}s)}{(1+T_s s)(1+\frac{L}{2}s)}\Theta(s) \tag{3.35}$$

The open-loop control system is shown in Figure 3.6 as a block diagram.

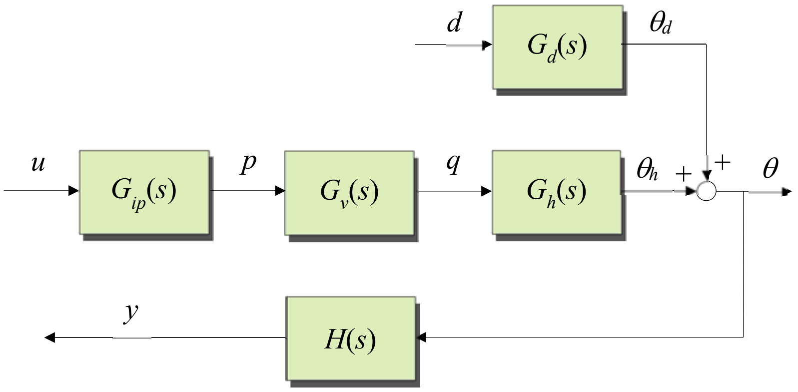

Figure 3.6 Block diagram of the plant

where u is the controller output [mA] as control input, θ is the glycol outlet temperature [°C] as output, y is the temperature measured in the sensor [mA] and d is the glycol inlet temperature [°C] as a disturbance.

Chapter 4. Surveys of Existing PID Controllers

In this chapter, a conventional linear PID controller which is the frame of a nonlinear PID controller proposed in Chapter 5 and two types of existing nonlinear PID controllers which are already proposed are examined.

4.1 Linear PID controller

The PID controller is a controller that linearly combines proportional, integral, and derivative actions and has a simple structure and high control performance.

In addition, it is still widely used enough to account for more than 90 [%] in the control loop of the industrial site because of its advantages such as easy selection of structure including P, PI, PD, PID and easy combination with additional including Anti-windup, Bumpless transfer [54].

4.1.1 Structure of the conventional PID controller

The PID controller, which is the most widely used to control several dynamic systems used in the industrial field, is the implementation of the algorithm on hardware that induces proportional, integral and derivative actions for the error between set-point or reference input and current output to generate appropriate control input u as shown in Equation (4.1).

$$u(t) = u_p(t) + u_i(t) + u_d(t) \tag{4.1a}$$

$$u_p(t) = K_p e(t) \tag{4.1b}$$

$$u_i(t) = K_i \int_0^t e(\tau) d\tau \tag{4.1c}$$

$$u_d(t) = K_d \frac{de(t)}{dt} \tag{4.1d}$$

where e is the error, K_p is the proportional gain, K_i is the integral gain, and K_d is the derivative gain. Laplace transform of Equation (4.1) can be expressed as the following equation in the frequency domain. Figure 4.1 shows this as a block diagram.

$$U(s) = U_p(s) + U_i(s) + U_d(s) \tag{4.2a}$$

$$U_p(s) = K_p E(s) \tag{4.2b}$$

$$U_i(s) = \frac{K_i}{s} E(s) \tag{4.2c}$$

$$U_d(s) = K_d s E(s) \tag{4.2d}$$

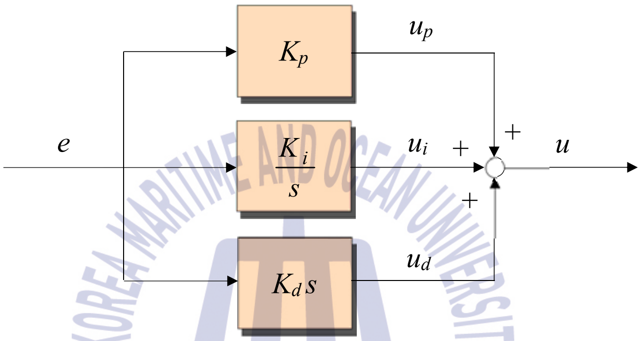

Figure 4.1 Structure of the conventional PID controller

Equation (4.2) can be simply written as the following equation:

$$U(s) = K_p\left(1 + \frac{1}{T_i s} + T_d s\right)E(s) \tag{4.3}$$

where $T_i = K_p/K_i$ and $T_d = K_d/K_p$ indicate to the integral time and the derivative time, respectively.

4.1.2 Characteristics of control actions

The output of the PID controller varies greatly according to the characteristics of the three actions and the magnitude of the gain. The characteristics of each action are explained as follows briefly.

(1) Proportional action

As shown in Equation (4.1b), proportional action produces the output by multiplying appropriate proportional gain K_p and the error between set-point and current output. When the error and proportional gain are large, the output is large. In particular, the ratio of the full range of the output to the magnitude of the corresponding error is called the proportional band (PB). That is, PB can be expressed as Equation (4.4) and is a value indicating the change in the input signal required to produce the output change of 100 [%] in %. The magnitude of this PB determines the sensitivity of the controller. Figure 4.2 shows this.

$$PB = \frac{100}{K_p} \tag{4.4a}$$

$$U_p(s) = K_p E(s) \tag{4.4b}$$

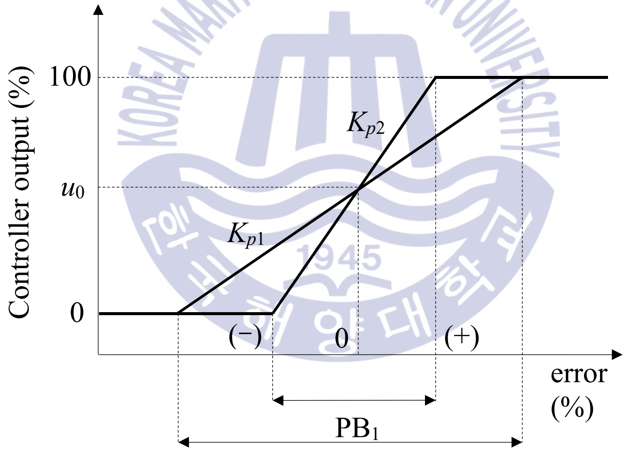

Figure 4.2 Proportional band

When only proportional action is applied to a 0-type system, a steady-state error called an offset is occurred. If the proportional gain K_p is designed to be large or PB is designed to be small enough to be sensitive to the error, the offset becomes small. However, the integral action is used together in some cases because it is not possible to make offset to eliminate completely only using the proportional action.

(2) Integral action

As described previous, proportional action generates an offset when used alone in a 0- type system. One way to eliminate this is to add the result of multiplying the integral value of the error by the gain K_i to the controller output as in Equation (4.1c). Even if a small error is continuously integrated with sufficient time, the value becomes large, making the offset zero.

Figure 4.3 shows the graph of the integral action for the error. It linearly increases for a certain error, and when it becomes zero, the integral action is fixed to the previous output state. The integral action can eliminate the steady-state error even in the system where the parameter changes, but it is disadvantageous in that the overshoot is increased due to the characteristics of the control action and the oscillation is caused until the output converges to the steady-state.

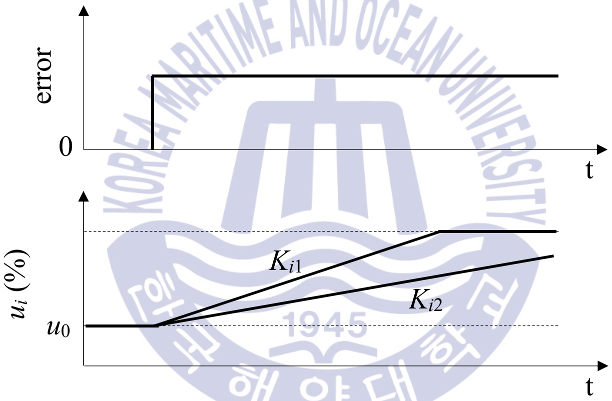

Figure 4.3 Integral action

(3) Derivative action

As shown in Equation (4.1d), the derivative action responds in proportion to the differential of the error, that is, the rate of change of the current error. Since the output of derivative action becomes zero when the error is constant, it cannot be used alone and is used with the proportional action or integral action.

As can be seen in Figure 4.4, the derivative action should be used with caution in systems with fast response characteristics because the output can change rapidly depending on the rate of change of error. If noise is included in the measured signal, the derivative action amplifies the noise greatly, so special attention should be paid to blocking noise.

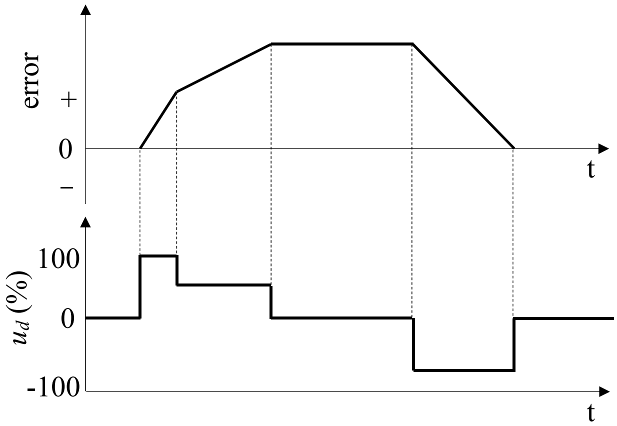

Figure 4.4 Derivative action

4.1.3 Effects of PID controller gains

As examined previous, the PID controller of Equation (4.1) consists of the parallel combination of three actions: Proportional action (u_p), integral action (u_i), and derivative action (u_d). u_p, u_i and u_d are calculated by multiplying the current error by proportional gain, the cumulative error from the beginning to the present time by integral gain and the rate of change of error by derivative gain, respectively. Finally, the control input is calculated by summing these values.

The performance of the feedback system is directly influenced by the selection of the three gains K_p, K_i, K_d. K_p increases response speed and reduces rise time but increases oscillation on the system. Although reducing steady-state error, K_i may make the transient response worse, and K_d serves to reduce overshoot and settling time.

Table 4.1 summarizes the effect of increasing or decreasing these values [55].

Table 4.1 Effects to controller parameters changes

Parameter	Overshoot (M_p)	Rise time (t_r)	Settling time (t_s)	Steady-state error (ε)
K_p	increase	decrease	-	decrease
K_i	decrease	decrease	increase	eliminate

K_d	decrease	-	decrease	-

It is necessary to know the fact that these three control actions are interrelated, so changing one of the three gains directly affects the other two control actions.

4.2 Gain tuning of the conventional PID controller

In the previous chapter, the three gains K_p, K_i, K_d that affect the structure of the PID controller and the performance of the feedback system have been examined. The process of appropriately obtaining this through analytical or experimental/empirical methods is called tuning.

The tuning of PID controller can be divided into empirical tuning method which does not require the mathematical model of a controlled system and tuning method based on a model. Ziegler-Nichols (Z-N) method is the representative tuning method for the former, and the internal model control (IMC) method is for the latter.

4.2.1 Ziegler-Nichols tuning method

In 1943, Ziegler-Nichols [56] proposed a rule to determine the proportional gain K_p, the integral time T_i, and the derivative time T_d based on the transient response characteristics of the controlled system. This method is still widely used in the design of most PID controllers because of the advantage of the non-model technique. The Ziegler-Nichols tuning rule has two methods: an open-loop method performed off-line and a closed-loop method performed with the controller mounted on the plant. They aim to reduce overshoot by 25 [%] in the step response.

(1) Open-loop method

This method first empirically obtains the response to the unit step input of the plant. Most industrial plants are expressed as an S-curve shaped response curve, that is, the first-order plus time delay (FOPTD) type as shown in Equation (4.5). If a unit-step response is not S-curve because of containing an integrator or major dominant complex-conjugate poles in the controlled system, this cannot be applied to the open-loop method.

$$\frac{Y(s)}{U(s)} = \frac{Ke^{-Ls}}{1+\tau s} \tag{4.5}$$

where K is the steady-state gain, L is the time delay, and τ is the time constant.

If an S-curve as Figure 4.5 is obtained, K, L and τ can be obtained from the magnitude ratio of the steady-state response $y(\infty)$ to the magnitude of the input u, an intersection point where the tangent at the inflection point of the curve meets the time axis and an intersection point where a line drawn from the point where the tangent line and the steady-state gain K meets the time axis, respectively.

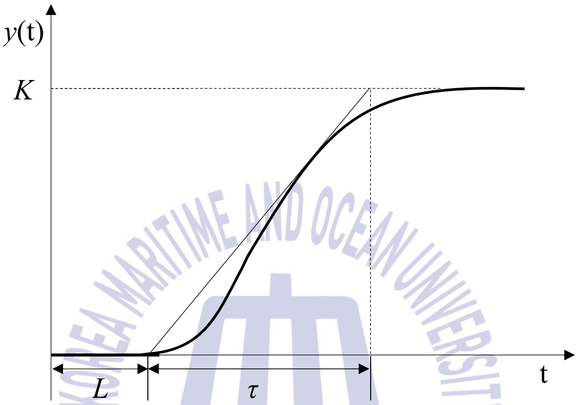

Figure 4.5 Response curve for unit-step input

If K, τ, L values are derived, the coefficients are obtained from Table 4.2. This method has the disadvantage that τ and L are not uniformly determined when the controlled system is higher degree, and field experience is required at this time.

Table 4.2 PID controller tuning rules by the open-loop method

Controllers	Parameters		
	K_p	T_i	T_d
P	$\frac{\tau}{KL}$	-	-
PI	$0.9\frac{\tau}{KL}$	$3.3L$	-

PID	$1.2\dfrac{\tau}{KL}$	$2.0L$	$0.5L$

(2) Closed-loop method

As shown in Figure 4.6, this method constructs a feedback control system only with proportional control (set as $T_i = \infty$, $T_d = 0$) and finds K_p that output y oscillates at a constant amplitude while gradually increasing K_p from zero.

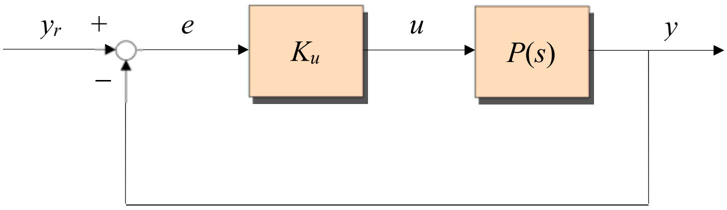

Figure 4.6 Closed-loop control system with proportional gain

The proportional gain K_p when the response curve oscillates at a constant amplitude is called the ultimate gain K_u and the period when the periodic oscillation occurs is called the ultimate period P_u. Figure 4.7 shows the measurement of P_u from the response curve.

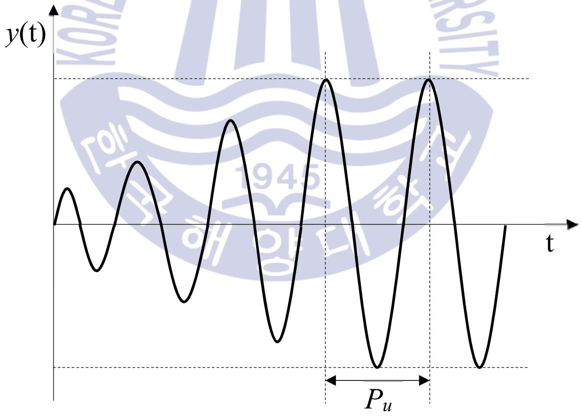

Figure 4.7 Response curve and ultimate period

Once K_u and T_u are obtained, the parameters are obtained in Table 4.3.

Table 4.3 PID controller tuning rules by the closed-loop method

Controllers	Parameters		
	K_p	T_i	T_d
P	$\frac{K_u}{2}$	-	-
PI	$\frac{K_u}{2.2}$	$\frac{P_u}{1.2}$	-
PID	$\frac{K_u}{1.7}$	$\frac{P_u}{1.2}$	$\frac{P_u}{8}$

This method has a disadvantage of taking much time because it derives ultimate gain and ultimate period by trial and error, and it is also not easy to continue to oscillate from the actual controlled system to the limited stability.

A method of easily obtaining the ultimate gain and ultimate period by compensating for the disadvantage of the above method is the relay feedback control as shown in Figure 4.8. The periodic oscillation occurs when replacing the proportional controller in Figure 4.6 with a finite-size relay, and ultimate gain and ultimate period can be obtained from the amplitude and cycle of the output signal obtained from periodic oscillation. For more information, see Reference [55].

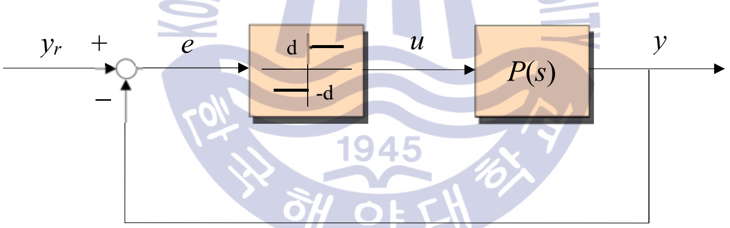

Figure 4.8 Relay feedback control system

4.2.2 Tyreus-Luyben tuning method

In 1992, Tyreus-Luyben [55] proposed a rule to determine K_p, T_i, and T_d based on the transient response characteristics of the controlled system as Ziegler-Nichols's closed-loop method. This method first constructs a closed-loop system with only a proportional gain K_p. Then, the proportional gain K_p is increased until it reaches to the ultimate gain K_u as Figure 4.6, at which the output of the control loop oscillates with a constant amplitude. After the ultimate period P_u is obtained from the response depicted in Figure 4.7, the controller parameters are tuned by applying the rules in Table 4.4.

Table 4.4 Tyreus-Luyben's tuning rules for PI and PID controller

Controllers	Parameters		
	K_p	T_i	T_d
PI	$\frac{K_u}{3.2}$	$2.2P_u$	-
PID	$\frac{K_u}{2.2}$	$2.2P_u$	$\frac{P_u}{6.3}$

4.3 Practical PID controller

The disadvantage of ideal derivative action used in existing PID controllers is that they have very high gain for high frequency signals [12]. The magnitude of the frequency transfer function of Equation (4.2d) is equal to that of Equation (4.6), and Figure 4.9 shows its frequency response with K_d= 1.

$$\frac{|U_d(j\omega)|}{|E(j\omega)|} = K_d\omega \tag{4.6}$$

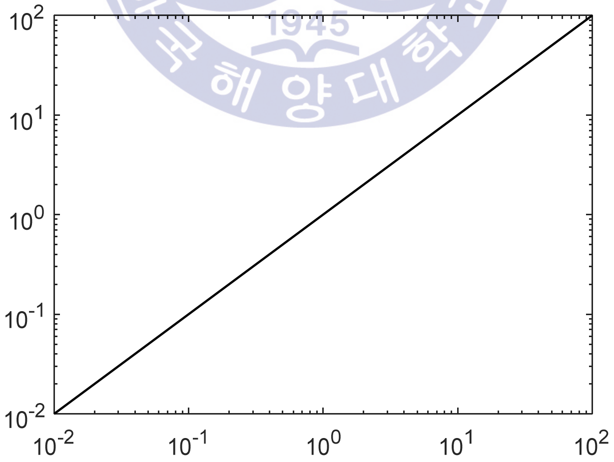

Figure 4.9 Frequency response of the ideal derivative action

The figure shows that $|U_d(j\omega)|/|E(j\omega)|$ increases in proportion to ω. That is, this means that when the output y is measured and gives feedback to controller, if the noise is mixed into feedback signal, there is noise in the error $e= y_r-y$, and if the noise is high frequency, it can produce a larger change in derivative action in proportion to the frequency. To compensate for this, the on-site PID controller uses an equation such as Equation (4.7). This type can mitigate the derivative kick that may occur in ideal derivative action.

$$\frac{T_d}{N}\dot{u}_d(t)+u_d(t)=K_d\dot{e}(t) \tag{4.7}$$

The following equation is obtained by expressing Equation (4.7) in the frequency domain.

$$U_d(s)=\frac{K_d s}{1+\frac{T_d}{N}s}E(s) \tag{4.8}$$

where N is the maximum derivative gain, which is empirically determined between 2 and 20 [12]. This can be interpreted as an ideal derivative filtered using a first order system with a time constant T_d/N. It can be seen that if N is increased, it can be approximated to K_ds, a transfer function of ideal derivative action.

The magnitude of the frequency transfer function of Equation (4.8) is equal to Equation (4.9).

$$\frac{|U_d(j\omega)|}{|E(j\omega)|}=\frac{K_d\omega}{\sqrt{1+(\frac{T_d}{N}\omega)^2}} \tag{4.9}$$

In the above equation, if $\omega ? \frac{N}{T_d}$, high-frequency gain is approximated as follows:

$$\frac{|U_d(j\omega)|}{|E(j\omega)|} = \frac{K_d\omega}{\frac{T_d}{N}\omega} = \frac{K_pT_d\omega}{\frac{T_d}{N}\omega} = K_pN \tag{4.10}$$

Figure 4.10 shows the frequency response for different N with K_p= 1, T_d= 10 in Equation (4.9).

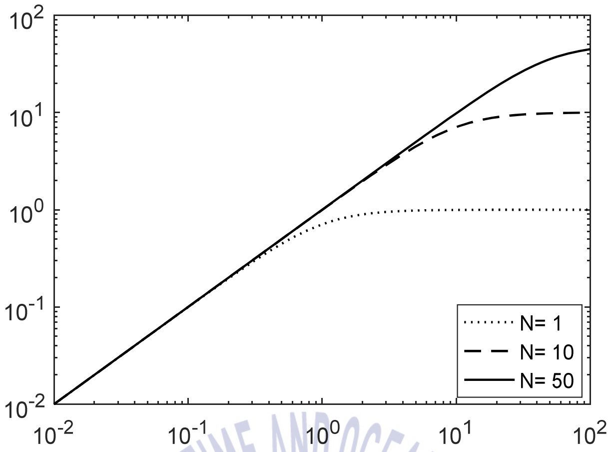

Figure 4.10 Frequency responses of the practical derivative action

The influence of the measurement noise can be removed to some extent by performing a derivative action such as Equation (4.7). In the case of N= 1 in Figure 4.10, the practical derivative action behaves like an ideal derivative action for low-frequency signals up to N/T_d= 1/10= 0.1[rad/sec], and the high frequency gain is limited to K_pN= 1×1= 1 for frequency signals higher than that. It can be seen that as N becomes larger, N/T_d and K_pN increase as well.

The transfer function of a PID controller with the practical derivative action can be written as Equation (4.11).

$$\frac{U(s)}{E(s)} = K_p + \frac{K_i}{s} + \frac{K_d s}{1 + \frac{T_d}{N}s} \tag{4.11a}$$

$$= K_p(1 + \frac{1}{T_i s} + \frac{T_d s}{1 + \frac{T_d}{N}s}) \tag{4.11b}$$

Meanwhile, it is also possible to filter the measured signal instead of derivative filtering and to apply it to an ideal PID controller. When using a secondary filter with a damping coefficient $\zeta = 1/\sqrt{2}$, the transfer function of a similar PID controller is given as Equation (4.12).

$$\frac{U(s)}{E(s)} = (K_p + \frac{K_i}{s} + K_d s)\frac{1}{1 + T_f s + T_f^2 s^2 / 2} \tag{4.12a}$$

$$= K_p(1 + \frac{1}{T_i s} + T_d s)\frac{1}{1 + T_f s + T_f^2 s^2 / 2} \tag{4.12b}$$

where the filter time constant T_f is typically chosen at T_d/N for PID control and the range of N is 2~20 [35].

4.4 Existing nonlinear PID controllers

Since PID control determines the output of the controller through three combined operations of proportional, integral, and derivative, which are important factors that determine the performance for the error between the set-point and output, precise tuning of the controller parameters is very important to achieve the desired performance. The conventional PID controller has a disadvantage in that, even if these parameters are correctly tuned, the controller should be re-tuned if the controlled system changes due to a change in the operating condition etc. Therefore, when controlling a controlled system with non-linearity and time-variability, the conventional PID controller is bound to have a limitation in its function. Therefore, various techniques of combining AI (artificial intelligence) techniques such as adaptive technique, gain scheduling, fuzzy, neural network, and evolutionary algorithm have been studied to improve the adaptability and robustness of the controller, and one of them is the Nonlinear PID (NPID) control technique.

The NPID control technique has been established as one of the simple and effective technique based on the conventional PID controller frame. The proposed techniques can be classified into two categories. One is a technique of nonlinearly changing the three gains of the conventional PID controller according to the rate of change of error and error [41-44] and the other is a techniques of nonlinearly scaling the error between the set-point and output, and inputting this scaled error into the conventional PID controller frame [45-47]. Here, two representative techniques are explained as below.

4.4.1 Seraji's NPID controller

Seraji proposes a nonlinear PID (NPID) controller with nonlinear gain $k(\cdot)$ coupled in series with a conventional PID controller with fixed gain, and the following equation shows this [45].

$$u(t) = K_p[k(e)e(t)] + K_i \int_0^t [k(e)e(\tau)]d\tau + K_d \frac{d[k(e)e(t)]}{dt} \tag{4.13}$$

where K_p, K_i, and K_d are the proportional gain, integral gain, and derivative gain of the PID controller with fixed gain, respectively, and nonlinear gain $k(e)$ is a function of $e(t)= y_r(t)-y(t)$ and operates to produce a scaled error. Figure 4.11 shows the block diagram of the NPID controller proposed by Seraji. In this NPID controller, the error $v(t)$ scaled by $k(\cdot)$ is input to the PID controller to obtain the control input $u(t)$.

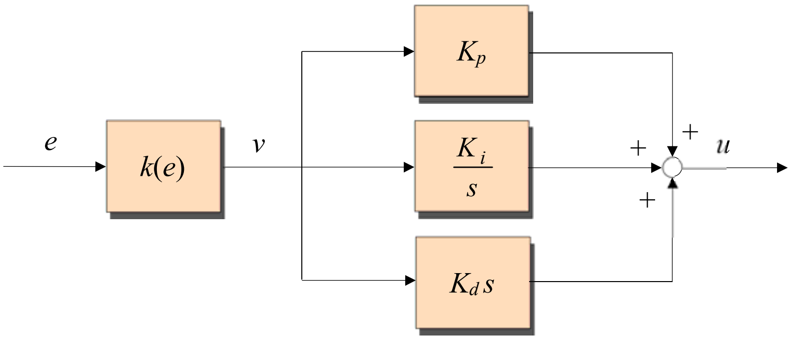

Figure 4.11 Block diagram of the Seraji's NPID controller

The nonlinear gain $k(e)$ can be arbitrary nonlinear function satisfying the condition of $0 \le k(e) \le k_{max}$. Seraji proposed three nonlinear functions including sigmoid function, hyperbolic function, and piecewise-linear function, and only the two functions are examined.

The first function is the following sigmoid function.

$$k(e) = k_0 + k_1\{\frac{2}{1+\exp(-k_2 e)} - 1\} \tag{4.14}$$

where k_0, k_1, and k_2 are positive constants defined by the user. Figure 4.12 shows the shape of this function.

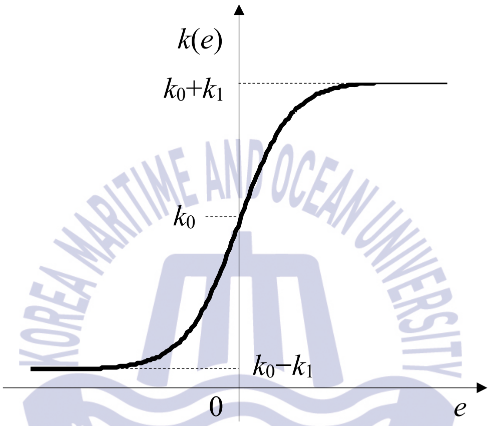

Figure 4.12 $k(e)$ versus e

When $e = -\infty$, $k(e)$ has a lower limit of $k_{min} = k_0 - k_1$ and has an upper limit of $k_{max} = k_0 + k_1$ when $e = +\infty$, and $k(e) = k_0$ when $e = 0$. As shown above, k_0 defines the center value of $k(e)$, k_1 determines the range of $k(e)$, and k_2 specifies the rate of change of $k(e)$.

The second is the use of the hyperbolic function:

$$k(e) = k_0 + k_1\{1 - \frac{2}{\exp(k_2 e) + \exp(-k_2 e)}\} \tag{4.15}$$

where k_0, k_1 and k_2 are positive constants.

Figure 4.13 shows the shape of this function, which is an inverted bell-shaped curve. The upper limit value of $k(e)$ is $k_{max}= k_0+k_1$ when $e= \pm\infty$ and the lower limit value is $k_{min}= k_0$ when e=0. As shown above, k_0 defines the minimum value of $k(e)$, k_1 represents the range, and k_2 specifies the rate of change of $k(e)$. This equation is an even function with $k(e)= k(-e)$ and can be applied when a function for the absolute value error $|e|$ is needed.

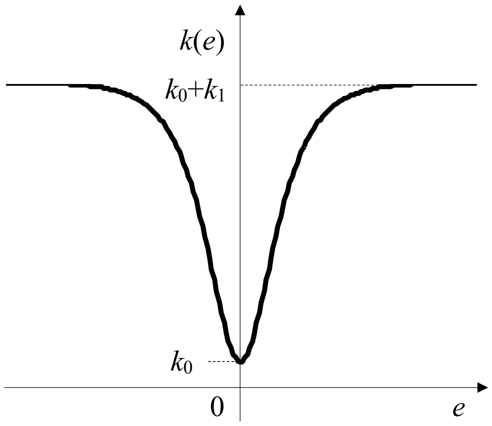

Figure 4.13 $k(e)$ versus e

In general, the main role of the integral action is to reduce the steady-state deviation. Therefore, it is necessary to decrease the value of integral action when the error is large, and to increase it when the error is small. On the contrary, the proportional action and derivative action are required to reduce error so as not to be sensitive to noise when the error is small, that is, when the output reaches the vicinity of the set-point. As can be seen in Figure 4.11, the disadvantage is that the characteristic role of the three actions is not considered because Seraji's method is scaled error by applying the same nonlinear function and the output of the controller is calculated by multiplying this scaled error by proportional gain, integral gain, derivative gain. The results can be seen in the response simulation of Chapter 7.

4.4.2 Korkmaz's NPID controller

The method proposed by Korkmaz et al. [41] is to use Equation (4.16) which nonlinearly changes the three gains in the structure of the conventional PID controller

$$u(t) = K_p(e)e(t) + K_i(e)\int_0^t e(\tau)d\tau + K_d(e)\frac{de(t)}{dt} \tag{4.16}$$

Equation (4.16) can be expressed as the format of a transfer function as follows.

$$\frac{U(s)}{E(s)} = K_p(e) + \frac{K_i(e)}{s} + K_d(e)s \tag{4.17}$$

where $K_p(e)$, $K_i(e)$ and $K_d(e)$ are time-varying gains, which mean proportional gain, integral gain and derivative gain, respectively, and these are characterized by the function of the error $e(t)$. Figure 4.14 shows the block diagram of the NPID controller proposed by Korkmaz et al.

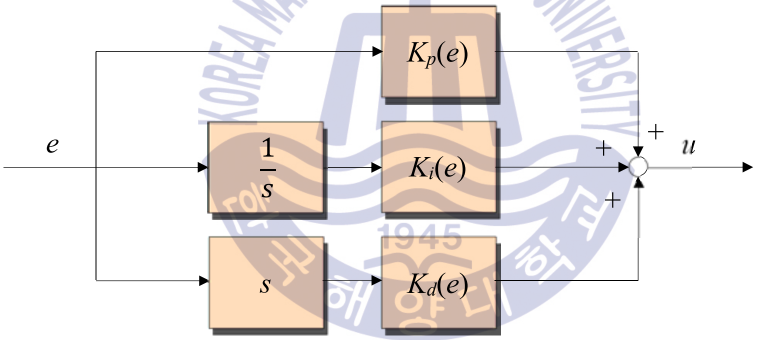

Figure 4.14 Block diagram of the Korkmaz's NPID controller

The proportional gain accelerates the response of controlled system and reduces the settling time, but if it is too large, the system becomes unstable. Integral gain removes a steady-state error, but if this value is too large, it causes vibration and increase overshoot. Derivative gain reduces vibration and overshoot. Considering this, Korkmaz et al. proposed the gains $K_p(e)$, $K_i(e)$ and $K_d(e)$ depending on the magnitude of $e(t)$, which is based on the nonlinear function $f(\cdot)$.

$$K_p(e) = \mathrm{a}_1 + \mathrm{a}_2 f(e) \tag{4.18a}$$

$$K_i(e) = b_1 - b_2 f(e) \tag{4.18b}$$

$$K_d(e) = c_1 + c_2 f(e) \tag{4.18c}$$

where parameters a_1, a_2, b_1, b_2, c_1, and c_2 are positive constants appropriately adjusted by the user, and $f(\cdot)$ has the same shape as Figure 4.15 as the Gaussian error function of Equation (4.19).

$$f(e) = erf(e) = \frac{2}{\sqrt{\pi}} \int_0^e \exp(-t^2) dt \tag{4.19}$$

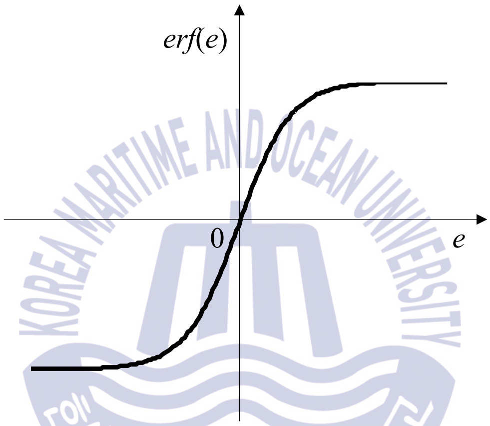

Figure 4.15 Gaussian error function

In order to prevent the PID gain from having a negative value, Korkmaz et al. used the absolute value of the error $|e|$ instead of e, which causes $f(e)$ to use only the positive domain of the *erf* function. Figure 4.16 shows the changes in the nonlinear gain values according to the changes in error especially when all of a_1, a_2, b_1, b_2, c_1, c_2 have a value of 1.

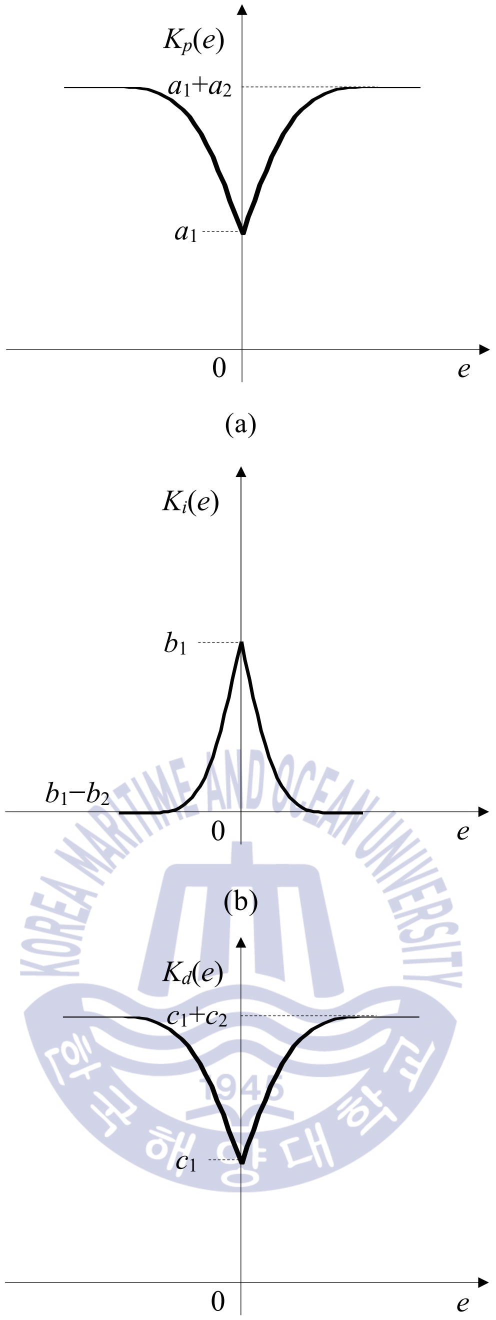

(c)

Figure 4.16 Nonlinear gains proposed by Korkmaz's NPID controller

The figure shows that both proportional gain $K_p(e)$ and the derivative gain $K_d(e)$ increase when the absolute value of the error increases pivot on e= 0. On the other hand, the integral gain $K_i(e)$ increases to reduce the steady-state deviation when the absolute value of the error becomes small. Thus, the minimum and maximum values of $K_p(e)$ are a_1 and a_1+a_2, respectively and the minimum and maximum values of $K_i(e)$ are b_1-b_2 and b_1, respectively and the minimum and maximum values of $K_d(e)$ are c_1 and c_1+c_2, respectively. As shown in Equation (4.18), the NPID controller proposed by Korkmaz et al. has disadvantages that there are six parameters that make tuning difficult and it is also difficult to interpret the stability of the entire feedback system by introducing three different nonlinear functions.

Chapter 5. Suggestion of the Proposed Nonlinear PID Controllers

This chapter proposes two types of NPID controllers to complement the disadvantages of existing NPID controller indicated in Chapter 4. One introduces nonlinear functions for the three proportional, integral, and derivative controllers (Fully-nonlinear PID controller), and the other includes a nonlinear function only for the integral controller (Partially-nonlinear PID controller). The controller parameters are tuned optimally using a genetic algorithm.

5.1 Fully-nonlinear PID controller

The error between the set-point (or reference input) and output (or the measured output) is scaled nonlinearly, and input into the controller to derive proportional, integral, and derivative actions. This type of controller is here called the Fully-Nonlinear PID (F-NPID) controller. The F-NPID controller is composed of P, I, and D blocks, and Figure 5.1 shows the structure.

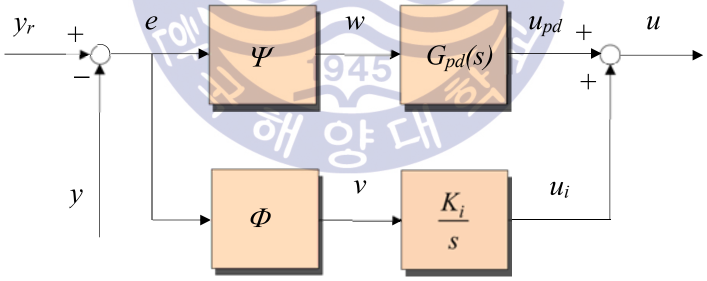

Figure 5.1 Structure of the F-NPID controller (Ψ and Φ are nonlinear functions)

5.1.1 Nonlinear P block

The magnitude of the proportional action u_p changes in proportion to the proportional gain or error, and if it is too large, overshoot and oscillation may occur. When the error is large, the proportional action will be large in order to increase the response speed. However, the large proportional action may continue even after the response reaches a steady-state if the proportional gain is set to be large. With this in mind, the P block uses a nonlinearly scaled error that is appropriately sized to a nonlinear function as follows.

$$u_p(t) = K_p w(t) \tag{5.1}$$

$$w(t) = \Psi(e(t)) \tag{5.2}$$

where, w is a nonlinearly scaled error, e is the error between the set-point (or reference input y_r) and output y, K_p is the proportional gain, and Ψ is the nonlinear function of the error.

The nonlinear function Ψ used to scale the error is implemented as a Takagi-Sugeno (T-S) type fuzzy model [70], and the rules are given by

$$\mathrm{R}_1\text{: if } e(t) \text{ is } F_1(e)\text{, then } \Psi_1(e(t)) = k_2 e(t) \tag{5.3a}$$

$$\mathrm{R}_2\text{: if } e(t) \text{ is } F_2(e)\text{, then } \Psi_2(e(t)) = k_1 e(t) \tag{5.3b}$$

$$\mathrm{R}_3\text{: if } e(t) \text{ is } F_3(e)\text{, then } \Psi_3(e(t)) = k_2 e(t) \tag{5.3c}$$

where, the error is the input of the fuzzy system, the nonlinear function Ψ_i (i= 1, 2, 3) is the output of each rule. k_1 and k_2 are positive and user-defined gains with a relationship of $0 \le k_1 \le k_2$. Meanwhile, the membership functions of the fuzzy sets $F_1(e)$, $F_2(e)$, $F_3(e)$ used in the fuzzy partition of the error are defined as follows, and Figure 5.2 shows the shapes of these.

$$F_1(e) = \begin{cases} 1 \quad , & e \le -3\sigma \\ -e/3\sigma, & -3\sigma < e \le 0 \\ 0 \quad , & elsewhere \end{cases} \tag{5.4a}$$

$$F_2(e) = \exp\left(-\frac{e^2}{2\sigma^2}\right) \tag{5.4b}$$

$$F_3(e) = \begin{cases} e/3\sigma, & 0 \le e < 3\sigma \\ 1 \quad , & e \ge 3\sigma \\ 0 \quad , & elsewhere \end{cases} \tag{5.4c}$$

where σ is the standard deviation of the membership function $F_2(e)$ and is a user-defined gain.

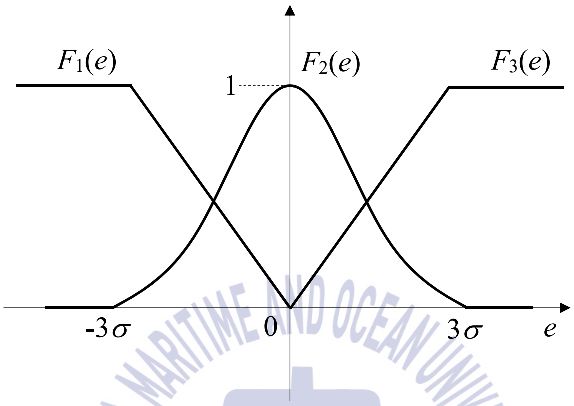

Figure 5.2 Fuzzy partition of the error e

If the error is given, the nonlinear function Ψ is calculated as follows.

$$\Psi_i(e(t)) = \frac{\alpha_1\Psi_1(e(t)) + \alpha_2\Psi_2(e(t)) + \alpha_3\Psi_3(e(t))}{\alpha_1 + \alpha_2 + \alpha_3}$$

$$= \frac{\alpha_1 k_2 + \alpha_2 k_1 + \alpha_3 k_2}{\alpha_1 + \alpha_2 + \alpha_3} e(t) \tag{5.5}$$

where $\alpha_i = F_i(e)$ (i= 1, 2, 3) is the degree of membership of each fuzzy set corresponding to the error. And Equation (5.5) gives the following nonlinear gain.

$$k(e) = \frac{\Psi_i(e(t))}{e(t)} = \frac{\alpha_1 k_2 + \alpha_2 k_1 + \alpha_3 k_2}{\alpha_1 + \alpha_2 + \alpha_3} \tag{5.6}$$

The shape of the nonlinear gain $k(e)$ changes according to the values of k_1, k_2 and σ. Figures 5.3-5.4 show the graph when they have specific values. In Figure 5.3, $k(e)$ converges to the upper limit k_2 when the error increases and converges to the lower limit k_1 when the error approaches zero. The width of the function is narrower and wider as σ is smaller and larger, respectively.

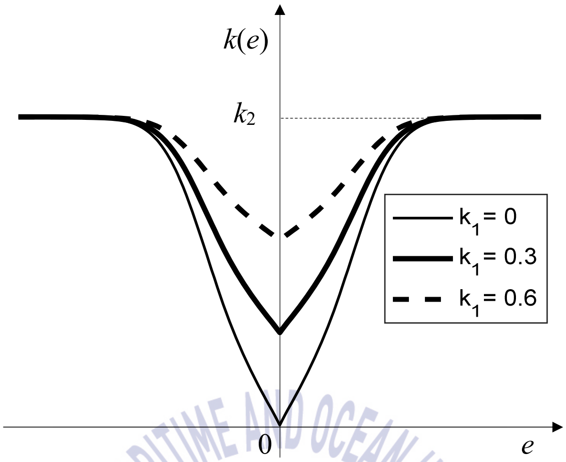

Figure 5.3 Shapes of $k(e)$ according to the change of k_1 (k_2= 1 and σ= 0.2)

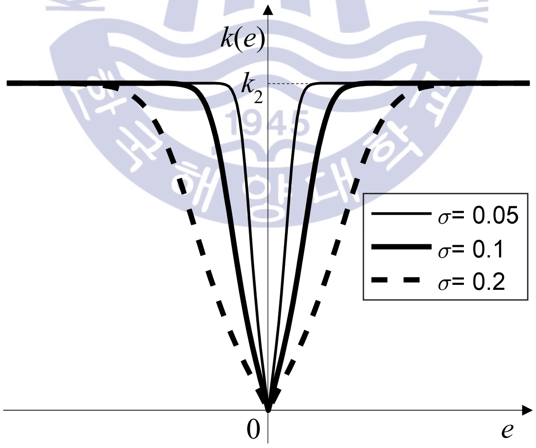

Figure 5.4 Shapes of $k(e)$ according to the change of σ (k_1= 0 and k_2= 1)

Meanwhile, Figure 5.5 shows the slope of the nonlinearly scaled error $w(t)= \Psi(e(t))$ in Equation (5.2) according to the change of error.

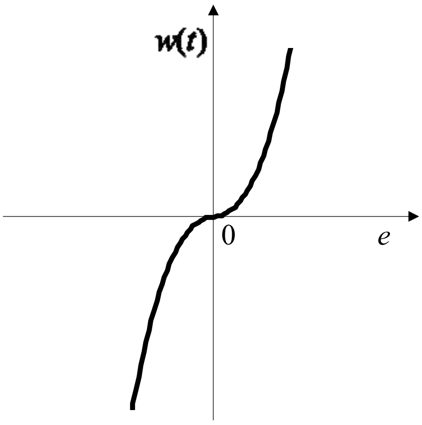

(a) k_1= 0 and k_2= 1

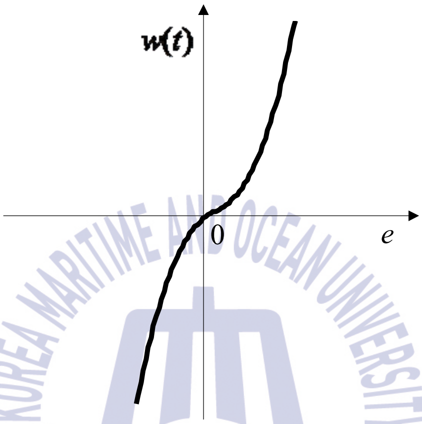

(b) k_1= 0.1 and k_2= 1

Figure 5.5 Shapes of $w(t)= \Psi(e(t))$

It can be seen that it always exists in the first and third quadrant as long as k_1 and k_2 have positive values.

5.1.2 Nonlinear D block

The derivative action u_d increases in proportion to the error rate and derivative gain, and brakes in anticipation that the output will increase as u_p and u_i increase. The D block has a structure in which the error is scaled by using the nonlinear function Ψ used in the proportional block, and the derivative action with the first filter term is coupled in series to mitigate the derivative kick as follows.

$$T_f \dot{u}_d(t) + u_d(t) = K_d \dot{w}(t) \tag{5.7}$$

where, K_d is the derivative gain, $T_f = K_p/(NK_d)$ is the filter time constant, and the maximum derivative gain N is a empirically determined constant and N= 10 is used in this thesis [12].

Thus, the following transfer function can be obtained for the proportional and derivative actions.

$$G_{pd}(s) = \frac{U_{pd}(s)}{W(s)} = K_p + \frac{K_d s}{1+T_f s} \tag{5.8}$$

5.1.3 Nonlinear I block

The integral action u_i increases if the absolute value of the cumulative error is larger or the integral time is shorter. When the error is small, the proportional action u_p no longer affects the system. Thus, u_i plays a role of eliminating the steady-state error because it continuously accumulates and controls the error. But, when the set-point is increased suddenly or a large disturbance is imposed, overshoot may occur because the error and cumulative error become large.

Thus, it is necessary to reduce the cumulative error to prepare for occurrence of overshoot when the error is large. When the error is small, it is necessary to increase the cumulative error so that the steady-state error is eliminated quickly.

Given this fact, the I block uses a nonlinearly scaled error that is appropriately sized to a nonlinear function as follows.

$$u_i(t) = K_i \int v(t)dt \tag{5.9}$$

$$v(t) = \Phi(e(t)) \tag{5.10}$$

where v is a nonlinearly scaled error, K_i is the integral gain, and Φ is the nonlinear function of the error.

The nonlinear function Φ used to scale the error is implemented as a Takagi-Sugeno (T-S) fuzzy model [70], and the rules are given by

$$\mathrm{R}_1\text{: if } e(t) \text{ is } F_1(e)\text{, then } \Phi_1(e(t)) = k_1 e(t) \tag{5.11a}$$

$$\mathrm{R}_2\text{: if } e(t) \text{ is } F_2(e)\text{, then } \Phi_2(e(t)) = k_2 e(t) \tag{5.11b}$$

$$\mathrm{R}_3\text{: if } e(t) \text{ is } F_3(e)\text{, then } \Phi_3(e(t)) = k_1 e(t) \tag{5.11c}$$

where, the error is the input of the fuzzy system, nonlinear function Φ_i (i= 1, 2, 3) is the output of each rule. k_1 and k_2 are positive and user-defined gains with a relationship of $0 \leq k_1 \leq k_2$ as same as Equation (5.3). Meanwhile, the membership function of the fuzzy sets $F_1(e)$, $F_2(e)$, $F_3(e)$ used in the fuzzy partition of e are as same as Equation (5.4) previously.

When the error is given, the nonlinear function Φ is calculated as follows.

$$\begin{aligned} \Phi_i(e(t)) &= \frac{\alpha_1 \Phi_1(e(t)) + \alpha_2 \Phi_2(e(t)) + \alpha_3 \Phi_3(e(t))}{\alpha_1 + \alpha_2 + \alpha_3} \\ &= \frac{\alpha_1 k_1 + \alpha_2 k_2 + \alpha_3 k_1}{\alpha_1 + \alpha_2 + \alpha_3} e(t) \end{aligned} \tag{5.12}$$

where, $\alpha_i = F_i(e)$ (i= 1, 2, 3) is the degree of membership of each fuzzy set corresponding to the error. α_i is always established as a relationship of $\alpha_1+\alpha_2+\alpha_3 \neq 0$ when defining a fuzzy set. The nonlinear gain $k(e)$ is expressed as the following equation.

$$k(e) = \frac{\Phi_i(e(t))}{e(t)} = \frac{\alpha_1 k_1 + \alpha_2 k_2 + \alpha_3 k_1}{\alpha_1 + \alpha_2 + \alpha_3} \tag{5.13}$$

The shape of the nonlinear gain $k(e)$ changes according to k_1, k_2 ($0 \leq k_1 < k_2$) and σ.

Figures 5.6-5.7 show this. In Figure 5.6, $k(e)$ converges to the lower limit value k_1 when the error becomes infinite, and converges to the upper limit value k_2 when the error approaches 0. In Figure 5.7, the width of the function is narrower and wider as σ is smaller and larger, respectively.

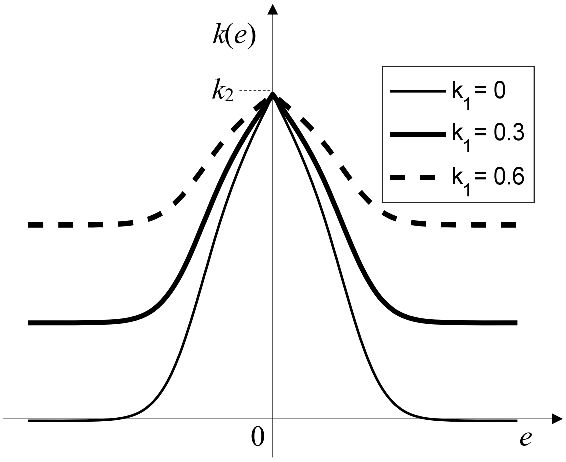

Figure 5.6 Shapes of $k(e)$ to change of k_1 (k_2= 1 and σ= 0.2)

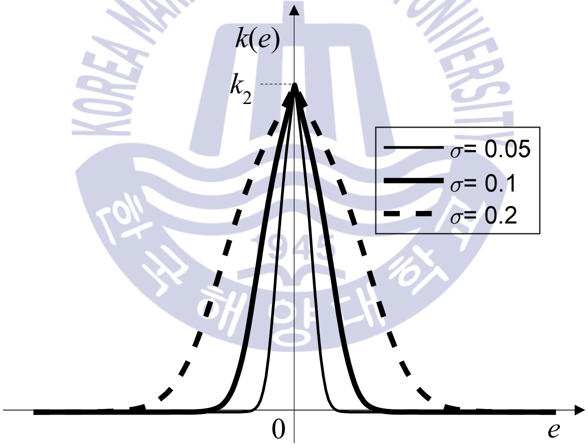

Figure 5.7 Shapes of $k(e)$ to change of σ (k_1= 0 and k_2= 1)

Meanwhile, Figure 5.8 shows the slope of the nonlinearly scaled error $v(t)= \Phi(e(t))$ in Equation (5.12) according to the change of error.

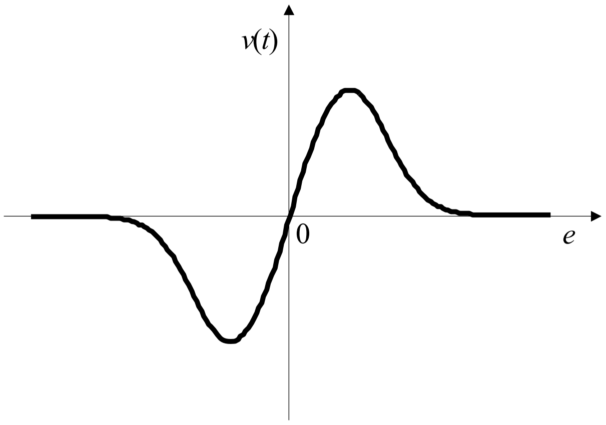

(a) k_1= 0 and k_2= 1

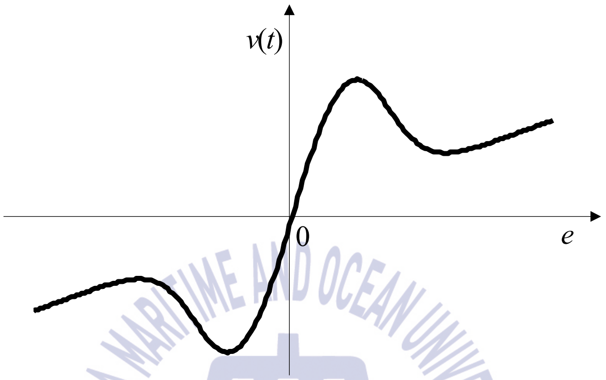

(b) k_1= 0.1 and k_2= 1

Figure 5.8 Shapes of $v(t)= \Phi(e(t))$

It can be also seen that it always exists in the first and third quadrant as long as k_1 and k_2 have positive values.

5.1.4 Relationship between Ψ and Φ

Two nonlinear functions Ψ and Φ are used in the F-NPID controller as shown in Figure 5.1. But they are defined as Equations (5.3), (5.11), so it is possible to describe them as one nonlinear function Φ. The following theorem is established between Equations (5.5) and (5.12), as it can be inferred from Figures 5.3 and 5.6.

Theorem 4.1 (relationship between Ψ and Φ) The following relationship is established between the two nonlinear functions $\varPsi$ and $\varPhi$ defined in Equations (5.5) and (5.12).

$$\varPsi(e(t)) = (k_1 + k_2)e(t) - \varPhi(e(t)) \tag{5.14}$$

Proof: Adding and subtracting $(k_1+k_2)(\alpha_1+\alpha_2+\alpha_3)$ at the numerator of Equation (5.5)

$$\varPsi(e(t)) = \frac{(k_1+k_2)(\alpha_1+\alpha_2+\alpha_3)-(k_1+k_2)(\alpha_1+\alpha_2+\alpha_3)+\alpha_1 k_2+\alpha_2 k_1+\alpha_3 k_2}{\alpha_1+\alpha_2+\alpha_3}e(t)$$

and Equation (5.5) gives the following relation.

$$\begin{aligned}\varPsi(e(t)) &= \frac{(k_1+k_2)(\alpha_1+\alpha_2+\alpha_3)-\alpha_1 k_1-\alpha_2 k_2-\alpha_3 k_1}{\alpha_1+\alpha_2+\alpha_3}e(t)\\ &= (k_1+k_2)e(t)-\frac{\alpha_1 k_1+\alpha_2 k_2+\alpha_3 k_1}{\alpha_1+\alpha_2+\alpha_3}e(t)\\ &= (k_1+k_2)e(t)-\varPhi(e(t))\end{aligned}$$

Therefore, from the relationship in Equation (5.14), the block diagram of the modified F-NPID controller shown in Figure 5.1 can be expressed as Figure 5.9 using one nonlinear function $\varPhi$.

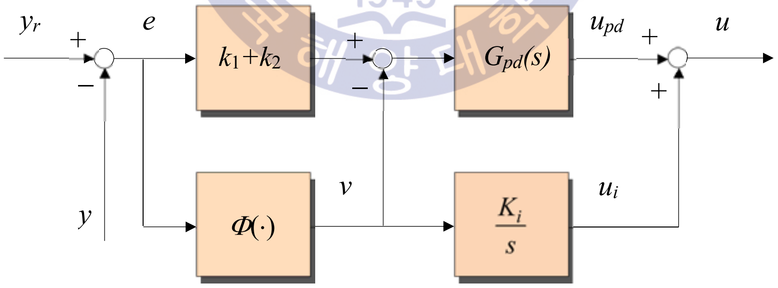

Figure 5.9 Block diagram of the modified F-NPID controller

5.2 Partially-nonlinear PID controller

The F-NPID controller has K_p, K_i, K_d, σ, k_1 (k_2 is set to 1 in Chapter 6) as user-defined gains. This can be a disadvantage because of having two more parameters than the existing PID controller. Thus, a nonlinear controller called Partially-nonlinear PID (P-NPID) controller that includes a nonlinear function only for the integral action is proposed.

The proportional and derivative actions are a system that responds immediately according to the input signal which is the magnitude of the error and the error rate, respectively. While, the integral action is a system that the input signal from the past to the present are accumulated to have the current output. This means that, the accumulated control signals during the specific time affects the integral action of the next time. Particularly, if the set-point is largely changed or a large disturbance occurs or a time delay element exists in the controlled system, the influence of the integral action becomes more excessive.

Thus, the P-NPID controller consists of a linear PD block to respond immediately according to the input signal and a nonlinear I block to adjust only for the integral action appropriately. Figure 5.10 shows the structure of the P-NPID controller.

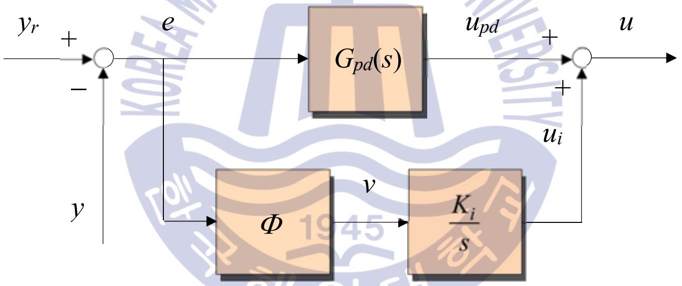

Figure 5.10 Structure of the P-NPID controller (Φ is a nonlinear function)

5.2.1 Linear PD block

The PD block has a structure composed of a combination of the conventional linear proportional and derivative action having the filter time constant. It is displayed in the time domain as follows.

$$u_p(t) = K_p e(t) \tag{5.15a}$$

$$T_f \dot{u}_d(t) + u_d(t) = K_d \dot{e}(t) \tag{5.15b}$$

$$u_{pd}(t) = u_p(t) + u_d(t) \tag{5.15c}$$

Again, this can be expressed as the following transfer function.

$$G_{pd}(s) = \frac{U_{pd}(s)}{E(s)} = K_p + \frac{K_d s}{1 + T_f s} \tag{5.16}$$

where, K_p and K_d are the proportional and derivative gains, respectively. $T_f = K_p/(NK_d)$ is the filter time constant, and N is the empirically determined constant.

5.2.2 Nonlinear I block

The nonlinear I block of the P-NPID controller uses the same one described in Section 5.1.3.

5.3 Feedback control systems

5.3.1 Modified F-NPID control system

The block diagram of the overall control system including the F-NPID controller and the controlled system discussed above is shown in Figure 5.11.

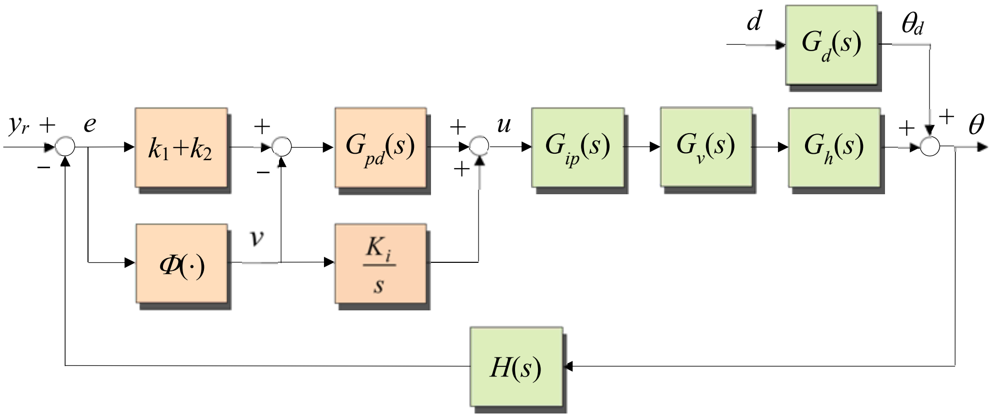

Figure 5.11 Overall modified F-NPID control system

If a ship departs from the port and sails along a constant speed, the main engine will run at a constant speed. So, the controller is considered to be a feedback regulator with $y_r = 0$. And if the influence of disturbance is not significant, it can be ignored ($\theta_d = 0$), the block diagram of Figure 5.11 can be simplified as follows:

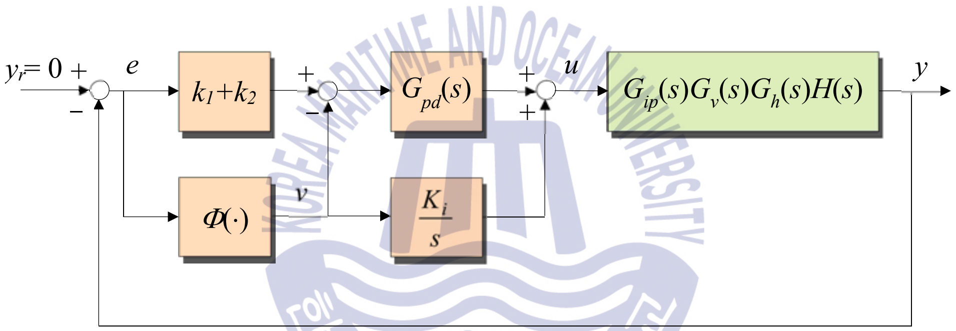

Figure 5.12 Overall modified F-NPID control system when $y_r = 0$ and $\theta_d = 0$

Based on this, the input/output relationship of the linear block from v to y can be expressed as a transfer function, which can be written as

$$Y(s) = G_{ip}(s)G_v(s)G_h(s)H(s)\{\frac{K_i}{s}V(s) + G_{pd}(s)[-(k_1+k_2)Y(s) - V(s)]\} \qquad (5.17)$$

If substituting and summarizing each transfer function discussed in Chapters 4 and 5, $G(s) = Y(s)/V(s)$ is expressed as the following equation.

$$G(s)=\frac{G_{ip}(s)G_v(s)G_h(s)H(s)[K_i-sG_{pd}(s)]}{s[1+(k_1+k_2)G_{pd}(s)G_{ip}(s)G_v(s)G_h(s)H(s)]}=\frac{N(s)}{D(s)} \tag{5.18a}$$

$$N(s)=G_{ip}(s)G_v(s)G_h(s)H(s)[K_i-sG_{pd}(s)]=n_0s^3+n_1s^2+n_2s+n_3 \tag{5.18b}$$

$$\begin{aligned} D(s)&=s[1+(k_1+k_2)G_{pd}(s)G_{ip}(s)G_v(s)G_h(s)H(s)] \\ &=s(s^5+d_1s^4+d_2s^3+d_3s^2+d_4\,\mathrm{s}+d_5) \end{aligned} \tag{5.18c}$$

where the parameters of the polynomial are given as follows.

$$n_0=\frac{K_{ip}K_vK_hK_s(K_pT_f+K_d)}{T_fT_vT_hT_s} \tag{5.18d}$$

$$n_1=\frac{2K_{ip}K_vK_hK_s((-K_pT_f-K_d)+(K_p-K_iT_f)L/2)}{T_fT_vT_hT_sL} \tag{5.18e}$$

$$n_2=\frac{2K_iK_{ip}K_vK_hK_s(K_iT_f-K_p+(-K_iL/2))}{T_fT_vT_hT_sL} \tag{5.18f}$$

$$n_3=\frac{2K_iK_{ip}K_vK_hK_s}{T_fT_vT_hT_sL} \tag{5.18g}$$

$$d_1=\frac{2T_fT_vT_hT_s+(T_vT_hT_s+T_vT_hT_f+T_vT_sT_f+T_hT_sT_f)L}{T_fT_vT_hT_sL} \tag{5.18h}$$

$$d_2=\frac{2(T_vT_hT_s+T_vT_hT_f+T_vT_sT_f+T_hT_sT_f)+(T_vT_h+T_vT_s+T_hT_s+T_vT_f+T_hT_f+T_sT_f)L}{T_fT_vT_hT_sL} \tag{5.18i}$$

$$\begin{aligned} d_3=&\frac{2(T_vT_h+T_vT_s+T_hT_s+T_vT_f+T_hT_f+T_sT_f)}{T_fT_vT_hT_sL}+ \\ &\frac{[(T_v+T_h+T_s+T_f)+(K_{ip}K_vK_hK_s)(k_1+k_2)(-K_pT_f-K_d)]}{T_fT_vT_hT_s} \end{aligned} \tag{5.18j}$$

$$\begin{aligned} d_4=&\frac{2(T_v+T_h+T_f+T_s+L/2)}{T_fT_vT_hT_sL}+ \\ &\frac{2[(K_{ip}K_vK_hK_s)(k_1+k_2)(K_pT_f+K_d-K_pL/2)]}{T_fT_vT_hT_sL} \end{aligned} \tag{5.18k}$$

$$d_5 = \frac{2[(K_{ip}K_vK_hK_s)(k_1+k_2)K_p+1]}{T_fT_vT_hT_sL} \tag{5.181}$$

If the block diagram of Figure 5.12 is devided into the linear and nonlinear blocks using Equation (5.18), It is shown as Figure 5.13

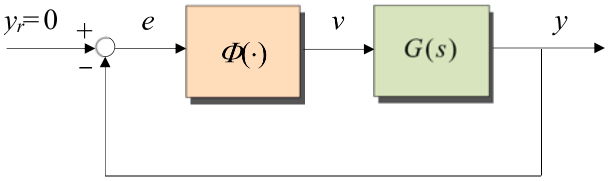

Figure 5.13 Control system when $y_r = 0$ and $\theta_d = 0$

5.3.2 P-NPID control system

The block diagram of the overall control system that combines the P-NPID controller and the controlled system is shown in Figure 5.14.

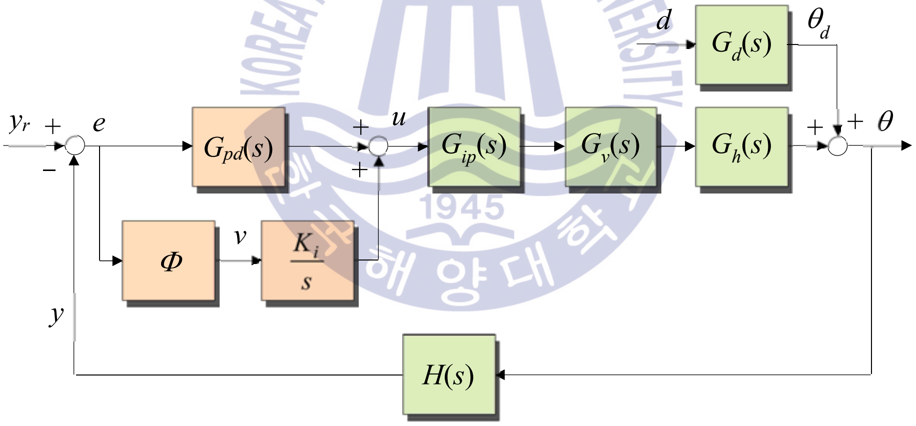

Figure 5.14 Overall P-NPID control system

As mentioned previously, if the main engine is operated at a constant speed ($y_r = 0$) and the effect of disturbance is not significant ($\theta_d = 0$), the block diagram in Figure 5.14 can be simplified as follows.

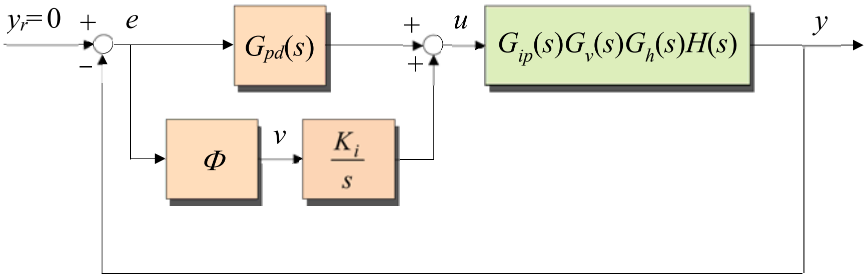

Figure 5.15 Overall P-NPID control system when y_r= 0 and θ_d= 0

Based on this, the input/output relationship of the linear block from v to y can be expressed as a transfer function, which can be written as

$$Y(s) = G_{ip}(s)G_v(s)G_h(s)H(s)[\frac{K_i}{s}V(s) - G_{pd}(s)Y(s)] \tag{5.19}$$

If substituting and summarizing each transfer function, $G(s)= Y(s)/V(s)$ is expressed as the following equation.

$$G(s) = \frac{K_i G_{ip}(s)G_v(s)G_h(s)H(s)}{s[1 + G_{pd}(s)G_{ip}(s)G_v(s)G_h(s)H(s)]} = \frac{P(s)}{Q(s)} \tag{5.20a}$$

$$P(s) = K_i G_{ip}(s)G_v(s)G_h(s)H(s) = p_0 s^2 + p_1 s + p_2 \tag{5.20b}$$

$$\begin{aligned} Q(s) &= s[1 + G_{pd}(s)G_{ip}(s)G_v(s)G_h(s)H(s)] \\ &= s(s^5 + q_1 s^4 + q_2 s^3 + q_3 s^2 + q_4 s + q_5) \end{aligned} \tag{5.20c}$$

where the parameters of the polynomial are obtained as follows.

$$p_0 = \frac{K_i K_{ip} K_v K_h K_s (-T_f L)}{T_f T_v T_h T_s L} \tag{5.20d}$$

$$p_1 = \frac{2[K_i K_{ip} K_v K_h K_s (T_f - L/2)]}{T_f T_v T_h T_s L} \tag{5.20e}$$

$$p_2 = \frac{2K_iK_{ip}K_vK_hK_s}{T_fT_vT_hT_sL} \tag{5.20f}$$

$$q_1 = \frac{2T_fT_vT_hT_s + (T_fT_vT_h + T_fT_vT_s + T_fT_hT_s + T_vT_hT_s)L}{T_fT_vT_hT_sL} \tag{5.20g}$$

$$q_2 = \frac{2[T_fT_vT_h + T_fT_vT_s + T_fT_hT_s + T_vT_hT_s] + (T_fT_v + T_fT_h + T_vT_h + T_fT_s + T_vT_s + T_hT_s)L}{T_fT_vT_hT_sL} \tag{5.20h}$$

$$q_3 = \frac{2(T_fT_v + T_fT_h + T_vT_h + T_fT_s + T_vT_s + T_hT_s)}{T_fT_vT_hT_sL} +$$

$$\frac{(T_f + T_v + T_h + T_s) + (K_{ip}K_vK_hK_s)(-K_pT_f - K_d)}{T_fT_vT_hT_s} \tag{5.20i}$$

$$q_4 = \frac{2[T_fT_vT_hT_s + L/2 + K_{ip}K_vK_hK_s(K_pT_f + K_d - K_pL/2)]}{T_fT_vT_hT_sL} \tag{5.20j}$$

$$q_5 = \frac{2[K_pK_{ip}K_vK_hK_s + 1]}{T_fT_vT_hT_sL} \tag{5.20k}$$

5.4 Tuning of the controller parameters

This section covers the problem of optimal tuning the parameters that the two proposed NPID controllers achieve satisfactory performance. Since the genetic algorithm is used for optimal tuning of the parameters, the genetic algorithm will be briefly discussed first.

5.4.1 Genetic algorithm

All living things in nature produce their offspring and live in harmony with their surroundings to preserve their genes and survive. A genetic algorithm is an optimization technique that imitates genetics and principles of natural selection with computer algorithms based on the fact that these series of processes are the best in a given environment [57-67].

When this process is used to solve the problem, the basic premise is to form an initial population to artificially cause evolution. A population is formed by a number of individuals, which are expressed in the form of strings of binary numbers or real numbers to reflect the role of genes. This population is progressively improved by genetic operators that mimic the sexual reproduction and evolutionary principles. Each individual, which is a member of a population, can be quantified by a fitness function and individual with large fitness values are more likely to be selected. The genetic information is exchanged among selected individuals and random genetic modification is introduced to form the next generation population.

(1) Structure of a genetic algorithm

The search process of the genetic algorithm is divided into five stages: population initialization, fitness evaluation, reproduction, crossover, and mutation. Figure 5.16 shows the basic structure of a genetic algorithm.

In the initialization stage, an initial population is formed that consists of individuals likely to be a solution to a given matter. In the fitness evaluation stage, the fitness of the individuals is evaluated, which is calculated from the objective function. The individuals in the current population are selected for reproduction depending on the relative fitness values of the individuals. Generally, the concept of survival of the fittest is applied to the case where individuals with high-performance are more likely to be selected, and those with poor performance disappear from the population. Selected individuals exchange and combine their genetic information with each other through crossover to generate offspring. Finally, they provide a means of introducing new information into the population by arbitrarily changing the genetic information of the selected individual through mutation. In this way, the newly formed population repeats the fitness evaluation, reproduction, crossover, and mutation operations previously performed until the optimal solution is found.

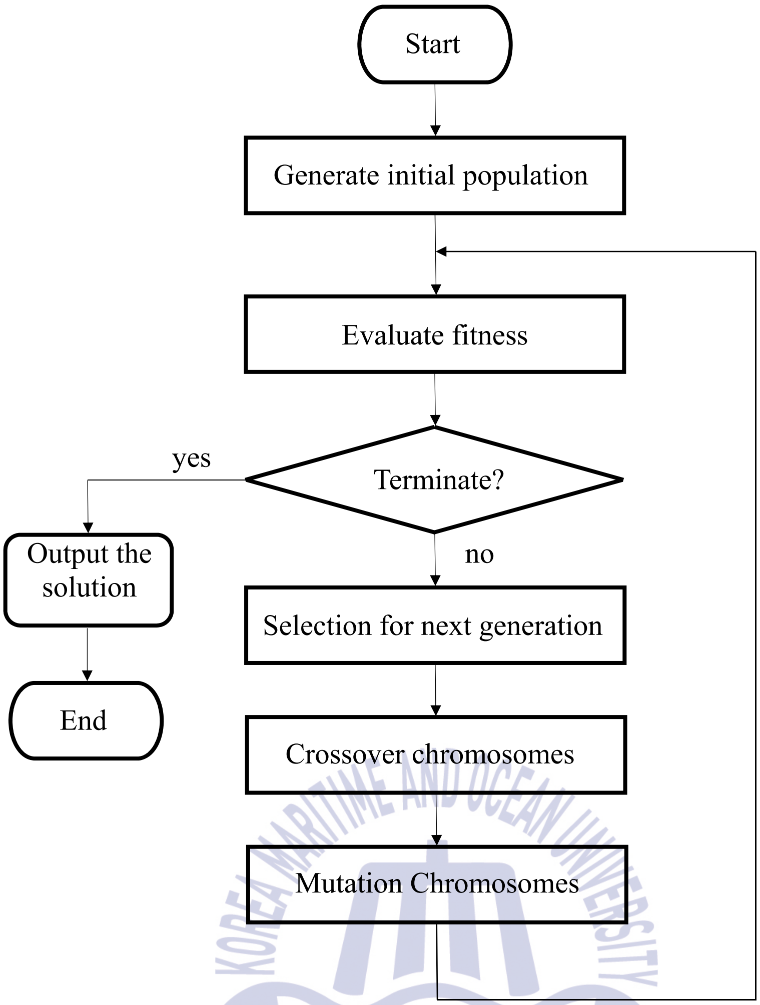

Figure 5.16 Structure of a genetic algorithm

(2) Basic genetic operator

Above all, it can be said that the core of the genetic algorithm is the basic genetic operator, which imitates the evolutionary principle of nature in the form of an algorithm. For this, the genetic algorithm uses the reproduction, crossover, and mutation operators as basic operators. Since the solution vector of the matter is expressed as real coding in this thesis, a real-coded genetic algorithm (RCGA) is used that employs operators which can handle it.

① Reproduction

Reproduction refers to the process of artificially mimicking the phenomenon of survival of the fittest in the natural system and selecting individuals according to the fitness of each individual to form a new population. Through reproduction, weak individuals are culled from the population, strong ones are selected, and good genes are spread to later generations, making the whole population stronger. In this thesis, reproduction which is similar to gradient [57] is used.

② Crossover

Crossover is to artificially imitate sexual mating of parental generations of natural system creatures, which selects a pair of parent chromosomes arbitrarily from the mating pool to search for a new point through information exchange among individual, and exchanges and joins the chromosomes to generate offspring after the crossover point.

In this thesis, the arithmetical crossover is used [58]. If two chromosomes $\boldsymbol{x}_1= [x_{11}, x_{12},\cdots, x_{1n}]$, $\boldsymbol{x}_2= [x_{21}, x_{22},\cdots, x_{2n}]$ are selected, their corresponding elements are first combined to produce the offspring $\bar{\boldsymbol{x}}_1$, $\bar{\boldsymbol{x}}_2$, as in Equation (5.21).

$$\begin{aligned} \bar{x}_{1j} &= \lambda x_{2j} + (1-\lambda)x_{1j} \\ \bar{x}_{2j} &= \lambda x_{1j} + (1-\lambda)x_{2j} (1 \le j \le n) \end{aligned} \tag{5.21}$$

where λ is a random value between [0, 1].

③ Mutation

While simulated evolution continues, the population becomes closer to the solution through the reproduction and crossover operators, and the chromosomes resemble each other. This phenomenon is desirable at the end of the generation, but if it occurs at the beginning of the generation, it may fall into the local solution or the dead corner due to lack of diversity of genes. Mutation is used to escape from this unwanted solution. This thesis uses an operator called dynamic mutation [59], also known as non-uniform mutation. Dynamic mutation can be used to select a large mutation rate because it searches the entire search space at the beginning of the generation with an equal rate, and when the number of generations increases, it narrows the search space and searches locally. If mutation occurs in the *j*th gene $\bar{x}_j$, the gene is changed from Equation (5.21) as follows:

$$x_j = \begin{cases} \bar{x}_j + \mathrm{V}(g, x_j^{(U)} - \bar{x}_j), & \tau = 0 \\ \bar{x}_j - \mathrm{V}(g, \bar{x}_j - x_j^{(L)}), & \tau = 1 \end{cases} \tag{5.22a}$$

$$\mathrm{V}(g, y) = y \cdot r \cdot (1 - \frac{g}{g_{\max}})^b \tag{5.22b}$$

where $x_j^{(L)}$ and $x_j^{(U)}$ are lower limit value and the upper limit value of x_j, respectively. g and g_{max} refers to the number of generations and the maximum number of generations where algorithm runs, respectively. τ is a random value taking either 0 or 1, and r is a random value between 0 and 1. b is a parameter indicating the degree of non-uniform.

(3) Fitness evaluation

In nature system, creatures constantly adapt to environments such as diseases, disasters, and natural enemies, and one creature’s ability to adapt reflects its fitness to the environment. In genetic algorithm, it is reflected in the process of evaluating the fitness of the individual.

All individuals in the population are evaluated for fitness for each generation. The fitness is calculated by the objective function selected to solve the given matter. In this process, the fitness function should be expressed in the form of a maximization matter and should not have a negative value in order to ensure that individuals with greater fitness will receive more compensation. Therefore, this thesis uses the equation such as Equation (5.23) to obtain the fitness function from the objective function described as the minimization matter.

$$f = -J(x) - J_{\min} \tag{5.23}$$

where f and $J(x)$ are the fitness function and the objective function, respectively, and x is the parameter vector. J_{min} is a constant that guarantees $f \geq 0$ [60-61].

(4) Other strategies

If a super individual emerges in the population of initial generations, the existing reproduction operator clones this individual multiple times, and as a result, they dominate the population, quickly converging to the local optimal point. In later generations, on the contrary, the population becomes stronger, and when individuals are clustered around a point, it becomes difficult to distinguish a good individual from a better individual. Therefore, it is necessary to reduce the influence of relative fitness among individuals so that the diversity of the genes can be sustained at an early stage, and to increase their influence later.

Therefore, this thesis uses linear scaling that distributes the fitness values of the individuals to a wide range of values so as to reduce the fitness influence of good individuals in initial generations and distributes more individuals so that more can be selected in later generations [62]. Also, an Elitist strategy [63] is used to ensure that the optimal individual is delivered to the next generation without extinction.

5.4.2 Optimal tuning of the controller parameters

The LNG regasification system for the main engine of the ship is mainly operated in two modes: warm-up mode and automatic mode. In the warm-up mode, the engine is prepared as ready to start several hours before departure. For this, the set-point is sequentially changed so that the glycol temperature of the secondary loop reaches the desired temperature. When the desired temperature is reached, LNG in the liquid state flows to the primary loop and is converted into a gas state that can be injected into the engine injector. At this time, the controller should have a good set-point tracking performance.

In the automatic mode, on the other hand, the start and stop of the engine, forward-reverse operation and normal operation are performed. In this mode, the set-point is fixed and the controller must be able to return quickly whenever there is an engine speed change command or the output is out of set-point by disturbance, that is, disturbance rejection performance should be good.

As discussed previously, the two proposed NPID controllers have 6 parameters K_p,

K_i, K_d, σ, k_1, k_2 in total. But k_1 and k_2 are directly multiplied by K_p, K_i, K_d and a GA is tuned in terms of optimizing their multiplication. Thus, k_1 and k_2 can be normalized to values between 0 and 1. In particular, a number of the user-defined gains of the F-NPID controller set to k_2= 1 are five: K_p, K_i, K_d, σ, k_1. In the case of a P-NPID controller, if k_1= 0 and k_2= 1, a number of the user-defined gains are four: K_p, K_i, K_d, σ. It makes the structure of P-NPID controller much simpler.

Therefore, the parameters of the NPID controllers are tuned by the GA [64] such that the following *IAE* objective function is minimized.

$$J = \int_0^{t_f} |e(t)|dt \tag{5.24}$$

where t_f is a sufficiently large enough time to allow subsequent integral value to be ignored.

Chapter 6. Stability Analysis

In the previous chapter, two NPID controllers that introduce nonlinear functions into conventional PID controller, use nonlinearly scaled error signals and input into the proportional, derivative, and integral actions were proposed. It is necessary to examine the stability of the overall feedback system that can be caused by introducing nonlinear functions during controller design. For this, the stability of the overall feedback system is analyzed by applying the circle stability theorems [68], which is often used for stability analysis of nonlinear problems.

6.1 System description

Let us consider a system as shown in Figure 6.1 before analyzing the stability of the proposed feedback system.

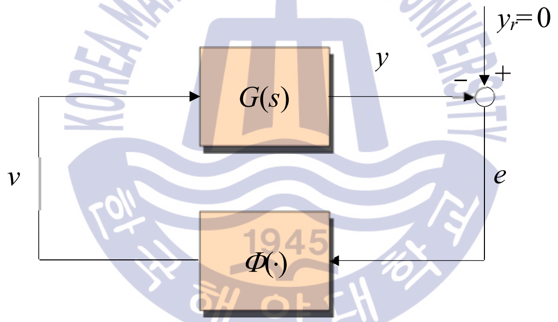

Figure 6.1 A feedback system

where $G(s)$ and $\Phi(\cdot)$ represent the linear and nonlinear part of the feedback system, respectively. In particular, $G(s)$, described by Equation (5.18) or Equation (5.20), is linear time-invariant minimal and can be expressed in the following state space form.

$$\dot{x} = Ax + Bv \tag{6.1a}$$

$$y = Cx + dv \tag{6.1b}$$

$$v = \Phi(e) \tag{6.1c}$$

where $x \in R^n$ is a state, v the input, y the output, $A \in R^{n \times n}$, $B \in R^{n \times 1}$, $C \in R^{1 \times n}$. (A, B) is controllable, (A, C) is observable, and Φ: $R \rightarrow R$ is a memoryless nonlinearity. Assuming that the external input $y_r = 0$ as the unforced system because in most cases the controller regulates to reject disturbances, then $y = -e$.

The transfer function of Equation (5.18) or Equation (5.20) can also be expressed as Equation (6.2) from Equation (6.1):

$$G(s) = C(sI - A)^{-1} B + d \tag{6.2}$$

Meanwhile, the nonlinear function Φ is a memoryless function satisfying the sector conditions. The problem is to find the bounds, that is, constant gains such that the overall feedback system is stable.

6.2 Basic definitions and theorems

Before explaining the stability of the proposed feedback systems, some definitions and theorems fundamental to the circle stability theorems are examined at first [68].

Definition 6.1 (Passivity) Consider a scalar time-invariant function in Figure 6.2(a). The function $\Phi: R \rightarrow R$ is called passive if $ev = e\Phi(e)$ is always nonnegative, that is, $ev = e\Phi(e) \geq 0$ for all e.

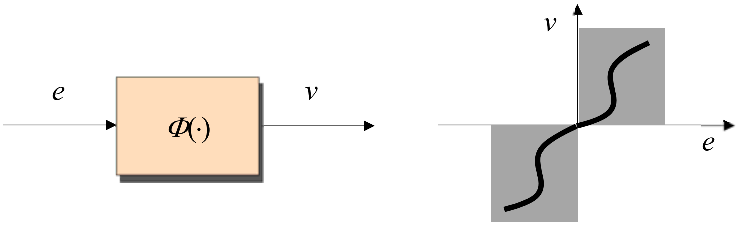

(a) A passive function (b) *e*-*v* relation

Figure 6.2 A passive function and *e*-*v* relation

The graph of the input-output relation must lie in the first and third quadrants as shown in Figure 6.2(b). It is also said that the graph belong to the sector [0, ∞), where zero and infinity are the slopes of the boundaries of the first-third quadrant region.

Definition 6.2 (Sector) A memoryless function Φ: $R \rightarrow R$ or $\Phi(e)$ is said to belong to the sectors

- $[0, \infty)$, if $\Phi(e)/e \geq 0$ (6.3a)
- $[k_1, \infty)$, if $\Phi(e)/e \geq k_1$ (6.3b)
- $[0, k_2]$, if $0 \leq \Phi(e)/e \leq k_2$ (6.3c)
- $[k_1, k_2]$, if $k_1 \leq \Phi(e)/e \leq k_2$ (6.3d)

for $\forall e \in [e_1, e_2]$, and nonnegative constant gains k_1, k_2 ($0 \leq k_1 \leq k_2$). If it holds $\forall e \in R$, the sector condition holds globally.

The sector [0, ∞) corresponds to passivity. The others are the sectors with excess of passivity. In all cases, the following two properties hold:

- $\Phi(0) = 0$ and (6.4a)
- $e\Phi(e) \geq 0$, $\forall e$ (6.4b)

The second property can be easily verified that as in the case of Equation (6.3d)

$$0 \le k_1 e^2 \le e\Phi(e) \le k_2 e^2 \qquad (6.5)$$

for all e, as long as k_1 and k_2 are nonnegative numbers with $k_1 \le k_2$. Geometrically, sector condition $[k_1, \infty)$ implies that Φ always lies between the straight line $k_1 e$ and the Φ-axis, and $[k_1, k_2]$ that Φ always lies between the two straight lines $k_1 e$ and $k_2 e$. The above sector conditions in Equation (6.3) are simply represented by $\Phi \in [0, \infty)$ or $\Phi \in [k_1, \infty)$ or $\Phi \in [0, k_2]$ or $\Phi \in [k_1, k_2]$. Figure 6.3 shows the sector conditions for four cases.

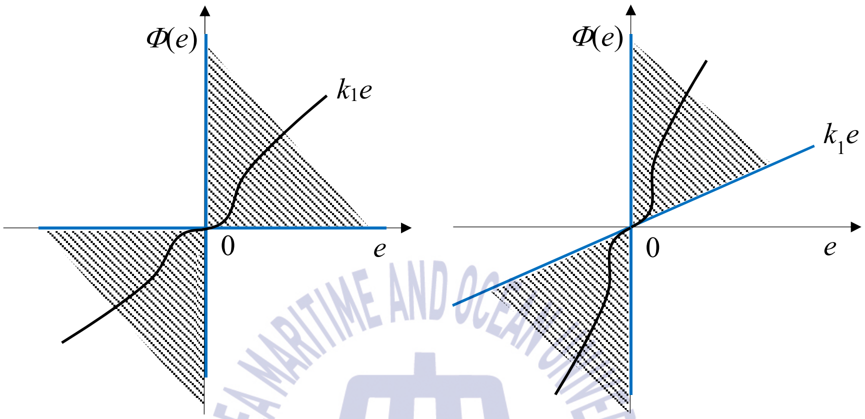

(a) Sector $[0, \infty)$ (b) Sector $[k_1, \infty)$

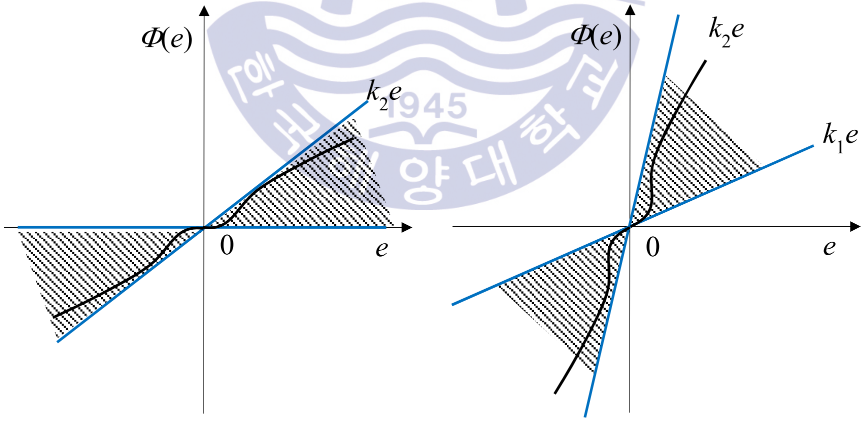

(c) Sector $[0, k_2]$ (d) Sector $[k_1, k_2]$

Figure 6.3 Geometrical representation of the sectors

Definition 6.3 (Positive real and strictly positive real) Consider a proper rational transfer function $G(s)$ described in Equation (6.2). Then $G(s)$ is called positive real if and only if the following conditions are satisfied:

- all poles of $G(s)$ are in $\mathrm{Re}(s) \leq 0$ (no poles in the right-hand plane),
- any pole of $G(s)$ on the imaginary axis is a simple pole with positive residues,
- $\mathrm{Re}(G(j\omega)) \geq 0$, for $\forall \omega \in R$.

The transfer function $G(s)$ is called strictly positive real if and only if the following conditions are satisfied:

- all poles of $G(s)$ are in $\mathrm{Re}(s) < 0$ (all poles in the left-hand plane),
- $\mathrm{Re}(G(j\omega)) > 0$, for $\forall \omega \in R$.

The basic difference between positive real and strictly positive real functions is that positive real functions can have poles on the $j\omega$ axis, while strictly positive real functions cannot. The condition for the transfer function of the system given by Equation (6.2) to become a positive real is defined in the following Lemma 6.1 known as Kalman-Yakubovich or Kalman-Yakubovich-Popov Lemma. Detailed proof is omitted, and referred to [68].

Lemma 6.1 (Positive Real) Let $G(s) = C(sI - A)^{-1}B + d$ be a transfer function where (A, B) is controllable and (A, C) is observable. Then, $G(s)$ is positive real if and only if there exist matrices $P = P^T > 0$, L, and w such that

$$PA + A^T P = -L^T L \tag{6.6}$$

$$PB = C^T - L^T w \tag{6.7}$$

$$w^2 = 2d \tag{6.8}$$

and is strictly positive real if and only if there exist matrices $P = P^T > 0$, L, w, and a positive constant ε such that

$$PA + A^T P = -L^T L - \varepsilon P \tag{6.9}$$

$$PB = C^T - L^T w \tag{6.10}$$

$$w^2 = 2d \tag{6.11}$$

which are known as the Kalman-Yakubovich-Popov lemma.

If the linear transfer function $G(s)$ is strictly positive real and the nonlinear function is passive, i.e. $\Phi \in [0, \infty)$ in the system given in Figure 6.1, Lemma 6.1, known as the Kalman-Yakubovich-Popov lemma can be applied to prove that it is absolutely stable [68].

Theorem 6.1 (Absolute Stability) Consider the feedback system of Figure 6.1. The system in Equation (6.1) is absolutely stable if Φ satisfies the sector condition $[0, \infty)$ and $G(s)$ is strictly positive real.

Proof: Using $V(x) = \frac{1}{2}x^T Px$ as a Lyapunov function candidate, where $P = P^T > 0$ satisfies the Kalman-Yakubovich-Popov Equations (6.9)-(6.11) and $\varepsilon > 0$, it is obtained

$$\begin{aligned}\dot{V} &= \frac{1}{2}x^T P\dot{x} + \frac{1}{2}\dot{x}^T Px = \frac{1}{2}x^T(PA + A^T P) + \frac{1}{2}x^T PBv + \frac{1}{2}(x^T PBv)^T \\ &= \frac{1}{2}x^T(PA + A^T P) + x^T PBv\end{aligned}$$

Using Equation (6.9) and Equation (6.10) yields

$$\begin{aligned}\dot{V} &= -\frac{1}{2}x^T(L^T L + \varepsilon P)x + x^T(C^T - L^T w)v \\ &= -\frac{1}{2}\varepsilon x^T Px - \frac{1}{2}x^T L^T Lx + (Cx + dv)^T v - v^T dv - x^T L^T wv\end{aligned}$$

Using Equation (6.11) and the fact that

$$(Cx + dv)^T v = yv = -e\Phi(e)$$

$$v^T dv = dv^2 = \frac{1}{2} w^2 v^2$$

yields

$$\dot{V} = -\frac{1}{2}\varepsilon x^T P x - \frac{1}{2}(Lx + wv)^T (Lx + wv) - e\Phi(e)\,.$$

Since the first two terms are of quadratic forms and $e\Phi(e) \geq 0$ for $\forall e$ from Equation (6.4b), $\dot{V} \leq 0$. Hence, the system is absolutely stable.

Through the above theorem 6.1, the necessary conditions to be stable for a feedback connection of two passive systems which are $\Phi \in [0, \infty)$ and strictly positive real $G(s)$ was observed. However, when the sector condition of Φ is different, theorem 6.1 cannot be directly applied. Instead, the theorem 6.1 should be applied after the sector condition of Φ should be converted to $[0, \infty)$.

A function in the sector $[k_1, k_2]$ for $\forall e$ can be transformed into a function in the sector $[0, \infty)$ by input feedforward followed by output feedback, that is, the loop transformation as depicted in Figure 6.4. Loop transformation does not change the interconnection and stability of the original system but does changes each of the subsystems. Input feedforward of k_1 on Φ can be nullified by output feedback of k_1 on $G(s)$, resulting in an equivalent feedback connection as far as asymptotic stability of the origin is kept as shown in Figure 6.4(b). Similarly, post-multiplying Φ by $1/(k_2-k_1)$ can be nullified by pre-multiplying $G(s)$ by (k_2-k_1) as shown in Figure 6.4(c). Finally, output feedback on the component in the feedback path can be nullified by input feedforward on the component in the forward path.

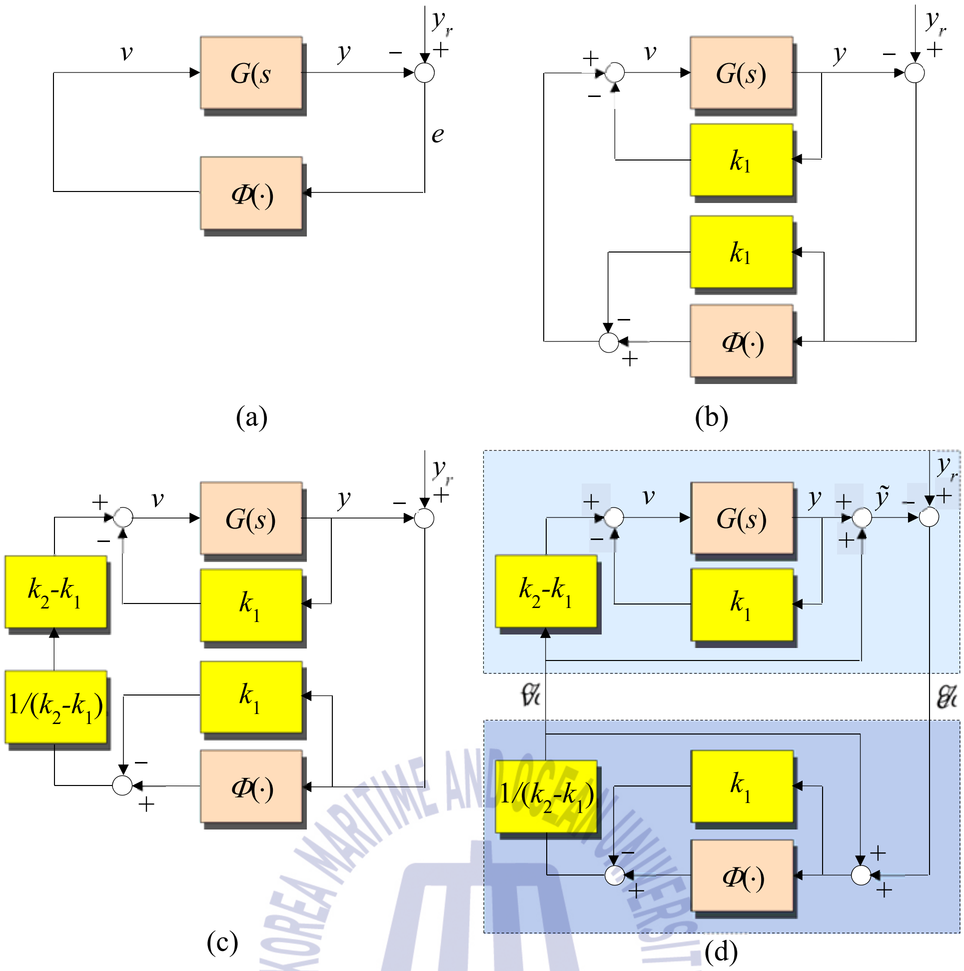

(a) (b)

(c) (d)

Figure 6.4 Loop transformation for changes of sector condition

In the subsystem finally obtained as Figure 6.4(d), the relation $\Phi(e) = k(e)e$ is applied and express it as the following equation:

$$\tilde{v} = \frac{1}{k_2 - k_1}[k(\cdot) - k_1](\tilde{e} + \tilde{v}) \tag{6.12}$$

The following equation is obtained by summarizing Equation (6.12).

$$\tilde{v} = \frac{k(\cdot) - k_1}{k_2 - k(\cdot)}\tilde{e} = \tilde{k}(\cdot)\tilde{e} = \tilde{\Phi}(\cdot) \tag{6.13a}$$

$$\tilde{k}(\cdot) = \frac{k(\cdot) - k_1}{k_2 - k(\cdot)} \tag{6.13b}$$

Therefore, applying the mapping of Equation (6.13b) converts the nonlinear function $\Phi \in [k_1, k_2]$ to a nonlinear function of the sector condition $\tilde{\Phi} \in [0, \infty)$. That is, it can be seen that if $k(\cdot) = k_1$, $\tilde{k}(\cdot) = 0$ and if $k(\cdot) = k_2$, $\tilde{k}(\cdot) \to \infty$. Performing a loop transformation to change the sector condition will also change the original linear system, like the upper subsystem in Figure 6.4(d). In the figure, the following expression is satisfied.

$$\tilde{Y}(s) = \tilde{U}(s) + \frac{G(s)}{1 + k_1 G(s)}(k_2 - k_1)\tilde{U}(s) \tag{6.14}$$

The following equation is obtained by summarizing Equation (6.14).

$$\tilde{Y}(s) = \frac{1 + k_2 G(s)}{1 + k_1 G(s)}\tilde{U}(s) \tag{6.15}$$

If Equation (6.15) is written again, the transfer function is obtained as following Equation (6.16).

$$\tilde{G}(s) = \frac{\tilde{Y}(s)}{\tilde{U}(s)} = \frac{1 + k_2 G(s)}{1 + k_1 G(s)} \tag{6.16}$$

Therefore, when the sector condition of the nonlinear function is $\Phi \in [k_1, k_2]$, the stability of the system can be said to be attributed to the problem of determining whether the transfer function of Equation (6.16) is strictly positive real or not.

Theorem 6.2 (Absolute Stability) Consider the feedback system of Figure 6.1 where

$\Phi \in [k_1, k_2]$. Then, the system in Equation (6.2) is absolutely stable if

$$\mathcal{G}(s) = \frac{1 + k_2 G(s)}{1 + k_1 G(s)}$$

is strictly positive real.

Proof: The case $\Phi \in [k_1, k_2]$ can be transformed to a case where the nonlinearity belongs to $\Phi \in [0, \infty)$ via the loop transformation as shown in Figure 6.4. The loop transformation does not change the interconnection but changes the transfer function $G(s)$ to $\mathcal{G}(s)$ in Equation (6.16). Hence, the original system is absolutely stable if the changed subsystem $\mathcal{G}(s) = [1 + k_2 G(s)] / [1 + k_1 G(s)]$ is strictly positive real.

Now the stability of the overall system should check only if $\mathcal{G}(s)$ of Equation (6.16) is strictly positive real according to the condition of Definition 6.3. In general, the pole and zero of a polynomial expression $G(s)$ described in the form of Equation (5.18) or Equation (5.20) can be inferred from a given transfer function to some extent, but if converted like Equation (6.16), $\mathcal{G}(s)$ becomes more complicated, so the pole and zero cannot be known easily. One way to solve this problem is to apply the frequency concept. Through frequency concept, the following Lemma 6.2 explains that if $\mathcal{G}(j\omega)$ is Hurwitz and $\mathrm{Re}\,\mathcal{G}(j\omega) \geq 0$ and $\mathcal{G}(j\omega)$ is a strictly positive real, the system is absolutely stable.

Lemma 6.2 (Circle criterion) Consider the system in Figure 6.1 where $G(s)$ is stable and $\Phi \in [k_1, k_2]$. Then the system is absolutely stable if one of the following conditions is satisfied:

- If $0 < k_1 < k_2$, then the Nyquist plot of $G(j\omega)$ does not penetrate the disk $D(k_1, k_2)$ having as diameter the segment $[-1/k_1, -1/k_2]$ located on the x-axis.
- If $0 = k_1 < k_2$, then the Nyquist plot of $G(j\omega)$ is located on the right of a vertical line defined by $\mathrm{Re}(s) = -1/k_2$.

Proof: Suppose that $G(j\omega)= \alpha+j\beta$, then in the case of $0< k_1< k_2$, Equation (6.16) can be rewritten as:

$$\operatorname{Re}\mathcal{G}(j\omega) = \operatorname{Re}\left(\frac{1/k_2 + G(j\omega)}{1/k_1 + G(j\omega)}\right) = \frac{(1/k_2+\alpha)(1/k_1+\alpha)+\beta^2}{(1/k_1+\alpha)^2+\beta^2} > 0$$

Rearranging the above inequality with the fact that the denominator is never zero yields

$$[\alpha + 2(\frac{1}{k_1}+\frac{1}{k_2})]^2 + \beta^2 > [\frac{1}{2}(\frac{1}{k_1}-\frac{1}{k_2})]^2$$

This inequality implies that the Nyquist plot of $G(j\omega)$ locates the outside of the circle with the center of $-2(1/k_1+1/k_2)+j0$ and a radius $(1/k_1-1/k_2)/2$ and never enter the disk $D(k_1,k_2)$ as shown in Figure 6.5(a).

In the case of $0= k_1< k_2$, Equation (6.16) can be rewritten as:

$$\operatorname{Re}\mathcal{G}(j\omega) = \operatorname{Re}(1+k_2 G(j\omega)) = 1 + k_2\alpha > 0$$

Rearranging the above inequality yields

$$\alpha > -\frac{1}{k_2}$$

This inequality implies that the Nyquist plot of $G(j\omega)$ lies to the right of a vertical line defined by $\operatorname{Re}(s)= -1/k_2$ as shown in Figure 6.5(b).

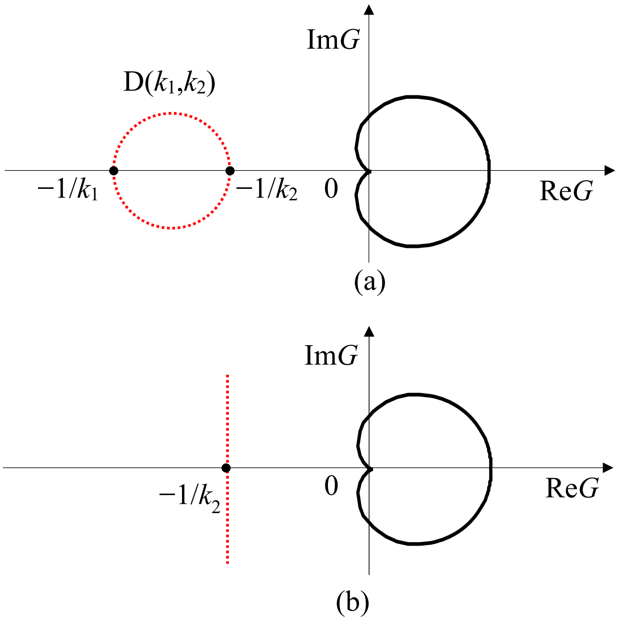

Figure 6.5 Disk D(k_1,k_2) and Nyquist plot of $G(j\omega)$

6.3 Stability of the NPID control systems

In order to guarantee stability by applying circle criterion to two proposed NPID control systems, the block diagram of feedback system in Figure 5.14 discussed in Section 5 is transformed as Figure 6.1, and then applies it to Lemma 6.2.

6.3.1 Sector condition of nonlinear block

In chapter 5, a linear block $G(s)$ and a nonlinear block Φ were examined that when the main engine is operating at a constant speed and the effect of disturbance is not significant, the controller is considered to be a feedback regulator, and can be briefly displayed as shown in Figure 6.1. At this time, it can be seen that the linear block is expressed as Equation (5.18) or Equation (5.20), and the sector condition of the memoryless nonlinearity Φ of the nonlinear block is determined by the use-defined gains k_1 and k_2 used for the posterior equation of Equation (5.3) and Equation (5.11). The following theorem shows that if k_1 and k_2 are positive constants and $k_1 \leq k_2$, $\Phi \in [k_1, k_2]$.

Theorem 6.3 Consider the mapping Φ of the T-S fuzzy system in Equation (5.12). Φ belongs to the sector $[k_1, k_2]$.

Proof: From the result of the fuzzy inference in Equation (6.12), $\alpha_i \geq 0$ (i= 1, 2, 3) and the fact that $\alpha_1+\alpha_2+\alpha_3 \neq 0$, clearly it is obtained

$$\Phi(e)=\frac{\alpha_1 k_1+\alpha_2 k_2+\alpha_3 k_1}{\alpha_1+\alpha_2+\alpha_3}e \geq \frac{\alpha_1 k_1+\alpha_2 k_1+\alpha_3 k_1}{\alpha_1+\alpha_2+\alpha_3}e = k_1 e$$

and also

$$\Phi(e)=\frac{\alpha_1 k_1+\alpha_2 k_2+\alpha_3 k_1}{\alpha_1+\alpha_2+\alpha_3}e \leq \frac{\alpha_1 k_2+\alpha_2 k_2+\alpha_3 k_2}{\alpha_1+\alpha_2+\alpha_3}e = k_2 e$$

Since it is expressed as $k_1 \leq \Phi(e)/e \leq k_2$, hence Φ belongs to the sector $[k_1, k_2]$. If k_1= 0 and k_2= 1 as a typical case, then Φ belongs to the sector [0, 1].

6.3.2 Stability analysis of F-NPID control system

To demonstrate that the feedback system in Figure 6.1 is absolutely stable, applying the parameters of the plant and the tuned controller with the choice of k_2= 1 in Table 7.1 and Table 7.2 to Equation (5.18) gives

$$N(s)=3.7805s^3-4.4756s^2-0.7595s+0.0081 \tag{6.17a}$$

$$D(s)=s(s^5+68.5405s^4+120.8028s^3+37.7492s^2+12.6517s+1.5005) \tag{6.17b}$$

It can be easily verified that the linear part $G(s)$ has six stable poles at 0, −66.7388, −1.5046, −0.1592 and −0.690±0.2986i.

Since $G(s)$ is stable and Φ belongs to the sector [0.860, 1], the first case of the Lemma 6.2 can be applied. Clearly, the choice of k_2 is not unique. The Nyquist plot of $G(j\omega)$

shown in Figure 6.6 lies on the right of the vertical line Re(s)= −0.552. Therefore, $-1/k_2$= −0.552, that is, k_2= 1.812.

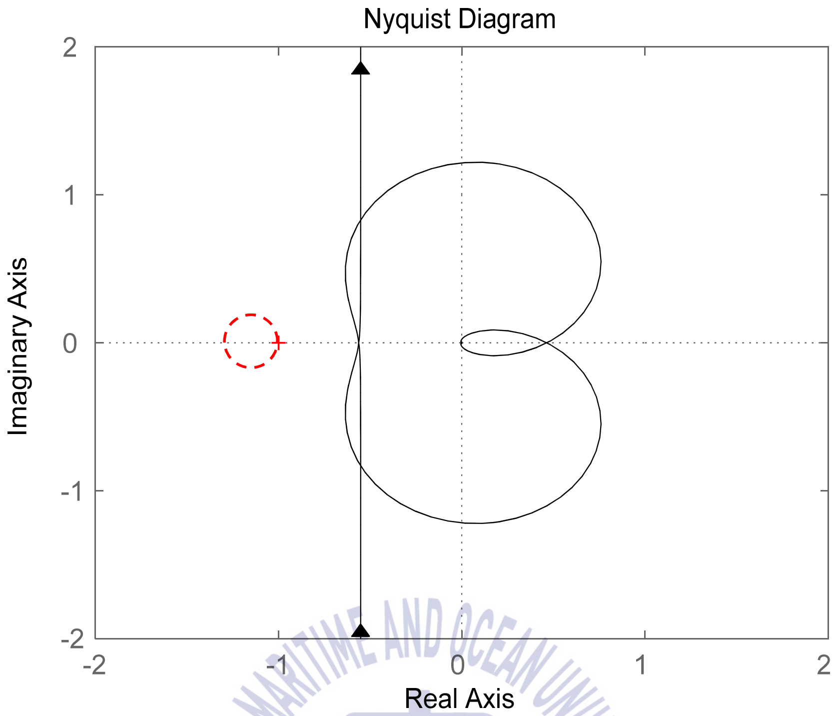

Figure 6.6 Nyquist plot of $G(j\omega)$ in F-NPID control system

This means that the system is absolutely stable for all values of k_2 less than 1.812. Hence, it can be concluded that the system is absolutely stable for all nonlinearities $\Phi \in [0.860, 1]$.

6.3.3 Stability analysis of P-NPID control system

In order to analyze stability by applying circle criterion to the proposed P-NPID control system, the system of Figure 5.14 is briefly divided into linear block $G(s)$ and nonlinear block Φ, and Lemma 6.2 is applied. Equations (6.18) are obtained by substituting and summarizing each transfer function covered in Chapters 4 and 5 in Equation (5.12). To demonstrate that the feedback system in Figure 6.7 is absolutely stable, applying the parameters of the plant and the tuned controller with the choice of

k_1= 0 and k_2= 1 in Table 7.1 and Table 7.2 to Equation (5.20) gives

$$P(s) = -0.0005s^2 - 0.0328s + 0.0447 \tag{6.18a}$$

$$Q(s) = s(s^5 + 68.23s^4 + 120.244s^3 + 40.6332s^2 + 8.9684s + 0.8874) \tag{6.18b}$$

It can be easily verified that the linear part $G(s)$ has six stable poles at 0, −66.429, −1.4376, −0.1707, and −0.0963±0.2125i and Φ belongs to the sector [0, 1]. The second case of the Lemma 6.2 can be applied.

Clearly, the choice of k_2 is not unique. The Nyquist plot of $G(j\omega)$ shown in Figure 6.7 lies on the right of the vertical line Re(s)= −0.541. Therefore, $-1/k_2$= −0.541, that is, k_2= 1.848. This means that the system is absolutely stable for all values of k_2 less than 1.848. Hence, it can be concluded that the system is absolutely stable for all nonlinearities $\Phi \in [0, 1]$.

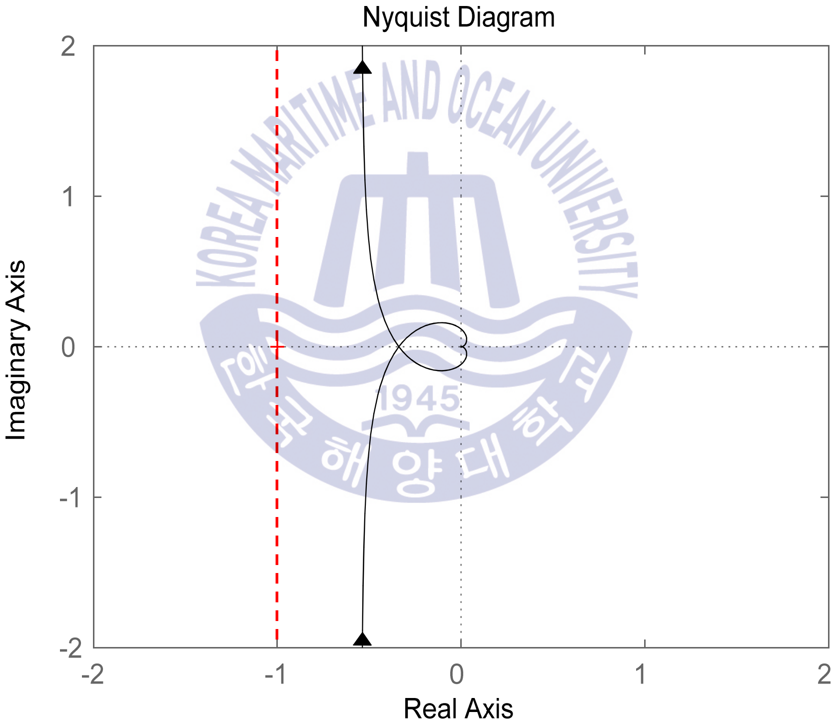

Figure 6.7 Nyquist plot of $G(j\omega)$ in P-NPID control system

Chapter 7. Simulations and Discussion of Results

7.1 Controller parameter tuning

A set of simulation works were performed to verify the effectiveness of the proposed methods. The results were compared with those of Seraji's NPID controller (Hereinafter simply referred to as S-NPID controller), those of the PID controller tuned by the Ziegler-Nichols (Z-N) method and the Tyreus-Luyben (T-L) method [55].

The proposed NPID controllers were tuned by the GA explained in Section 5.4 using parameters of the plant as shown in Table 7.1.

Table 7.1 Parameters of the plant

Parameter	Value
K_{ip}	0.75 [psi/mA]
K_v	0.4/3 [kcal/sec·psi]
T_v	3 [sec]
K_h	12.5 [°C·sec/kg]
T_h	30 [sec]
K_s	0.2 [mA/°C]
T_s	10 [sec]
K_d	1
L	1.5 [sec]

The methods to be compared have the structure of conventional PID controller, and the Z-N method and the T-L method are tuned by inducing periodic oscillation in the system. The calculated ultimate gain and ultimate period are $K_u = 83.7$ and $P_u = 37.9$, respectively. Meanwhile, the S-NPID controller is tuned by the GA under minimizing the *IAE* objective function such as Equation (5.24), where $k_0 = 0$, $k_1 = 1$, and $k_2 = 1$ are used as the nonlinear functions of Equation (4.14). All the parameters for the GA are arranged as follows:

Population size: $n = 50$,

Crossover probability: 0.9,

Basic mutation probability: 0.05.

The following Table 7.2 shows the tuned controller parameters.

Table 7.2 Tuned controller parameters

Method	Controller gains			Remarks
	K_p	K_i	K_d	
F-NPID	30.486	0.327	203.465	$\sigma= 0.332$, $k_1= 0.860$, $k_2= 1$
P-NPID	32.067	1.815	213.021	$\sigma= 0.160$, $k_1= 0$, $k_2= 1$
S-NPID	45.686	1.237	112.025	$k_0= 0$, $k_1= 1$, $k_2= 1$
Z-N	49.235	2.598	233.252	$K_u= 83.7$ $P_u= 37.9$
T-L	38.046	0.456	228.877	

7.2 Responses to set-point changes

The large main engine must be warmed up for several hours before start-up to ensure smooth start-up and longer engine life. During the warm-up period, a duty engineer takes several actions. In particular, the engine coolant, the lubricant, and the fuel oil are preheated to desired temperatures to maintain the engine in a startable state. In the case of LNG-fuelled marine engines, the LNG of −163 [℃] should be heated gradually to the normal temperature of 35~55 [℃] during the warm-up period, so the engineer increases the glycol outlet temperature set-point on the secondary loop by several steps with the time difference. On the contrary, if a vessel arrives at the port and the engine is completely stopped, the glycol outlet temperature should be slowly dropped from the operating temperature to the temperature of engine-room. At this time, the controller should be operated so that the output follows the set-point change well.

Figure 7.1 shows the response and control input when the glycol outlet temperature of the secondary heat exchanger is changed from 48 [℃] to the desired set point of 50 [℃] to check the set point tracking performance of the controllers. Figure 7.2 shows the response and control input when the glycol outlet temperature is changed from 50 [℃] to the desired set point of 48 [℃].

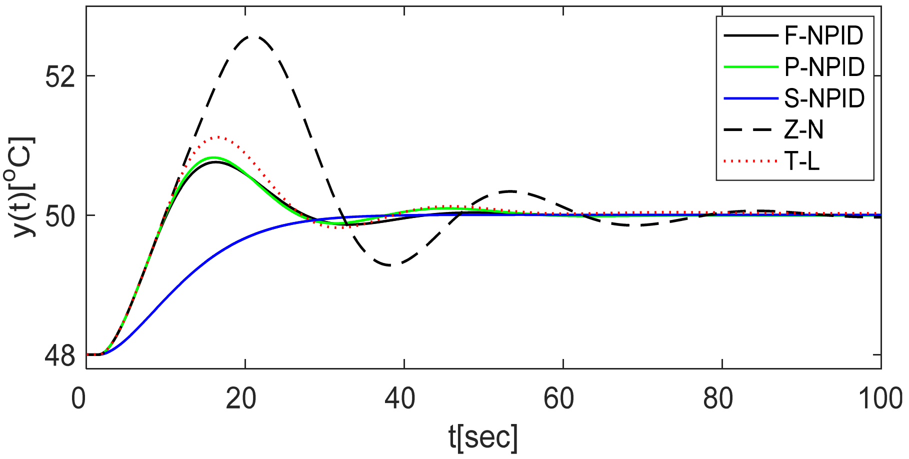

(a) Step responses

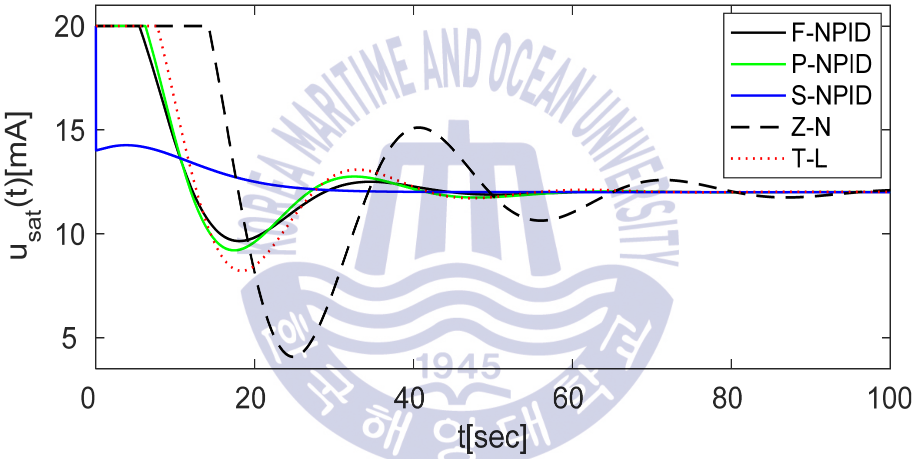

(b) Control inputs

Figure 7.1 Responses and control inputs of the five control methods when the set-point is step-wisely changed from 48 [℃] to 50 [℃]

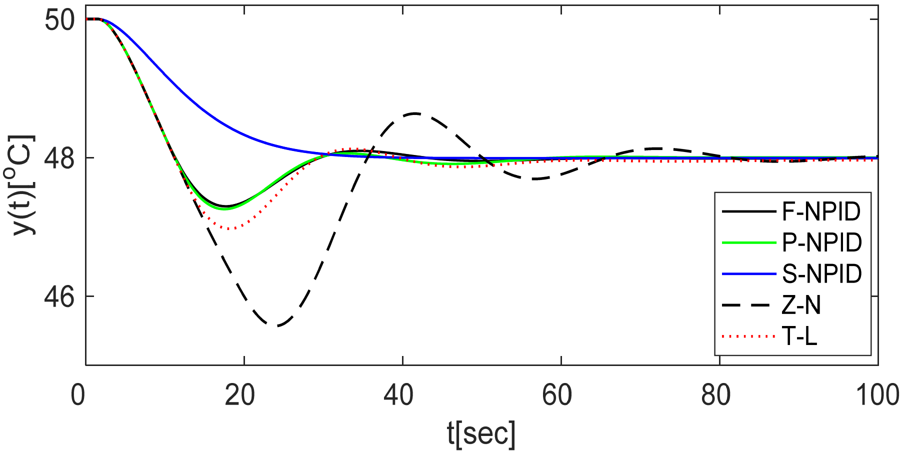

(a) Step responses

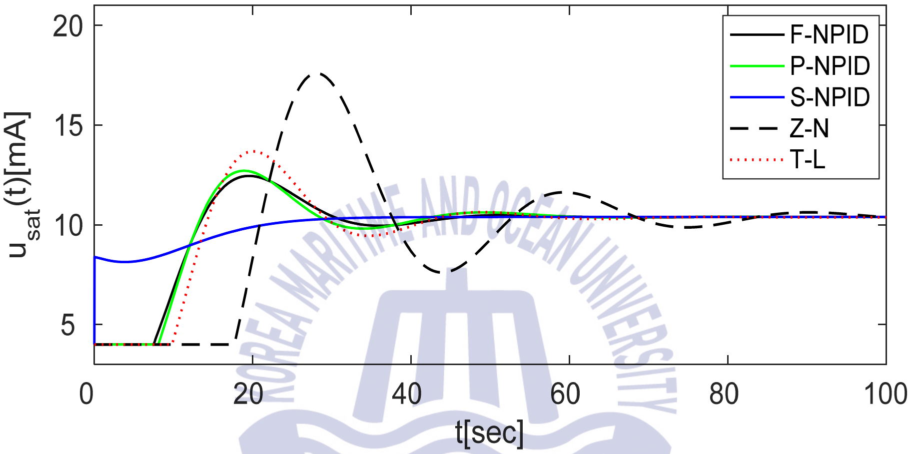

(b) Control inputs

Figure 7.2 Responses and control inputs of the five control methods when the set-point is step-wisely changed from 50 [℃] to 48 [℃]

These figures show that the response of the Z-N method is the worst, and the Seraji's NPID controller has a slower swiftness and a longer settling time.

For quantitative comparison, Table 7.3 summarizes rise time $t_r = t_{90} - t_{10}$, peak time t_p, overshoot M_p, 2 [%] settling time t_s, and IAE from the responses of Figure 7.1.

Table 7.3 Quantitative comparison of the set-point tracking performance

Method	Set-point tracking performance				
	t_r	t_p	M_p	t_s	IAE
F-NPID	5.898	16.300	38.056	40.127	22.539
P-NPID	5.829	16.020	41.507	53.395	23.265
S-NPID	18.324	54.500	0.0880	31.820	26.196
Z-N	5.737	20.980	131.67	90.482	59.275
T-L	5.865	16.520	53.887	52.768	27.113

Table 7.3 shows that the proposed methods are better both in terms of response swiftness and closeness. The outstanding point is that the P-NPID controller has fewer parameters to adjust than those of the F-NPID controller, but the performance is comparable to that of the F-NPID controller.

7.3 Responses to noise rejection

Next, a simulation was carried out to confirm the robustness of the system against the noise. Figure 7.3 shows the responses and control inputs under the sensor noise in the range −0.2~0.2 [°C] when the outlet temperature of the glycol is measured.

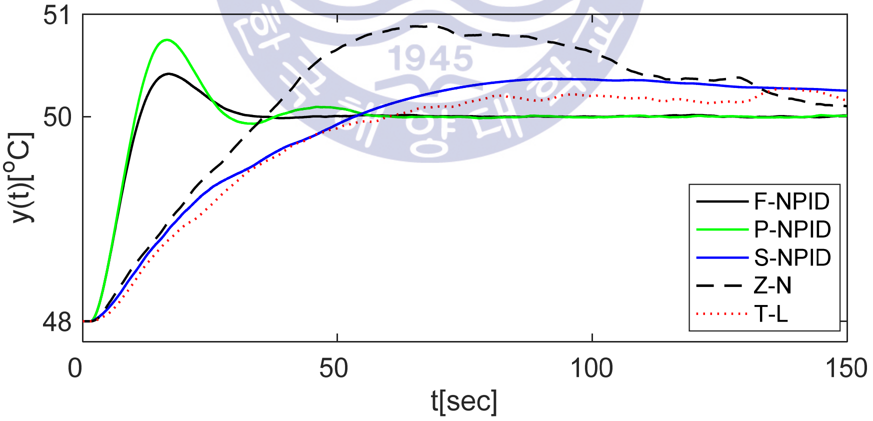

Figure 7.3 Responses of the five control methods when the set-point is step-wisely changed from 48 [°C] to 50 [°C] under Gaussian sensor noise N(0,0.01^2)

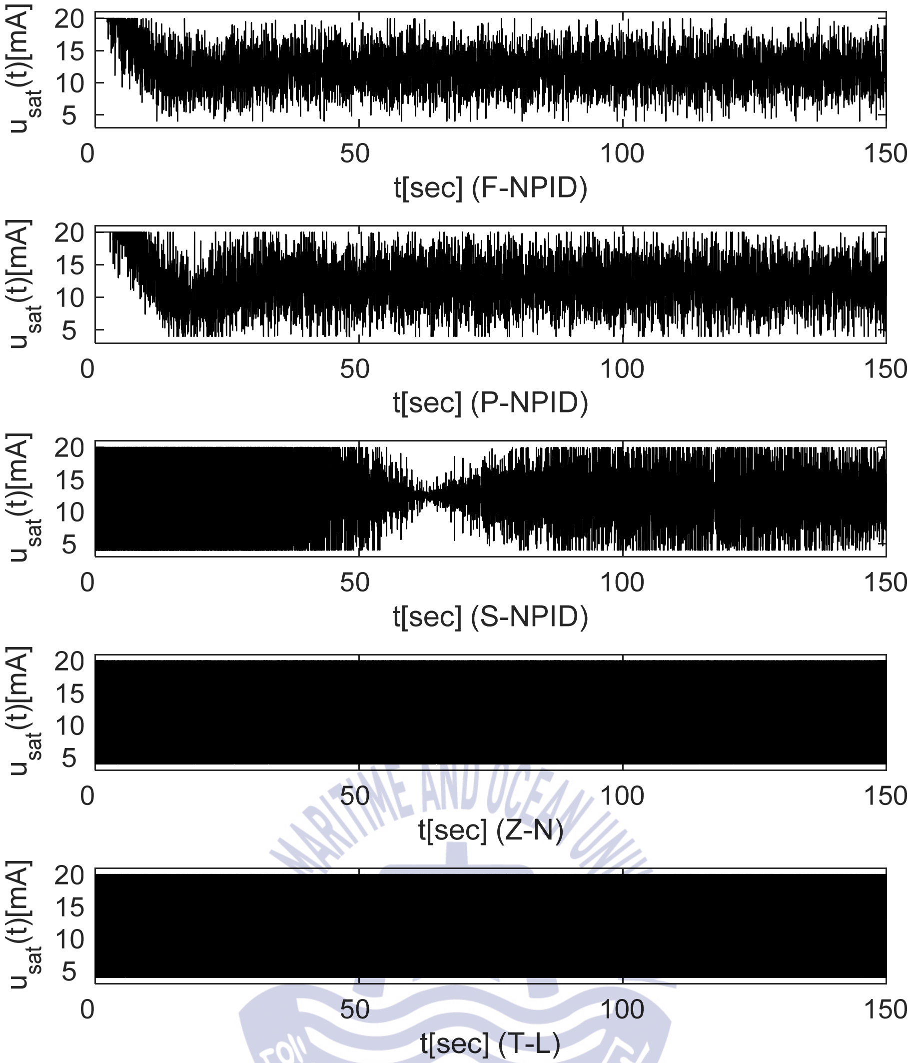

Figure 7.4 Control inputs of the five control methods when the set-point is step-wisely changed from 48 [℃] to 50 [℃] under Gaussian sensor noise N(0,0.01^2)

As shown in the figure, the proposed methods have almost no response changes. However, it can be seen that the existing PID controllers having the ideal derivative action are directly affected by noise, so the responses are all severely distorted.

7.4 Responses to system parameter changes

Next, a simulation is conducted to check the robustness of the proposed NPID controllers for the parameter change of the controlled system. Considering that time constant (T_h) and steady-state gain (K_h) of the heat exchanger in controlled system fluctuate the most severely, the simulation is performed in case these values are changed by about ±10 [%] from the nominal value while changing the set-point. Figure 7.5 shows the responses and control input when the gain and time constant of the heat exchanger are increased by 10 [%], and Figure 7.6 shows the responses and control input when their values are lowered by 10 [%]. Table 7.4 summarizes the performance of each controller for parameter changes.

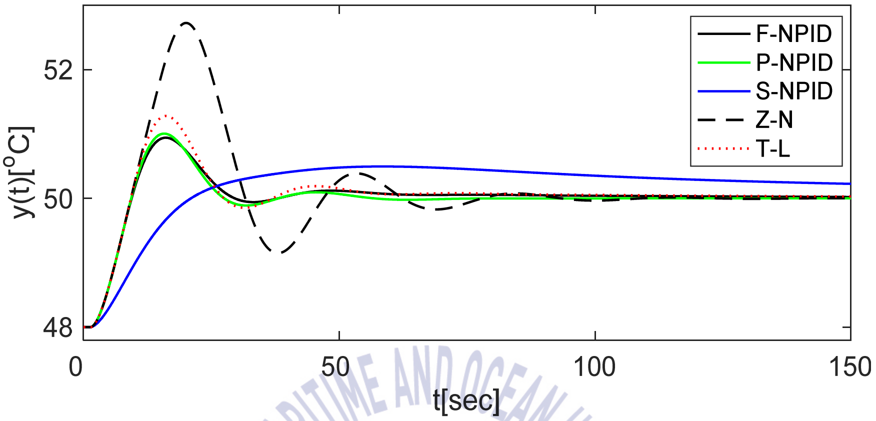

Figure 7.5 Responses comparison to parameter changes (K_h= 12.5→13.75, T_h= 30→33) while y_r= 48 [°C]→50 [°C]

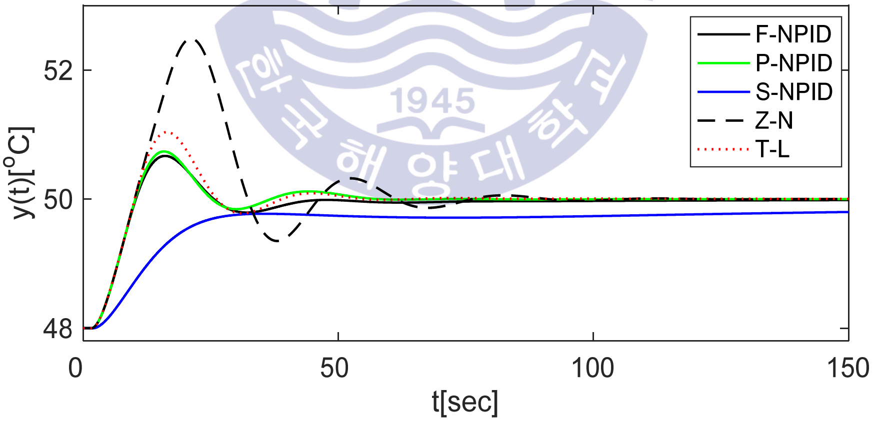

Figure 7.6 Responses comparison to parameter changes (K_h= 12.5→11.25, T_h= 30→27) while y_r= 48 [°C]→50 [°C]

Table 7.4 Performance to parameter changes: K_h= 12.5→13.75, T_h= 30→33

Method	Performance to parameter changes				
	t_r	t_p	M_p	t_s	IAE
F-NPID	5.602	16.100	45.528	61.114	26.237
P-NPID	5.501	15.780	50.280	52.582	24.852
S-NPID	16.71	58.400	12.109	127.63	43.570
Z-N	5.487	20.060	135.95	88.146	62.947
T-L	5.544	16.140	61.685	81.234	30.927

As shown in the figures and tables, the proposed methods were more robust to the parameter changes than the other methods.

7.5 Responses to disturbance changes

After the warm-up process, the engineer no longer changes the set-point and sets the controller to automatic mode. And then, the role of the controller is to control the output to return to the set-point as soon as possible whenever there are disturbance changes.

Given that the two-cycle engine occurs a fuel injection per revolution and that the engine rpm during normal operation is about 120 [rpm], it can be considered that the temperature of the returned glycol changes slightly due to the flow of intermittent LNG fuel every about 0.5 [sec]. Next, a simulation is carried out that changes d, the temperature of the glycol returning to the heat exchanger, from 40 [°C] to 42 [°C] for t= 10~10.5 [sec] while the system is operating at 50 [°C]. Figure 7.7 shows the responses at this time.

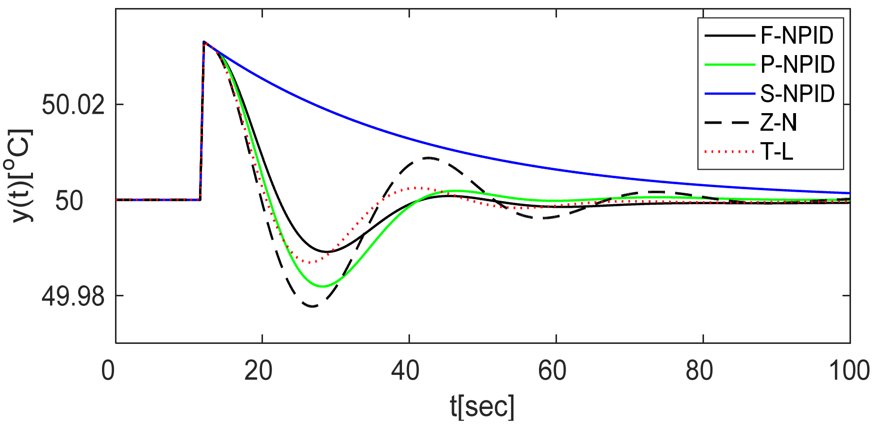

(a) Step responses

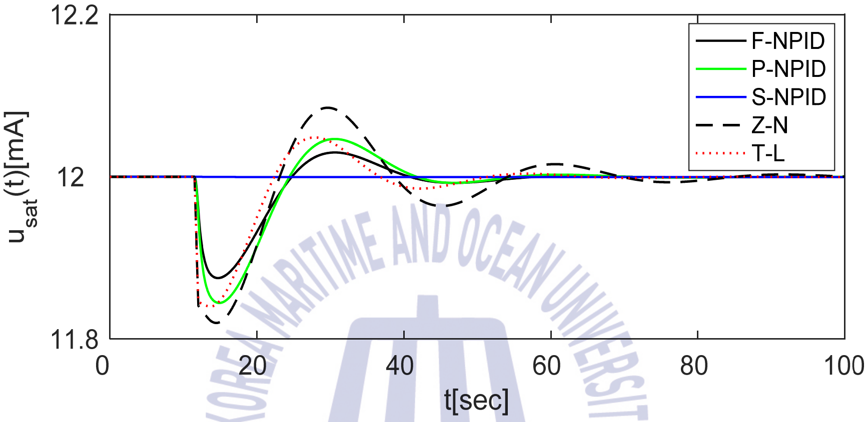

(b) Control inputs

Figure 7.7 Responses and control inputs to disturbance changes (*d*= 40 [°C]→42 [°C])

In the figure, all the methods are satisfactory because the peak temperature is not high, but it can be seen that the proposed two methods were generally recovered faster, indicating that the overall performance is good.

Chapter 8. Conclusion

This thesis proposed two types of nonlinear PID controller, that is, F-NPID controller and P-NPID controller, which control the outlet temperature of the glycol by regulating the steam flow rate supplied to the secondary loop of heat exchanger in the LNG regasification system.

The F-NPID controller had a structure the error between the set-point and output was scaled nonlinearly with a nonlinear gain, and then inputted into the proportional, integral, and derivative controllers. The P-NPID controller had a structure to use the linear PD controller as it is, and input the error which was scaled by the nonlinear gain only into the integral controller. And the filter time constant was installed to mitigate the derivative kick at both derivative blocks of the proposed controllers.

In this case, the nonlinear gain was implemented as the fuzzy model of a Takagi-Sugeno (T-S) type and the error was continuously scaled so that excellent control performance was maintained even in the environment changes.

The stability problem of the feedback system caused by the introduction of the nonlinear function was confirmed based on the circle criterion.

The parameters of the proposed and S-NPID controllers were tuned optimally in terms of minimizing the objective function given by the genetic algorithm. And the parameters of two conventional PID were tuned by inducing periodic oscillation.

The following conclusions were obtained from the simulations performed by applying the proposed controllers to the LNG regasification system.

1. In the result of responses to set-point changes, Overshoot of the S-NPID controller was smaller than others, but Rise time and peak time were the biggest one. So, it took much time to reach the set-point. Z-N method had the biggest overshoot and settling time. The performance of T-L method was good but not better than the proposed two nonlinear PID controllers. Overall, F-NPID and P-NPID controllers were better performance than others. In the result of responses to noise rejection, the proposed

controllers had almost no response changes due to installing the filter time constant in derivative block. But other controllers had the ideal derivative action, it was severely distorted. In the result of responses to system parameters changes, all controllers of performance were a little worse than the responses to set-point changes. Especially, S-NPID controller didn't reach the set-point due to have a long settling time. In the result of responses to disturbance changes, all the methods were satisfactory because the peak temperature was not high, but it can be seen that the two proposed methods generally recovered faster than others.

2. In case of the F-NPID control system, it was concluded that the system was absolutely stable because the Nyquist plot of $G(j\omega)$ did not penetrate the disk D(k_1, k_2) having as diameter the segment $[-1/k_1, -1/k_2]$ located on the x-axis. In case of the P-NPID control system, it was concluded that the system was absolutely stable because the Nyquist plot of $G(j\omega)$ was located on the right of a vertical line defined by $\mathrm{Re}(s) = -1/k_2$.

The comparison results showed that the two proposed nonlinear PID controllers were superior to those by other controllers. It was also found that the performance of P-NPID controller which was made by the F-NPID controller more concise was not significantly different from the performance of the F-NPID controller with a total of five user-defined gains.

Based on the above results, the proposed controllers are considered to be effective for controlling other nonlinear systems with a time delay. And a number of vessels equipped with LNG-fuelled marine engine are not many because it was developed recently. So, the point not to carry out the simulation with field data will be a future research task.

References

[1] Kumar, S., Kwon, H.T., Choi, K.H., Lim, W., Cho, J.H., Tak, K., & Moon, l., 2011. LNG: An eco-friendly cryogenic fuel for sustainable development. *Applied Energy*, 88(12), pp. 4264-4273.

[2] International Maritime Organization (IMO), 2005. *MARPOL 73/78 Annex VI, Regulations for the Prevention of Air Pollution from Ships*. IMO.

[3] International Maritime Organization (IMO), 2008. *Green House Gas Emissions from Ships, Phase 1 Report*. IMO.

[4] International Maritime Organization (IMO), 2005. *MARPOL 73/78 Annex VI, Regulations for the Prevention of Air Pollution from Ships, Regulation 13.6 and 14.3, Emission Control Area.* IMO.

[5] International Maritime Organization (IMO), 2005. *MARPOL 73/78 Annex VI, Regulations for the Prevention of Air Pollution from Ships, Regulation 20, Attained Energy Efficiency Design Index.* IMO.

[6] International Maritime Organization (IMO), 2005. *MARPOL Annex VI, Regulations for the Prevention of Air Pollution from Ships, Regulation 14, Sulphur Oxides and Particulate Matter*. IMO.

[7] International Maritime Organization (IMO), 2005. *MARPOL Annex VI, Regulations for the Prevention of Air Pollution from Ships, Regulation 13, Nitrogen Oxides.* IMO.

[8] Kim, J.H., 2013. Introduction of LNG propulsion line with market changes direction and shipping services. *Journal of Korea Maritime Institute*, 3(2), pp. 103-119.

[9] Korea Energy Economics Institute, 2016. *World Energy Issue Insight Special*, Ulsan: Korea Energy Economics Institute.

[10] MAN Diesel & Turbo, 2012. *ME-GI Duel Fuel MAN B&W Engines: A Technical, Operational and Cost-effective Solution for Ships Fuelled by Gas*, MAN Diesel & Turbo.

[11] Jafarzadeh, S., Paltrinieri, N., Utne, I.B., & Ellingsen, H., 2017. LNG-fuelled fishing vessels: A systems engineering approach. *Transportation Research Part D:*

Transport and Environment, 50, pp. 202-222.

[12] Åström, K.J., & Hägglund, T., 2005. *Advanced PID control*. ISA: North Carolina.

[13] Vinaya, V.K., Ramkumar, K., & Alagesan, V., 2012. Control of heat exchangers using model predictive controller. *Proceeding of the 2012 IEEE International Conference on Advances in Engineering, Science and Management*, Tamil Nadu June 30-31, 2012, pp. 242-246.

[14] Oravec, J., Bakošová, M., Mészáros, A., & Míková, N., 2016. Experimental investigation of alternative robust model predictive control of a heat exchanger. *Applied Thermal Engineering*, 105, pp. 774-782.

[15] Vasičkaninová, A., & Bakošová, M., 2015. Control of heat exchanger using neural network predictive controller combined with auxiliary fuzzy controller. *Applied Thermal Engineering*, 89, pp. 1046-1053.

[16] Pandey, M., Ramkumar, K., & Alagesan, V., 2012. Design of fuzzy logic controller for a cross flow shell and tube heat-exchanger. *Proceeding of the 2012 IEEE International Conference on Advances In Engineering, Science And Management*, Tamil Nadu, June 30-31, 2012, pp. 150-154.

[17] Kumar, A., & Garg, K.K., 2015. Comparison of Ziegler-Nichols, Cohen-Coon and fuzzy logic controllers for heat exchanger model. *International Journal of Science, Engineering and Technology Research*, 4(6), pp. 1917-1920.

[18] Ahmad, M.A., Ishak, A.A., & Ismail, N.K., 2012. New hybrid model reference adaptive supervisory fuzzy logic controller for shell-and-tube heat exchanger temperature system. *2012 IEEE Control and System Graduate Research Colloquium*, Shah Alam, July 16-17, 2012, pp. 49-54.

[19] Duka, A.V., & Oltean, S.E., 2012. Fuzzy control of a heat exchanger. *2012 IEEE International Conference on Automation Quality and Testing Robotics*, Cluj-Napoca, May 24-27, 2012, pp. 135-139.

[20] Emhemed, A.A.A., Alsseid, A., & Hanafi, D., 2017. Modelling and controller design for temperature control of power plant heat exchanger. *Universal Journal of Control and Automation*, 5(3), pp. 49-53.

[21] Sivakumar, P., Prabhakaran, D., & Kannadasan, T., 2012. Temperature control of shell and tube heat exchanger by using intelligent controllers-case study. *International Journal of Computational Engineering Research*, 2(8), pp. 285-291.

[22] Beirami, H., & Zerafat, M.M., 2015. Self-tuning of an interval type-2 fuzzy PID controller for a heat exchanger system. *Iranian Journal of Science and Technology Transactions of Mechanical Engineering*, 39(M1), pp. 113-129.

[23] Ahn, J.K., So, G.B., Lee, J.Y., Lee, Y.H., So, M.O., & Jin, G.G., 2014. PID control of a shell and tube heat exchanger system incorporating feedforward control and anti-windup techniques. *Journal of Institute of Control Robotics and Systems*, 20(5), pp. 543-550.

[24] Habobi, N.A., 2010. PC based controller for shell and tube heat exchanger. *Iraqi Journal of Chemical and Petroleum Engineering*, 11(1), pp. 47-53.

[25] Sarabeevi, G.M., & Beebi, M.L., 2016. Temperature control of shell and tube heat exchanger system using internal model controllers. *2016 International Conference on Next Generation Intelligent Systems*, Kottayam, September 1-3.

[26] Padhee, S., Khare, Y.B., & Singh, Y., 2011. Internal model based PID control of shell and tube heat exchanger system. *Proceeding of 2011 IEEE Students' Technology Symposium*, Kharagpur, January 14-16, 2011, pp. 297-302.

[27] Padhee, S., 2011. *Performance evaluation of different conventional and intelligent controllers for temperature control of shell and tube heat exchanger system*. Master. Punjab: Thapar University.

[28] Padhee, S., 2014. Controller design for temperature control of heat exchanger system: simulation studies. *World Scientific and Engineering Academy and Society (WSEAS) Transactions on Systems and Control*, 9, pp. 485-491.

[29] Khare, Y.B., & Singh, Y., 2010. PID control of heat exchanger system. *International Journal of Computer Application*, 8(6), pp. 22-27.

[30] Khanvilkar, S., Jadhav, S.P., Vyawahare, V., & Kadam, V., 2016. Comparative study of fuzzy and IMC based controllers for heat exchanger system. *2016 International Conference on Automatic Control and Dynamic Optimization Techniques*, Pune, September 9-10, pp. 344-348.

[31] Xiao, Y., Cui, G., Chen, J., & Zhao, B., 2017. Improved model control strategy with dynamic adaption for heat exchangers in energy system. *An International Journal of Computation and Methodology Numerical Heat Transfer, Part A: Applications*, 72(6), pp.458-478.

[32] Skorospeshkin, M.V., Sukhodov, M.S., Skorospeshkin, V.N., & Rymashevskiy, P.O.,

2017. An adaptive control system for a shell-and-tube heat exchanger. *Journal of Physics: Conference Series*, 803(1).

[33] Manikandan, R., & Vinodha, R., 2016. Multiple model based adaptive control for shell and tube heat exchanger process. *International Journal of Applied Engineering Research*, 11(5), pp. 3175-3180.

[34] Banu, U.S., & Uma, G., 2007. Fuzzy gain scheduled pole placement based on state feedback control of CSTR. *IET_UK International Conference on Information and Communication Technology in Electrical Sciences* (*ICTES 2007*), India, December 20-22, 2007, pp. 63-68.

[35] Geetha, M., Balajee, K.A., & Jovitha, J., 2012. Optimal tuning of virtual feedback PID controller for a continuous stirred tank reactor (CSTR) using particle swarm optimization (PSO) algorithm. *IEEE International Conference on Advances in Engineering, Science and Management* (*ICAESM-2012*), Tamil Nadu, March 30-31, 2012, pp. 94-99.

[36] Aslam, F., & Kaur, G., 2011. Comparative analysis of conventional, P, PI, PID and fuzzy logic controllers for the efficient control of concentration in CSTR. *International Journal of Computer Applications*, 17(8), pp. 12-16.

[37] Banu, U.S., & Uma, G., 2008. Fuzzy gain scheduled CSTR with GA-based PID. *Chemical Engineering Communications*, 195(10), pp. 1213-1226.

[38] Nekoui, M.A., Khameneh, M.A., & Kazemi, M.H., 2010. Optimal design of PID controller for a CSTR system using particle swarm optimization (PSO). *Proceedings of 14th International Power Electronics and Motion Control Conference* (*EPE-PEMC-2010*), Ohrid, September 6-8, 2010, pp. T7-63-66.

[39] Chen, C.T., & Peng, S.T., 1999. Learning control of process systems with hard input constraints. *Journal of Process Control*, 9(2), pp. 151-160.

[40] Saoud, L.S., Rahmoune, F., Tourtchine, V., & Baddari, K., 2011. An inexpensive embedded electronic continuous stirred tank reactor(CSTR) based on neural networks. *2011 International Conference on Multimedia Technology* (*ICMT*), Hangzhou, July 26-28, 2011, pp. 6233-6237.

[41] Korkmaz, M., Aydoğdu, Ö., & Doğan, H., 2012. Design and performance comparison of variable parameter nonlinear PID controller and genetic algorithm based PID controller. *Proceeding of 2012 IEEE International Symposium on*

Innovations in Intelligent Systems and Applications, Trabzon, July 2-4, 2012, pp. 1-5.

[42] Isayed, B.M., & Hawwa, M.A., 2007. A nonlinear PID control scheme for hard disk drive servosystems. *2007 Mediterranean Conference on Control & Automation*, Athens, June 27-29, 2007, pp. T16-014.

[43] Zhang, H., & Hu, B., 2012. The application of nonlinear PID controller in generator excitation system. *Energy Procedia*, 17, pp. 202-207.

[44] Chen, J.P., Lu, B.C., Fan, F., Zhu, S.C., & Wu, J.X., 2011. A nonlinear PID controller for electro-hydraulic servo system based on PSO algorithm. *Applied Mechanics and Materials*, 141, pp. 157-161.

[45] Seraji, H., 1997. A new class of nonlinear PID controllers. *International Federation of Automatic Control* (*IFAC*) *Proceedings Volumes*, 30(20), pp. 65-71.

[46] Zaidner, G., Korotkin, S., Shteimberg, E., Ellenbogen, A., Arad, M., & Cohen, Y., 2010. Nonlinear PID and its application in process control. *2010 IEEE 26th Convention of Electrical and Electronics Engineers in Israel*, Eliat, November 17-20, 2010, pp. 574-577.

[47] Jiang, F., & Gao, Z., 2001. An application of nonlinear PID control to a class of truck ABS problems. *Proceeding of the 40th IEEE Conference on Decision and Control*, Orlando, December 4-7, 2001, pp. 516-521.

[48] Man Diesel & Turbo, 2009. *ME-GI Dual FUEL MAN B&W Engines: A Technical, Operational and Cost-effective Solution for Ships Fuelled by Gas*, Man Diesel &Turbo.

[49] Daewoo Shipbuilding & Maritime Engineering (DSME), 2013. *LNG Fuel Gas Supply System (FGSS®)*, Seoul: Bulletin of the society of naval architects Korea.

[50] https://www.kamui.co.jp/english/products/shell_and_tube

[51] Daewoo Shipbuilding & Maritime Engineering (DSME), 2010. *Green Ship and Development of Maritime Transportation*, DSME.

[52] Daewoo Shipbuilding & Maritime Engineering (DSME), 2011. *Development of LNG Fuelled Propulsion System for Containerships and Tankers*, DSME.

[53] Afrianto, H., Tanshen, M.R., Munkhbayar, B., Suryo, U.T., Chung, H., & Jeong, H., 2014. A numerical investigation on LNG flow and heat transfer characteristic in heat exchanger. *International Journal of Heat and Mass Transfer*, 68, pp. 110-118.

[54] Nozaka, Y., 1993. Trend of new control theory application in industrial process control (survey). *International Federation of Automatic Control (IFAC) Proceedings Volumes*, 26(2), pp. 215-218.

[55] O'Dwyer, A., 2009. *Handbook of PI and PID Controller Tuning Rules*. 3rd Ed. Imperial College Press: London

[56] Ziegler, J.G., & Nichols, N.B., 1942. Optimal settings for automatic controllers. *Transactions of the American Society Mechanical Engineers (ASME)*, 64, pp. 759-768.

[57] Pham, D.T. & Jin, G.G., 1996. A hybrid genetic algorithm. *Proceeding 3rd World Conference on Expert Systems*, Seoul, pp. 748-757.

[58] Matyas, J., 1965. Random optimization. *Automation and Remote Control*, 26, pp. 246-253.

[59] Grefenstette, J.J., 1986. Optimization of control parameters for genetic algorithms. *IEEE Transactions on System, Man, and Cybernetics*, 16(1), pp. 122-128.

[60] Jin, G.G., & Joo, S., 2000. A study on a real-coded genetic algorithm. *Journal of Control, Automation and Systems Engineering*, 6(4), pp.268-275.

[61] Michalewicz, Z., 1996. *Genetic Algorithms+Data Structures=Evolution Programs*. 3rd Ed. Springer-Verlag: Berlin.

[62] Goldberg, D.E., 1989. *Genetic Algorithms in Search, Optimization and Machine Learning*, Addison-Wesley: Boston.

[63] De Jong, K.A., 1975. *An Analysis of the Behavior of a Class of Genetic Adaptive Systems*. Doctoral dissertation, The University of Michigan.

[64] Jin, G.G., 2002. *Genetic Algorithms and its applications*. Kyo Woo Sa: Seoul.

[65] Whitley, D., 1994. A genetic algorithm tutorial. *Statistics and Computing*, 4, pp. 65-85.

[66] Gen, M., & Cheng, R., 1997. *Genetic Algorithms and Engineering Design*. A Wiley-Interscience Publication: New York.

[67] Holland, J.H., 1992. *Adaptation in Natural and Artificial Systems*. MIT Press Cambridge: University of Michigan

[68] Khalil, H.K., 2002. *Nonlinear Systems*. 3rd Ed. Prentice Hall: New Jersey.

[69] Silva, G.J., Datta, A., & Bhattacharyya, S.P., 2001. Controller design via Padé approximation can lead to instability. *Proceeding of the 40th IEEE Conference on*

Decision and Control, Orlando, December 4-7, 2001, pp. 4733-4737.

[70] Tagaki, T., & Sugeno, M., 1985. Fuzzy identification of system and its application to modeling and control. *IEEE Transactions on Systems, Man, and Cybernetics* (*SMC*), 15(1), pp. 116-132.

[71] So, G.B., & Jin, G.G., 2018. Temperature control of a regasification system for LNG-fuelled marine engines. *Proceeding of the 8th International Conference on Advances in Mechanical, Aeronautical and Production Techniques* (*MAPT 2018*), Kuala Lumpur, February 03-04, 2018, pp. 14-19.

[72] So, G.B., & Jin, G.G., 2018. Fuzzy-based nonlinear PID controller and its application to CSTR. *Korean Journal of Chemical Engineering*, 35(4), pp. 819-825.